INSTITUTE FOR FUSION STUDIES

DOE/ET-53088-552 IFSR #552

Resistive Magnetohydrodynamic Studies of Tearing Mode Instability with Equilibrium Shear Flow and Magnetic Reconnection

LEON OFMAN
Institute for Fusion Studies
The University of Texas at Austin
Austin, Texas 78712

June 1992

THE UNIVERSITY OF TEXAS

AUSTIN

RESISTIVE MAGNETOHYDRODYNAMIC STUDIES OF TEARING MODE INSTABILITY WITH EQUILIBRIUM SHEAR FLOW AND MAGNETIC RECONNECTION

APPROVED BY

DISSERTATION COMMITTEE:

Philip J. Morrison

Wendell Horton

R D Hazeltine

R. S. Steinolfson

Paul J Morrison

Copyright
by
Leon Ofman
1992

Dedicated to my parents and my wife

RESISTIVE MAGNETOHYDRODYNAMIC STUDIES OF TEARING MODE INSTABILITY WITH EQUILIBRIUM SHEAR FLOW AND MAGNETIC RECONNECTION

by

LEON OFMAN, M.S.

DISSERTATION

Presented to the Faculty of the Graduate School of

The University of Texas at Austin

in Partial Fulfillment

of the Requirements

for the Degree of

DOCTOR OF PHILOSOPHY

THE UNIVERSITY OF TEXAS AT AUSTIN

May, 1992

Acknowledgments

I am very grateful to Professor Philip J. Morrison and Dr. Richard S. Steinolfson for their guidance, assistance, and collaboration. I have greatly benefited from their expertise and experience, and I deeply appreciate their time and effort that made this dissertation possible.

I would like to thank Professors R. D. Hazeltine and C. W. Horton for the useful discussions and advice that they offered throughout my studies in Austin. I would also like to thank Professor P.R. Shapiro for serving as my committee member.

I have benefited from the many useful discussions that I had with the students at the Institute for Fusion Studies. I would especially like to mention R. Acevedo, S. Cable, D. Curran, D. del Castillo, J. Hernandez, J. Koga, C. Kueny, M.G. Prahovic, R. Kinney, B. Schadwick, X.N. Su, H. Xiao, and the now former students Dr. X.L. Chen, and Dr. A. McAlister.

I want to acknowledge financial support from the Institute for Fusion Studies and from the U.S. Department of Energy Contract No. DE- FG05-80ET-53088 and National Science Foundation Contract Nos. ATM-89-96317 and ATM-90-15705. I have also benefited from my work at Southwest Research Institute.

I would like to thank the staff members at the Institute of Fusion Studies, especially the secretaries, D. Allen, S. Crumley, J. Gillette, J. Patton, S. Stewart, and C. Valentine. I would also like to thank the staff at Southwest

Research Institute, and especially W. Lewis who made my work there even more pleasant.

I would also like to thank A.Y. Aydemir, J. Dibble, A. Macmahon, and W.H. Miner for computer advice and the National Energy Research Supercomputer Center for the use of their Cray supercomputers.

Special thanks to my wife Rachel Ofman for her love and understanding that made my work possible. Finally, I wish to thank my parents for their love and support throughout the difficult times.

Leon Ofman

The University of Texas at Austin

May, 1992

RESISTIVE MAGNETOHYDRODYNAMIC STUDIES OF TEARING MODE INSTABILITY WITH EQUILIBRIUM SHEAR FLOW AND MAGNETIC RECONNECTION

Publication No. _____

Leon Ofman, Ph.D.
The University of Texas at Austin, 1992

Supervisor: Philip J. Morrison

Magnetic reconnection and tearing can play an important role in fusion experiments and in space plasmas. This thesis is devoted to the magnetohydrodynamic (MHD) study of the linear and nonlinear evolution of the resistive tearing mode instability in the presence of equilibrium shear flow, and the reconnection of an x-point magnetic field configuration.

Numerical solutions of the linearized time-dependent MHD equations and growth rate scaling are obtained. The results of the computations are compared to previous work, and the computed growth rate scalings agree with analytical predictions. The introduction of viscosity and small equilibrium shear flow alters the growth rate scaling considerably. When the shear flow is

large, the growth rate behaves in a more complex way, and Kelvin-Helmholtz instability effects are present.

The linear evolution of the double tearing mode with equilibrium shear flow and viscosity is investigated numerically. The dispersion relation for the growth rate of the double tearing instability is generalized to include flow. Relatively small shear flow at the resonant surfaces has a stabilizing effect on the double tearing mode. For Reynolds number comparable or larger than the magnetic Reynolds number a stabilizing effect is found.

The nonlinear evolution of the tearing mode instability with equilibrium shear flow is investigated via numerical solutions of the resistive incompressible 2-D MHD equations. The simulations are initiated with solutions of the linearized MHD equations. Magnetic energy release decreases, and the saturation time increases with shear flow. The validity of the numerical solutions is tested by verifying that the total energy and helicity are conserved.

The reconnection of two-dimensional stressed x-type neutral point magnetic fields is studied via solution of the nonlinear incompressible and compressible resistive MHD equations. Solutions of the linear eigenvalue problem are obtained and compared to the MHD simulations. It is found that with conducting boundary condition, the fields relax to the force-free x-type neutral point at a rate close to that predicted by linear theory. When flow through the boundaries is present, the x-point evolves into a current sheet.

Table of Contents

Acknowledgments v

Table of Contents ix

List of Tables xi

List of Figures xii

1. Introduction 1

1.1 Overview and Motivation 1

1.2 Model Equations 3

1.3 Organization of this dissertation 5

2. Linear Evolution of the Tearing Mode with Equilibrium Shear Flow and Viscosity 8

2.1 Introduction 8

2.2 Basic Equations 10

2.3 Linear Theory 12

2.4 Method of Solution 15

2.5 Numerical Results 18

2.6 Summary and Discussion 23

3. Linear Studies of the Double Tearing Mode with Equilibrium Shear Flow and Viscosity 35

3.1 Introduction 35

3.2 Model Equations 36
3.3 Dispersion Relation 38
3.4 Numerical Results 42
3.5 Summary and Discussion 47

4. Nonlinear Evolution of the Tearing Mode with Equilibrium Shear Flow **54**

4.1 Introduction 54
4.2 MHD Equations 55
4.3 Method of Solution 57
4.4 Numerical Results 60
4.5 Summary and Discussion 68

5. Resistive Reconnection of an X-type Neutral Point **85**

5.1 Introduction 85
5.2 Incompressible 2-D MHD Equations 87
5.3 Linear Dispersion Relation 89
5.4 Nonlinear Simulations 95
5.4.1 Incompressible MHD 95
5.4.2 Compressible MHD 98
5.5 Summary and Discussion 100
5.6 Appendix 112

BIBLIOGRAPHY **115**

Vita

List of Tables

2.1 Summary of the effects of equilibrium shear flow on the tearing mode. (From Chen and Morrison, 1990a.) 16

2.2 The maximal absolute values of the solutions in Figs. 2.3-2.5. . . 20

3.1 The values of the flow parameter V, the shear at the resonant surfaces R_s, and the growth rates for $y_s = 0.15$, $S = 10^4$, and $y_s = 0.75$, $S = 10^6$ with $R = 0.5$. 46

4.1 The change in the magnetic, kinetic, and total energies. 65

List of Figures

2.1 The initial equilibrium magnetic field and flow. 13

2.2 The oscillating and exponentially growing components of the solutions. 25

2.3 The spatial variations of the complex solutions W and ψ (inviscid case) normalized to their peak values. The equilibrium flow is $G = V\tanh(Ry)$. 26

2.4 Plot of W nd ψ as in Fig. 2.3 except the equilibrium flow is $G = V\mathrm{sech}\,(Ry)$. 27

2.5 Same as Fig. 2.4a with (a) $R = 2.5$. (b) Same as Fig. 2.4b with $R = 2.5$. 28

2.6 Growth rate scaling with S. 29

2.7 The growth rate as a function of the shear parameter R. 30

2.8 Calculated numerical growth rate scaling with viscosity parameter S_v. The other parameters are $S = 10^6$, $V = 0$, $\alpha = 0.5$. . . . 31

2.9 The dependence of the growth rate on Q. 32

2.10 The dependence of the growth rate on S_v for sech flow profile and small shear. 33

2.11 The value of γ_I and its magnitude calculated with FFT for sech flow profile. 34

3.1 The initial equilibrium normalized magnetic field $F(y)$ and shear flow $G(y)$ given by Eqs. (3.1) and (3.2), respectively. 39

3.2 The spatial dependence of the complex perturbed magnetic field ψ and flow W. 49

3.3 Growth rate dependence on R_s 50

3.4 Growth rate dependence on S. 51

3.5 The dependence of the complex growth rate γ on the shear parameter R_s. 52

3.6 Growth rate scaling with viscosity parameter S_v. 53

4.1 Spatial dependence of the flux functions with $S = 10^2$, $V = 0.1$ (top figure), $V = 0.2$ (bottom figure) and tanh equilibrium flow profile. 70

4.2 Spatial dependence of the stream functions with $S = 10^2$, $V = 0.1$ (top figure), $V = 0.2$ (bottom figure) and tanh equilibrium flow profile. 71

4.3 Spatial dependence of the flux functions with $S = 10^2$, $V = 0.1$ (top figure), $V = 0.5$ (bottom figure), and sech equilibrium flow profile. 72

4.4 Spatial dependence of the stream functions with $S = 10^2$, $V = 0.1$ (top figure), $V = 0.5$ (bottom figure), and sech equilibrium flow profile. 73

4.5 Contour plot of Ψ and Φ with $V = 0.5$, $S = 10^2$, and the tanh flow profile. 74

4.6 Contour plot of Ψ and Φ with $V = 0.1$, $S = 10^4$, and the sech flow profile. 75

4.7 Contour plot of ψ and ϕ with $V = 0.1$, $S = 10^4$, and the sech flow profile. 76

4.8 Contour plot of $J = -\nabla^2\psi$ with $V = 0.0$ (top figure), and $V = 0.3$ (bottom figure) and the tanh flow profile for $S = 10^2$. . 77

4.9 The mode structure of ψ and ϕ with $V = 0.3$ and the tanh equilibrium flow profile for $S = 10^2$. 78

4.10 The temporal evolution for the case where $S = 10^2$, $V = 0.1$ with the tanh equilibrium flow profile. 79

4.11 The temporal evolution of ΔE_{Mx} (curve A), ΔE_{My} (curve B), and ΔE_{tot} (curve C), with $V = 0.2$ (top figure), and $V = 0.3$ (bottom figure). 80

4.12 The nonlinear evolution of the $S = 10^4$, $V = 0.5$ tearing mode with the tanh equilibrium flow profile. 81

4.13 The nonlinear evolution for the case where $S = 10^5$, $V = 0.5$ with the tanh equilibrium flow profile. 82

4.14 Numerical test of the energy conservation relation with $S = 10^2$. The energy dissipation as calculated from the l.h.s. of Eq. (4.10) (curve A), and the r.h.s. of Eq. (4.10) (curve B). 83

4.15 Numerical test of the helicity conservation relations with $S = 10^2$. The magnetic helicity dissipation as calculated from l.h.s. of Eq. (4.11) (curve A), and the r.h.s. of Eq. (4.11) (curve B). . 84

5.1 The initial equilibrium magnetic field configuration with an x-point. 90

5.2 Decay rates of the modes with $m = n = 0$, and $n = 1$, $m = 2, 4$ obtained from the solution of the linear dispersion relation. . . . 94

5.3 The real and imaginary parts of the eigenfunctions $f(r)$ with $m = 0$, $n = 1$, $S = 10^3$, $\gamma = 0.292 + 1.248i$ (top figure), and $m = 1$, $n = 3$, $S = 10^5$, $\gamma = 0.275 + 2.343i$ (bottom figure). . . . 96

5.4 The decay rate scaling with S of the $m = n = 0$ mode. 102

5.5 The perturbed energies of an x-point. ΔE_{Mx} (curve A), ΔE_{My} (curve B), and ΔE_{tot} (curve C). 103

5.6 The value of $\psi(0, 0, t)$ (curve A), and the reconnected flux (curve B). 104

5.7 Contour lines of Ψ. 105

5.8 The sheet current at $t = 5.3\tau_h$ with the incompressible MHD simulations. 106

5.9 Compressible MHD simulation of the relaxation of an x-point with $m = 0$ initial perturbation. 107

5.10 Compressible MHD simulation of the relaxation of an x-point with $m = 2$ initial perturbation. 109

5.11 The evolution of a sheet current with the compressible MHD simulations. 110

5.12 The velocity stream lines of the sheet current. 113

Chapter 1

Introduction

1.1 Overview and Motivation

Understanding th icroscopic and macroscopic processes that c cur in plasma involves the study of plasma instabilities. In an ideal infinitely conducting plasma, the field lines and the plasma move together, and the topology of the field lines cannot change. Tearing mode instability occurs when a component of the ambient magnetic field (in Cartesian geometry) reverses its sign, and the resistivity becomes important in a singular region of the plasma (tearing layer). The magnetic field is then free to tear and reconnect, and the topology of the magnetic field lines can change. Large currents are generated in the singular region and the free magnetic energy is released through Ohmic heating of the plasma. As the instability proceeds, magnetic islands are generated and grow exponentially in size (Furth, Killeen, Rosenbluth, 1963) until they reach a size comparable to the tearing layer. The growth then slows to an algebraic rate due to the nonlinear satura n of the instability (Rutherford, 1973). When shear flow is present, the growth rate can decrease or increase depending on the flow profile and its parameters (Chen and Morrison, 1990; Ofman *et al.*, 1991). When reconnection occurs at a singular line (singular point in 2-D), the initial perturbation can decay away on a resistive time scale (Hassam, 1991; ig and McClymont, 1991), or with appropriate boundary ditions it mig evolve into a sheet curre t (Dungey, 1953).

These processes are of particular interest to the study of laboratory and space plasmas. The tearing mode instability is a major source of the disruption of nested magnetic flux surfaces (on which the plasma pressure is constant) that are needed to confine the plasma in a tokamak. Shear flow (or poloidal sheared rotation in toroidal geometry) of the plasma might be one of the means to control the tearing instability and to suppress it. In space plasma the tearing mode instability and magnetic reconnection are associated with solar flares (Priest, 1981) and solar coronal loops (Priest, 1985). Strong shear flow motions are observed in the solar chromosphere, and in the corona and are believed to exist in galactic jets. The reconnection of an x-point magnetic field was suggested as a mechanism for release of magnetic energy in solar flares and for the formation of sheet current (Dungey, 1953; Syrovatsky, 1966).

The resistive magnetohydrodynamic (MHD) approach used in this dissertation relies on the assumption that plasma can be approximated by a set of fluid equations together with Maxwell's equations with finite dissipation parameters. Many approximations are used in the derivation of the MHD equations (see below), and their applicability is restricted to temporal and spatial scales in which the "MHD ordering" holds. In spite of these shortcomings, MHD theory has proven to be a very useful tool for understanding the various macroscopic processes in plasma. The full set of the MHD equations is nonlinear and for most cases of interest cannot be solved analytically, and is difficult to solve numerically for realistic plasma configuration in three dimensions. Usually, simplifying assumptions are made with respect to the geometry, and to the boundary and the initial conditions. The MHD equations are then linearized, and the resulting equations are solved numerically in one spatial

dimension. Additional approximations are made in order to solve the linear set of equations analytically.

Progress in computer technology and algorithm development makes it feasible to solve nonlinear MHD equations in two or three spatial dimensions with realistic initial and boundary condition and with satisfactory spatial and temporal resolution. On one hand, the validity of the simplifying assumptions in the linear and the nonlinear theory can be tested with the aid of computer simulations. On the other hand, computer simulation codes are tested against the analytical theory, and the quality of the simulation can be estimated from its energy conservation and additional constants of motion. Finally, the results of both analytical theory and computer simulation can be compared to experiments or observations, and qualitative predictions of experimental results or physical phenomena can be made, although, due to the large number of assumptions used in the theory, a quantitative prediction is rarely possible.

In this dissertation an MHD approach is used to study numerically and analytically the linear and nonlinear evolution of the tearing mode instability in the presence of shear flow for a wide parameter range, and with various flow profiles. The magnetic reconnection of an x-point and the possibility of current sheet formation are also investigated.

1.2 Model Equations

We assume that collisional MHD theory (Drake and Lee, 1977) is applicable, that the plasma resistivity η is constant and isotropic, and the perpendicular viscosity ν is constant (Braginskii, 1965). We neglect the effects

of gravity. The basic equations in cgs units are:

$$\rho\left[\frac{\partial \mathbf{v}}{\partial t}+(\mathbf{v}\cdot\nabla)\mathbf{v}\right]=-\nabla P+\frac{1}{4\pi}(\nabla\times\mathbf{B})\times\mathbf{B}+\rho\nu\nabla_{\perp}^{2}\mathbf{v} \tag{1.1}$$

$$\frac{\partial \mathbf{B}}{\partial t}=\nabla\times(\mathbf{v}\times\mathbf{B})-\frac{c^{2}\eta}{4\pi}\nabla\times(\nabla\times\mathbf{B}) \tag{1.2}$$

$$\frac{\partial \rho}{\partial t}+\nabla\cdot(\rho\mathbf{v})=0 \tag{1.3}$$

$$\nabla\cdot\mathbf{B}=0 \tag{1.4}$$

$$\frac{d}{dt}\left(\frac{P}{\rho^{\gamma_p}}\right)=0 \tag{1.5}$$

where c is the speed of light, ρ is the plasma density, $\mathbf{B}$ is the magnetic field, $\mathbf{v}$ is the velocity of the plasma, P is the pressure, and γ_p is the polytropic index.

In the second and third Chapter we use the linearized version of the MHD equations in one spatial dimension with constant and uniform density. The initial magnetic field, flow, and the boundary conditions are appropriate for the tearing (Chapter 2) and the double tearing (Chapter 3) modes. In the fourth and fifth Chapter we present and solve the nonlinear incompressible 2-D MHD equations. Assuming $\rho = const.$, Eq. (1.3) becomes

$$\nabla\cdot\mathbf{v}=\mathbf{0}, \tag{1.6}$$

and the pressure P becomes an implicit variable that is eliminated from the calculations by taking a curl of Equation (1.1). In Chapter 5 we solve the adiabatic ($\gamma_p = 5/3$) and compressible 2-D MHD equations for the reconnection of an x-point. For isothermal evolution $\gamma_p = 1$ can be used.

1.3 Organization of this dissertation

In Chapter 2 the linearized, time-dependent, incompressible visco-resistive MHD equations for the tearing mode are solved numerically for a wide range of parameters. The linear theory of the resistive tearing mode instability, has been recently extended by introducing the effect of equilibrium shear flow and viscosity. In this chapter, the growth rate scalings, and the eigenfunctions are obtained, and the results of the computations are compared to previous work. The computed growth rate scaling agree well with the analytical predictions. The presence of flow modifies the solutions considerably and affect the growth rate scaling: it can stabilize or destabilize the mode. The presence of small flow shear (compared to the magnetic shear) alters the growth rate scaling with viscosity. When the shear flow is large, the growth rate becomes independent of small viscosity, and the transition to Kelvin-Helmholtz instability is observed.

In Chapter 3 the linear evolution of the double tearing mode with equilibrium shear flow parallel to the magnetic field and viscosity is investigated numerically. Growth rates obtained from the MHD simulations are found to agree with the solutions of the double tearing dispersion relation in the parameter range of validity. Solutions of the linearized MHD equations for the double tearing mode with parallel shear flow are found for wide relevant parameter ranges. Large (weakly coupled) and small (strongly coupled) rational surface separation are investigated. Shear flow decouples the rational surfaces, reduces the growth rate, and transforms the instability to the standard tearing mode. Overstable modes are found from the solutions of the dispersion relation and in the numerical computation. The presence of small viscosity reduces the

growth rate of the instability, but has little effect on the oscillatory part of the growth rate. The temporal oscillations of the solutions increase with the flow at the resonant surfaces at a rate slower than that of the Doppler shift. The parameters of the shear flow that will stabilized the double tearing mode with large and small rational surface separation is found.

Chapter 4 is devoted to the study of the nonlinear evolution of the tearing mode instability with equilibrium shear flow via numerical solutions of the resistive MHD equations. The two-dimensional nonlinear simulations are in slab geometry, are periodic in the x-direction, and are initiated with solutions of the linearized MHD equations presented in Chapter 2. When the shear flow is small the tearing mode saturates within one resistive time, while for larger flows the nonlinear saturation develops on a longer time scale. The magnetic energy release decreases and the saturation time increases with the flow shear, for both small and large resistivity. The validity of the numerical solutions was tested by verifying that the total energy and the magnetic helicity are conserved. The total energy dissipation rate decreases as the tearing mode approached its saturated state.

In Chapter 5 the reconnection of two-dimensional stressed x-type neutral point magnetic fields is studied via solution of the nonlinear resistive MHD equations and by analytical solution of the linear eigenvalue problem. For nearly azimuthally symmetric perturbations with conducting boundary condition, the fields relax incompressibly to the unstressed force-free x-type neutral point at a rate close to that predicted by the linear theory. The linear dispersion relation is derived and solved, and the results compared to compressible and incompressible MHD simulations. A faster reconnection rate is found for

azimuthally non-symmetric perturbations. When flow through the boundaries is allowed and the fields at the boundaries are free to adjust we find that the perturbed x-point evolves into a sheet current.

Chapter 2

Linear Evolution of the Tearing Mode with Equilibrium Shear Flow and Viscosity

2.1 Introduction

The linear theory of the tearing mode instability was first developed by Furth, Killeen and Rosenbluth in 1963 (hereafter FKR). They solved the linearized MHD equations using the boundary layer approach. Numerical techniques for the solution of the linear equations were subsequently applied to the problem (Killeen,1970). FKR theory has been widely used and applied to laboratory plasmas and fusion experiments in various geometries. Numerical computations of linear tearing mode instability have been performed by many, in various sub-volumes of parameter space (see, for example, Steinolfson and Van Hoven, 1983) usually without equilibrium shear flow or viscosity effects. The importance of flow and viscosity in the evolution of tearing instability growth rate scaling has been recently shown using both analytical (Chen and Morrison, 1990a, 1990b) and numerical (Einaudi and Rubini, 1986, 1989; Ofman *et al.*, 1991) analyses. Non-homogeneous flows are commonly observed in various phenomena believed to involve reconnection, such as solar coronal loops, solar wind, magnetopause boundary, extragalactic jets and fusion experiments (Priest, 1985; Drake, 1985).

In this chapter the time-dependent equations are solved numerically throughout the entire physical region of instability, in contrast to the bound-

ary layer approach in which solutions of two physically different regions must be matched. This approach enables us to avoid some significant assumptions required by the boundary layer theory, such as constant-ψ or conditions on the growth rate γ (Chen and Morrison, 1990a, 1990b), see also Section 2.3. Thus, we can test the validity of these assumptions and corroborate various scaling laws predicted analytically. Using a finite difference method for the time-dependent problem, we are able to show the spatial and temporal evolution of the perturbed quantities and the dependence on the physical parameters of the problem. Some relevant parameters examined in our study are the normalized wavenumber α, the magnetic Reynolds number S, the shear parameter R, the fluid velocity V (normalized to Alfvén velocity) and the ratio between the viscous and the Alfvén time scales, S_v (i.e., the Reynolds number). By retaining the time dependence, we are able to study cases on a relatively short time scale, such as may be necessary when more then one over-stable mode is present in the solutions. This is particularly significant for the non-linear simulations in which several modes can interact (Steinolfson and Van Hoven, 1984).The results of the linear calculations are later used to initiate the non-linear simulations (see Chapter 4) .

This chapter is organized as follows. In Sec. 2.2 we present the basic equations. In Sec. 2.3 the main results of the linear boundary layer theory are reviewed. In Sec. 2.4 the method of solution is described. Section 2.5 is devoted to the results of numerical computations. Summary and discussion are presented in Sec. 2.6.

2.2 Basic Equations

We use Cartesian geometry and choose an equilibrium magnetic field of the form

$$\mathbf{B}_0(y) = B_{x0}(y)\mathbf{e}_x + B_{z0}(y)\mathbf{e}_z. \tag{2.1}$$

Similarly, the equilibrium plasma flow is assumed to be in the (x, z) plane, with the form

$$\mathbf{V}_0(y) = V_{x0}(y)\mathbf{e}_x + V_{z0}(y)\mathbf{e}_z. \tag{2.2}$$

Equations (1.1)-(1.4) are linearized around the magnetic field and flow velocity equilibrium, solutions assuming perturbations of the form $f_1(y,t)\times exp(ik_x x + ik_z z)$. The normalized linearized time-dependent y-components of the MHD equations can be written as

$$\left(\frac{\partial}{\partial t} + i\alpha G\right)\left(W'' - \alpha^2 W\right) - i\alpha R^2 G'' W = i\alpha F\left(\psi'' - \alpha^2\psi\right) \tag{2.3}$$

$$-i\alpha F''\psi + \frac{1}{S_v}\frac{\partial^4 W}{\partial y^4}$$

$$\left(\frac{\partial}{\partial t} + i\alpha G\right)\psi - i\alpha F W = \frac{1}{S}\left(\psi'' - \alpha^2\psi\right), \tag{2.4}$$

where the dimensionless variables are t in units of τ_h, y in units of a_b, and the perturbed physical quantities $\psi = B_{y1}/B$, $W = V_{y1}/V_a$, and the primes denote the derivatives with respect to y. Also, the dimensionless parameters are the magnetic Reynolds number $S = \tau_r/\tau_h$, a measure of viscosity $S_v = \tau_v/\tau_h$, the shear parameter $R = a_b/a_v$ and the normalized wave number $\alpha = ka_b$. The relevant time scales in these definitions are the resistive time τ_r, the Alfvén time

τ_h and the viscous time τ_v given by $\tau_v = \rho a_b^2/\nu$, $\tau_r = 4\pi a_b^2/c^2\eta$, $\tau_h = a_b\sqrt{4\pi\rho}/B$ and in the above quantities a_b is the magnetic length scale, a_v is the velocity length scale, V_a is the Alfvén velocity and B is a measure of the magnetic field.

The quantities F and G are the normalized equilibrium magnetic and velocity field, respectively, in the x-direction. We assume that F is given by

$$F(y) = \tanh(y) \tag{2.5}$$

and present results for each of the following velocity profiles

$$G(y) = V\tanh(Ry) \tag{2.6}$$

or

$$G(y) = V\{1 - \mathrm{sech}\,(Ry)\}, \tag{2.7}$$

where V is the velocity parameter in units of the Alfvén velocity V_a. Hereafter we refer to Eq. (2.6) as the tanh velocity profile and to Eq. (2.7) as the sech velocity profile. The geometry of the tearing mode in Cartesian coordinates, and the equilibrium quantities are shown in Fig. 2.1. In Fig. 2.1a , the tanh velocity profile is shown, thus V_0 and B_0 have the same dependence on y. The two flow profiles and their derivatives (i.e., flow shear) are shown in Fig. 2.1b. It is evident that the tanh flow profile has the largest shear at $y = 0$ (the tearing layer), and the sech flow has the largest shear away from the tearing layer.

Equations (2.3) and (2.4) are solved numerically without any further approximations. They are subject to the boundary conditions that $W, \psi \rightarrow 0$ exponentially when $y \rightarrow \infty$. For the numerical simulation limited to finite boundaries located at y_1 and y_2, the above boundary conditions become

$$W'(y_{1,2}) = \pm\alpha W(y_{1,2}) \tag{2.8}$$

$$\psi'(y_{1,2}) = \pm\alpha\psi(y_{1,2}), \tag{2.9}$$

where primes denote the derivatives with respect to y taken at the left (y_1) and right (y_2) boundaries of the physical region.

2.3 Linear Theory

The growth rates of the instability can be found from the time-Fourier-transformed Equations (2.3)-(2.4), using the boundary layer approach (FKR; Chen and Morrison,1990a, 1990b; Porcelli, 1987; Paris and Sy, 1983; Dobrovolny *et al.*, 1983). Assuming perturbations of the form $f_1(y)exp(iwt+ik_x x)$ these equations become

$$(\gamma + i\alpha G)\left(W'' - \alpha^2 W\right) - i\alpha R^2 G'' W = i\alpha F\left(\psi'' - \alpha^2\psi\right) \tag{2.10}$$

$$-i\alpha F''\psi + \frac{1}{S_v}\frac{\partial^4 W}{\partial y^4}$$

$$(\gamma + i\alpha G)\,\psi - i\alpha F W = \frac{1}{S}\left(\psi'' - \alpha^2\psi\right), \tag{2.11}$$

where $\gamma = \gamma_R + i\gamma_I = i\omega\tau_h$ is the complex growth rate and the subscripts R and I denote real and imaginary parts, respectively.

The physical region is divided in two regions, namely, an inner region in which $|F| << 1$ and resistivity cannot be neglected [e.g., near $y = 0$, for

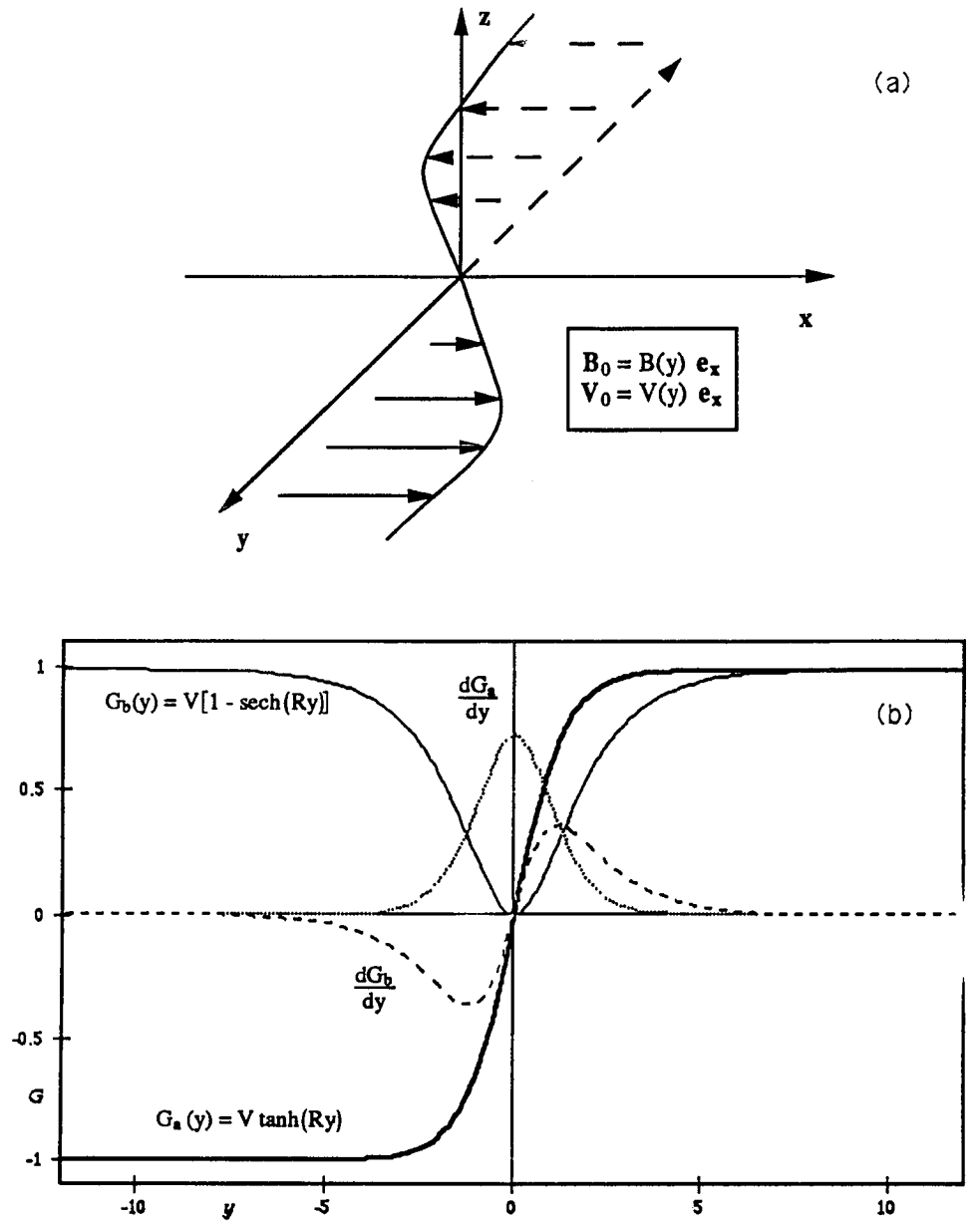

Figure 2.1: The initial equilibrium magnetic field and flow.
(a) The tanh dependence on y for $\mathbf{B}_{x0}$ and$\mathbf{V}_{x0}$. (b) Equilibrium flow profiles $G(y)$ and their derivatives used in the present work.

$F(y)$ as in (2.5)] , and an outer region in which the resistivity can be neglected in Ohm's law. In the inner singular layer, one can substitute $F' = F'(0), F'' = F''(0), G' = G'(0), G'' = G''(0)$, and $F = yF'$. The solutions in the outer and the inner regions are matched continuously through a matching parameter

$$\Delta' = \frac{\psi_2'}{\psi_2} - \frac{\psi_1'}{\psi_1}, \tag{2.12}$$

where the subscripts 1 and 2 denote values at the boundaries of the inner singular layer of width ϵ, respectively. An important result obtained by Chen and Morrison (1990a), is that that flow in the outer region can drastically change the matching quantity Δ'. In fact, alteration of the external flow profile can effect the transition from constant-ψ to nonconstant-ψ tearing. A numerical estimate of Δ' is discussed in Section 2.5. The FKR result, without shear flow or viscosity is

$$\gamma_R = \omega_I \tau_h \sim S^{-3/5}. \tag{2.13}$$

This scaling can be used as a benchmark for comparison with new numerical results.

The growth rates and their scalings are found by taking the following limits of the parameters:

$$\left|\frac{\gamma}{\alpha F'(0)\epsilon}\right| << 1 \ (slow\ growth), \tag{2.14}$$

$$\left|\frac{\gamma}{\alpha F'(0)\epsilon}\right| \sim 1 \ (fast\ growth), \tag{2.15}$$

$$\left|\frac{G'(0)}{F'(0)}\right| \ll 1 \ (small\ shear), \tag{2.16}$$

$$\left|\frac{G'(0)}{F'(0)}\right| \sim 1 \ (comparable\ shear), \tag{2.17}$$

where ϵ is the width of the tearing layer. The results for the inviscid case, as obtained by Chen and Morrison (1990a), are summarized in Table 2.1. For the nonconstant-ψ tearing mode and small or comparable shear (2.16)-(2.17), the growth rate scaling is

$$\gamma_R \sim \alpha^{2/3} S^{-1/3}. \tag{2.18}$$

In the case of the constant-ψ tearing mode when the velocity shear is comparable to the magnetic shear, i.e. (2.17) is satisfied, the growth rate scales as

$$\gamma_R \sim \alpha^{1/2} S^{-1/2}. \tag{2.19}$$

When viscosity is present and the condition $\left|\frac{G'(0)}{F'(0)}\right| < 1$ is satisfied, the scaling (2.19) is modified to

$$\gamma_R \sim S^{-2/3} Q^{1/3} \left[4\frac{S}{S_v} + \frac{G'(0)^2}{F'(0)^2}\left(1 - \frac{S}{S_v}\right)^2 \right]^{-1/6}, \tag{2.20}$$

where $Q \equiv \alpha F'(0)\left(1 - \frac{G'(0)^2}{F'(0)^2}\right)$. As $\left|\frac{G'(0)}{F'(0)}\right| \to 1$, the growth rate approaches zero as $Q^{1/3}$. When $\left|\frac{G'(0)}{F'(0)}\right| > 1$, the tearing mode disappears, and Kelvin-Helmholtz (K-H) instability effects are present. When the shear is very small (2.16), the growth rate scaling (2.13) becomes

$$\gamma_R \sim [\alpha F'(0)]^{1/3} S^{-2/3} \left(\frac{S_v}{S}\right)^{1/6}. \tag{2.21}$$

The dependence of the growth rate on S, S_v and $\left|\frac{G'(0)}{F'(0)}\right|$ in Eqs. (2.18)-(2.21) has been verified numerically. These results will be presented in Sec. 2.5.

2.4 Method of Solution

We solve Equations (2.3) and (2.4) using an implicit finite difference scheme (Killeen, 1970; Steinolfson and Van Hoven, 1983) with a variable spatial

Table 2.1: Summary of the effects of equilibrium shear flow on the tearing mode. (From Chen and Morrison, 1990a.)

Constant-ψ tearing mode	Nonconstant-ψ tearing mode
$\left\|\frac{G'(0)}{F'(0)}\right\| \ll 1$ (a) The growth rate and scale length of the resistive region are, respectively, $\gamma \sim \alpha^{2/5}\Delta'^{4/5}S^{-3/5}$, $\epsilon \sim (\alpha S)^{-2/5}\Delta'^{1/5} \ll 1$ (b) The constant-ψ approximation is valid if $\epsilon\|\Delta'\| \ll 1$ (c) Small flow shear $G'(0)$ destabilizes the constant-ψ tearing mode	(a) The growth rate and scale length of the resistive region are, respectively, $\gamma \sim \alpha^{2/3}S^{-1/3}$ $\epsilon \sim (\alpha S)^{-1/3} \ll 1$ (b) In this limit, we have $\epsilon\|\Delta'\| \gg 1$ $1 - G'(0)^2/F'(0)^2 \neq 1$ (c) Small flow shear $G'(0)$ stabilizes the constant-ψ tearing mode with sufficiently large Δ'
$\left\|\frac{G'(0)}{F'(0)}\right\| \leq 1$ (a) The growth rate and scale length of the resistive region are, respectively, $\gamma \sim (\alpha\|\Delta'\|)^{1/2}S^{-1/2}$ $\epsilon \sim (\alpha S)^{-1/3} \ll 1$ (b) If $G'(0)G''(0) - F'(0)F''(0) \neq 0$, $\Delta' > 0$ instability criterion is removed (c) The constant-ψ approximation is valid if $\left\|\sqrt{[1 - G'(0)^2/F'(0)^2]\,\Delta'\epsilon}\right\| \ll 1$	(d) There exists a transition to ideal instability when Δ' becomes negative through $\Delta' = \infty$ (which is made possible by the flow on the external region)
$\left\|\frac{G'(0)}{F'(0)}\right\| > 1$ stabilized	stabilized

grid. The following system of finite difference equations in the complex plane, which accommodate flow and viscosity, are solved numerically:

$$-\frac{i\alpha F_j}{2\Delta y_j \Delta y_+}\psi_{j+1}^{n+1} + i\left(\frac{\alpha F_j}{\Delta y_+ \Delta y_-} + \frac{\alpha^3}{2}F_j + \frac{\alpha F_j''}{2}\right)\psi_j^{n+1} - \frac{i\alpha F_j}{2\Delta y_j \Delta y_-}\psi_{j-1}^{n+1}$$

$$-\frac{1}{2S_v \Delta y_j \Delta y_+}Z_{j+1}^{n+1} + \left(\frac{1}{\Delta t} + \frac{i\alpha}{2}G_j + \frac{1}{S_v \Delta y_+ \Delta y_-}\right)Z_j^{n+1} - \frac{1}{2S_v \Delta y_j \Delta y_-}Z_{j-1}^{n+1}$$

$$-\left(\frac{\alpha^2}{\Delta t} + \frac{i\alpha^3}{2}G_j + \frac{i\alpha}{2}R^2 G_j''\right)W_j^{n+1} = k_j^n \tag{2.22}$$

$$-\frac{1}{2S\Delta y_j \Delta y_+}\psi_{j+1}^{n+1} + \left(\frac{1}{\Delta t} + \frac{i\alpha}{2}G_j + \frac{1}{S\Delta y_+ \Delta y_-} + \frac{\alpha^2}{2S}\right)\psi_j^{n+1}$$

$$-\frac{1}{2S\Delta y_j \Delta y_-}\psi_{j-1}^{n+1} - \frac{i\alpha}{2}F_j W_j^{n+1} = d_j^n \tag{2.23}$$

$$Z_j^{n+1} - \frac{1}{\Delta y_j \Delta y_+}W_{j+1}^{n+1} + \frac{2}{\Delta y_+ \Delta y_-}W_j^{n+1} - \frac{1}{\Delta y_j \Delta y_-}W_{j-1}^{n+1} = q_j^n, \tag{2.24}$$

where $\Delta y_j = (y_{j+1} - y_{j-1})/2$, $\Delta y_+ = y_{j+1} - y_j$, $\Delta y_- = y_j - y_{j-1}$. The variable grid spacing Δy_j expands from a minimum of $\Delta y_{min} = 10^{-5}$ near the singular surface to $\Delta y_{max} = 0.5$ near the computational boundaries according to the prescription $\Delta y_j = \Delta y_{max}\left(\frac{\Delta y_{min}}{\Delta y_{max}}\right)^{(J-j)/(J-1)}$, where J denotes the boundary grid point. Up to 240 grid points were used.

The purpose of Eq. (2.24), which is a finite difference form of $Z(t,y) - W''(t,y) = 0$, is to enable the numerical calculation of the fourth order viscous term $\frac{1}{S_v}\frac{\partial^4 W}{\partial y^4}$ in Eq. (2.3), while maintaining the tridiagonal form of the finite difference equations:

$$-A_j U_{j+1}^{n+1} + B_j U_j^{n+1} - C_j U_{j-1}^{n+1} = P_j^n, \tag{2.25}$$

where A, B, C are 3 by 3 matrices and U, P are 3-dimensional vectors. Equation (2.25) is solved for U by using Gaussian elimination.

The time step Δt was selected so that $\Delta t \leq min\{(\gamma_R)^{-1}, (5\gamma_I)^{-1}\}$, and the simulation was evolved for N time steps until only the fastest growing mode is present in the solutions. Usually the number of time steps satisfied $50 < N < 500$.

From the complex solutions $W(t,y)$ and $\psi(t,y)$, which are symmetric or antisymmetric relative to $y = 0$ [the symmetries are determined by the functions $F(y)$ and $G(y)$ in Eqs. (2.3)-(2.4)], the growth rates were obtained in two steps (see Fig. 2.2). First, the real part of the growth rate γ_R is found by fitting a straight line to the logarithm of $W(t,y_0)$ (where y_0 is an arbitrary point in the domain). Next, the exponential trend is removed from the solutions and a Fast Fourier Transform (FFT) is performed on the remaining oscillatory part of $W(t,y_0)$, which thereby determines the imaginary part of the growth rate γ_I. If more than one overstable mode is present at the same time, the result of the FFT will show a corresponding number of well defined peaks, indicating the values of the γ_I. This occurs when the real parts of the two modes have very close values:

$$exp(\gamma_{R1} t_m) exp(-\gamma_{R2} t_m) \sim 1, \tag{2.26}$$

where $t_m = N\Delta t$. If the modes are purely growing (no time-dependent oscillations are present), then only the first step in the above method is performed.

2.5 Numerical Results

The method of finding the complex growth rate (Sec. 2.4) is clarified in Fig. 2.2. In Figs. 2.3-2.11 we present the results of computer simulations of tearing mode instability. In Figs. 2.3-2.5 the spatial behavior of the complex

solutions $W(t_0, y)$ and $\psi(t_0, y)$, normalized to their respective peak values, is presented. In what follows, we have used the normalizations $\psi = B_{y1}/B_{y1max}$ and $W = -iV_{y1}/V_{y1max}$, where the absolute maximal values are given in Table 2.2. Figures 2.6, 2.8-2.10 show the various scalings of the growth rate, as in Eqs. (2.18)-(2.21). In Fig. 2.7, the dependence of the growth rate γ on the shear parameter R, for sech and tanh flow profiles is shown.

In Figs. 2.3 and 2.4 the constant-ψ solutions are shown. This is clearly seen from the fact that the tearing layer, defined by the inner peak of W_R, is located in a region where ψ_R is constant. The presence of flow introduces the imaginary parts of the perturbed quantities and the outer peak in W_R, as compared to FKR type solutions (see, for example, Steinolfson and Van Hoven, 1983). The inviscid solutions in Figs. 2.3a and 2.4a agree with the results in Einaudi and Rubini (1986). The figures of the eigenfunctions as given by Einaudi and Rubini are drawn with a linear scale in the y-direction, rather than logarithmic scale used in this chapter. In Fig. 2.3a the equilibrium magnetic field was (2.5), the flow profile was tanh (2.6), and the velocity shear, determined by $V = 1.0$ and $R = 0.73$, was comparable to the magnetic field shear. The antisymmetric solutions, namely, W_R (short dashes line) and ψ_I (long dashes line), for the positive and negative values of y are plotted on the positive logarithmic y axis. The solutions in Fig. 2.3b are for the same parameters as in Fig. 2.3a, but they include viscosity comparable to resistivity $S = S_v = 10^6$. Its effect is to reduce W_R and ψ_I relative to ψ_R (see Table 2.2) and therefore, reduce the reconnecting fields and the growth rate. Figures 2.4a-2.4b show the behavior for a sech equilibrium flow. In Fig. 2.4b the antisymmetric solutions are W_R and W_I (dashed line). The solid line is ψ_R and in this case it merges with the

Table 2.2: The maximal absolute values of the solutions in Figs. 2.3-2.5.

	Fig. 2.3a	Fig. 2.3b	Fig. 2.4a	Fig. 2.4b	Fig. 2.5a	Fig. 2.5b
ψ_R	1.000	1.000	1.000	1.000	1.000	1.000
ψ_I	0.145	0.129	0.218	0.049	1.798	2.156
W_R	0.145	0.129	0.060	0.014	1.851	2.166
W_R	0.897	0.898	0.271	0.271	0.984	1.081

normalized ψ_I that has similar shape. The effect of viscosity on this solution is shown in Fig. 2.4b. The inner peak of W_I has practically disappeared, and the growth rate is smaller than in Fig. 2.4a.

In Figs. 2.5a-2.5b a nonconstant-ψ tearing mode is shown. In other words, most of the spatial variation of the perturbed flow W_R is confined to the region of the maximal variation of ψ_R. Viscosity, in Fig. 2.5b adds additional features to the eigenfunctions, reducing slightly the growth rate. The more complex dependence of the solutions on y is due to the mixing of Kelvin-Helmholtz and tearing instabilities.

The scaling of the growth rates for the inviscid case is presented in Fig. 2.6. The lower line represents the analytical scaling and has a slope of $-1/2$ on a log-log scale. It fits very well the calculated points that were obtained from the type of solutions shown in Fig. 2.3a, having values of resistivity $S = 10^3 - 10^7$, and it agrees with the analytical results in Table 2.1 for the constant-ψ case. The lower the resistivity (higher S), the closer the inner peaks of W_R and ψ_I are to the singular surface $y = 0$, while W_I and ψ_R remain almost unaffected. This result is expected from the analytic scaling of the inner layer width $\epsilon \sim S^{-2/5}$ (small shear, Fig. 2.6b) and $\epsilon \sim S^{-1/3}$ (high shear). The upper line of Fig. 2.6a has a slope of $-1/3$, in good agreement with the calculated points from the solutions shown in Fig. 2.5a and the nonconstant-ψ tearing mode (Table 2.1).

The dashed curve is the imaginary part of γ for the nonconstant-ψ case. The oscillations of the fluid appear due to K-H instability and therefore exhibit a different behavior than γ_R that is dominated by tearing.

The dependence of the growth rate on the shear parameter R is shown in Fig. 2.7 for tanh flow profile (empty circles), and sech profile (full circles). Here γ_R agrees with Einaudi and Rubini (who used a different numerical approach). For small values of R the FKR growth rate is recovered. When R is of order unity ($R = 0.73$), the tanh profile, produces a peak in the growth rate, which satisfies conditions (2.15), (2.17) and scales as $S^{-1/2}$ in (2.19). The sech profile, produces a different behavior for $R > 1$, namely the solutions become non constant-ψ solutions and the tearing mode is further destabilized. The nonconstant-ψ is most evident for $2 < R < 3$ with $V = 1.0$. At $R > 4$ a transition to ideal K-H instability occurs (Einaudi and Rubini, 1986, Chen and Morrison, 1990a). The oscillating part appears in the nonconstant-ψ regime and reaches its peak value near the transition point to ideal instability.

The matching quantity Δ' was estimated numerically for the solution in Figs. 2.3-2.5 by calculating ψ'/ψ near the singular layer. It was found that Δ' is drastically affected by the flow in the outer region (e.g. by the value of R), while almost unaffected by the resistivity. For the constant-ψ case $\Delta' \sim O(10)$ and for nonconstant-ψ case $\Delta' \sim O(100)$ in agreement with the analytical calculation of Chen and Morrison (1990a).

When the viscosity is comparable to or larger than resistivity, and no shear flow is present, the classical FKR scaling (2.13) changes to (2.21). In Fig. 2.8 the dependence of the growth rate on S_v is shown. The line with the theoretical slope of 1/6 agrees with the calculated points, which have a least

mean square slope of 0.168. In Fig. 2.9 the dependence of the growth rate on Q (Eq. 17c) is verified and is found to agree well with the analytical result in the range $0.02 < Q < 0.2$. When Q is very small, the influence of flow on the matching quantity Δ' should be accounted for in the analytical growth rate scaling, thereby modifying (2.20). (Note that in the numerical solutions, ψ and ψ' are continuous everywhere, therefore Δ' is not well-defined).

The dependence of the growth rate on viscosity for the sech profile is presented in Fig. 2.10. For $R = 0.44, V = 1.0$ the analytical scaling of $S_v^{1/6}$ is recovered (lower straight line). For $R = 6$ (high shear) the tearing mode is stabilized, and the instability becomes a Kelvin-Helmholtz mode. The K-H instability is practically unaffected by intermediate to low viscosity ($S_v = 10^4 - 10^8$), but for higher viscosity, when the viscous time scale is comparable to the instability growth time scale, the mode is stabilized ($S_v < 10^3$) in agreement with the results found by Einaudi and Rubini (1989). It is interesting to note that the imaginary part of the growth rate exhibits similar behavior to the real part, unlike γ_I in Fig. 2.6 where both K-H and tearing instabilities are present.

In Fig. 2.11 an example of the dependence of γ_I on viscosity is shown. For the sech flow profile, $R = 6$ and $S_v = 10^6$ (Fig. 2.11a) only one value for γ_I is found, and it corresponds to the fastest growing mode. When the viscosity is increased and $S_v = 10^5$, two overstable modes are present in the solution (Fig. 2.11b) due to condition (2.26). The growth rate of the fastest growing mode for this value of viscosity has a local minimum (with respect to S_v), and is shown in Fig. 2.10. When the viscosity is further increased to $S_v = 10^4$, the difference between γ_{R1} and γ_{R2} increases, and the magnitude of the second mode in Fig. 2.11c becomes very small compared to the fastest growing mode.

The boundary conditions in the above solutions required exponential decay of the solutions to zero at infinity, Eqs. (2.8)-(2.9). We have found that using conducting wall boundary conditions at large $y \geq 10$ would not change the results significantly.

2.6 Summary and Discussion

The results of an analytic boundary layer approach were compared to numerical solutions of the time-dependent, linearized, resistive, and viscous MHD equations (2.3)-(2.4) for various values of the parameters α, R, V, S and S_v. In general, a very good agreement with the analytical growth rate scalings was found. Therefore, the approximations used in analytical theory to find the growth rate scalings are found to hold. The spatial variations of the solutions, that were not found analytically for the viscous and inviscid cases with flow, have been presented. A nonconstant-ψ tearing mode and its parameter range have been found numerically to be in agreement with the analytical predictions. The numerical growth rate scalings have been calculated and found to agree with the analytical ones, within the given range of their parameters. The time dependent linearized MHD Equations (2.3)-(2.4) for tearing mode instability were solved numerically, without further approximations, in the region of interest. An implicit variable grid tridiagonal finite difference scheme was used to obtain the numerical solutions, and Fast Fourier Transform techniques were used to find the imaginary part of the growth rate after the real part, the exponential growth rate γ_R was found. When the shear flow was very small ($V < 0.1$, $R < 0.1$), in the inviscid case the classical FKR growth rate and inner layer scalings were recovered. When viscosity is present, the growth rate

scaling is changed to $\gamma_r \sim S^{-2/3}\left(\frac{S_v}{S}\right)^{1/6}$. For the tanh profile, when the shear flow was large, i.e. $\left|\frac{G'(0)}{F'(0)}\right| \sim 1$ and $S_v = S$ it has been verified that the growth rate scales as $\gamma_R \sim \left[1-\left(\frac{G'(0)}{F'(0)}\right)^2\right]^{1/3}$. For the sech profile, a transition from the constant-ψ to non constant-ψ tearing mode was observed to be driven by the flow in the outer region (outside of the tearing layer). In particular for $\alpha = 0.5$, $S = 10^6$, $V = 1.0$ and $2 < R < 3$ the nonconstant-ψ tearing mode is obtained, with the analytically predicted growth rate scaling $\gamma_R \sim S^{-1/3}$. In case of the tearing mode, small and intermediate values of viscosity , $S_v = 10^7 - 10^3$, lower the growth rate. For the sech profile and $R > 4$, Kelvin-Helmholtz instability is dominant; it is stabilized for higher values of viscosity ($S_v < 10^3$) when the viscous time scale is comparable to the growth time scale. The advantage of the time dependent approach over time independent methods (such as those used by Einaudi and Rubini, 1986,1989) is clearly seen when relatively short time scale simulations are performed, where more then one oscillating mode in the magnetic and velocity perturbations is present. This is particularly important for the generalization of the problem to non-linear studies (see Steinolfson and Van Hoven, 1984, and Chapter 4).

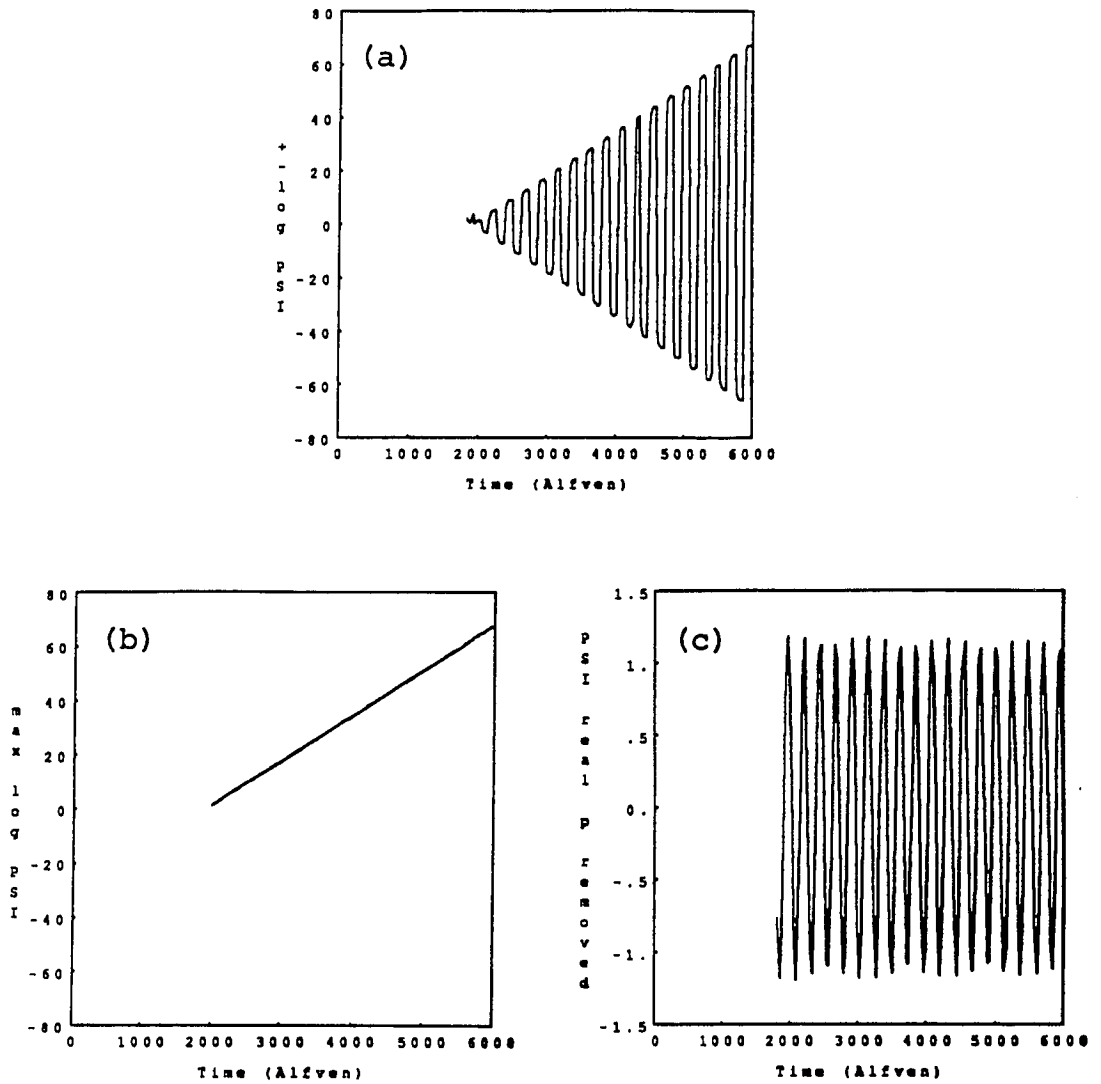

Figure 2.2: The oscillating and exponentially growing components of the solutions.
(a) The time dependent solution $\pm \log |\psi_R(t, y_0)|$. (b) The linear fit to the maxima of $\log |\psi_R(t, y_0)|$. The slope of this line determines γ_R. (c) The solution $\psi_R(t, y_0)$, with only the oscillatory part remaining. Performing FFT on it determines γ_I. Note that the initial transition time of $1500\tau_h$ was removed from the calculations.

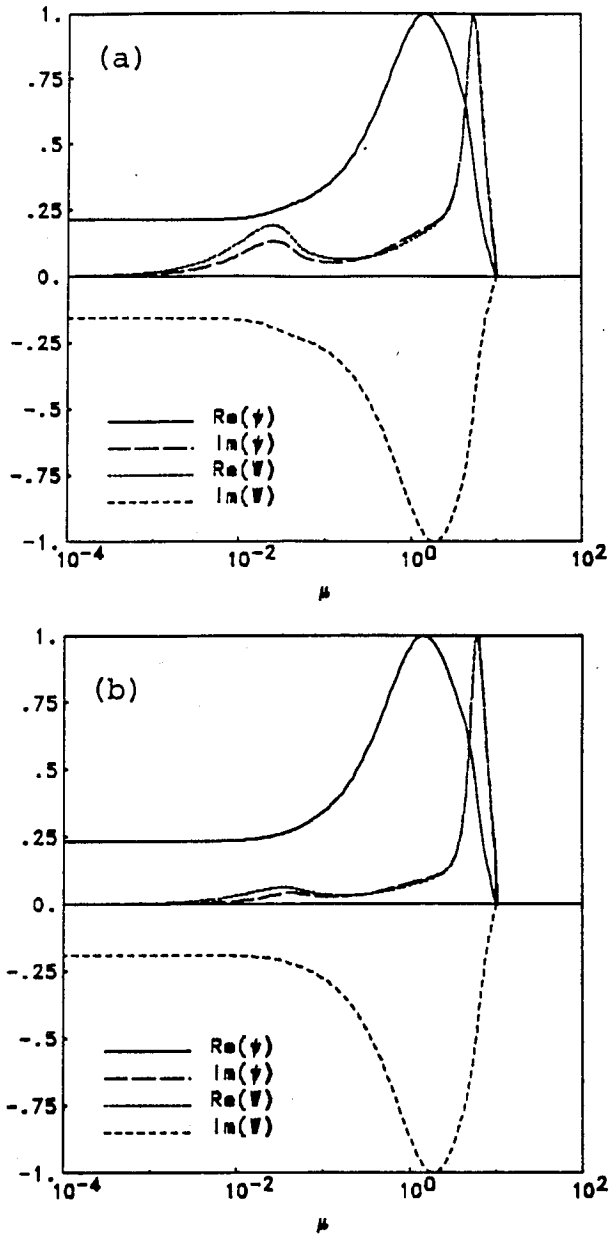

Figure 2.3: The spatial variations of the complex solutions W and ψ (inviscid case) normalized to their peak values. The equilibrium flow is $G = V\tanh(Ry)$. The parameters are (a) $V = 1$, $R = 0.73$, $S = 10^6$, $\alpha = 0.5$, and no viscosity. (b) Same as (a) except with viscosity $S_v = 10^6$.

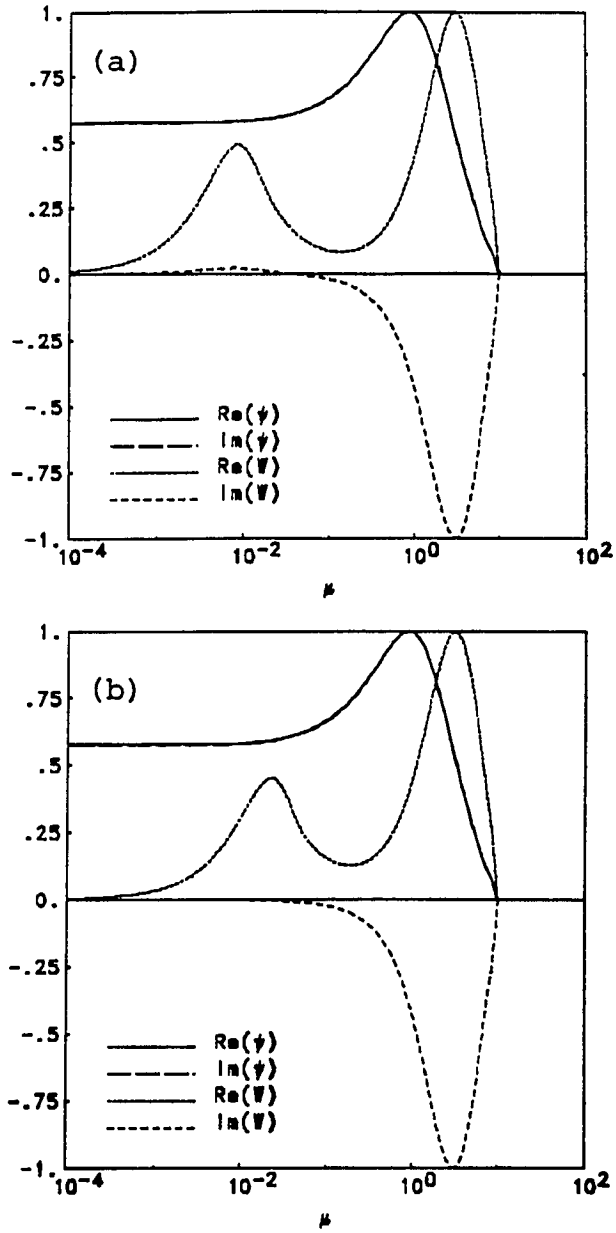

Figure 2.4: Plot of W and ψ as in Fig 2.2 except the equilibrium flow is $G = V\mathrm{sech}\,(Ry)$.
The parameters are (a) $V = 1$, $R = 0.44$, $S = 10^6$, $\alpha = 0.5$, and no viscosity. (b) Same as (a) except with viscosity $S_v = 10^6$.

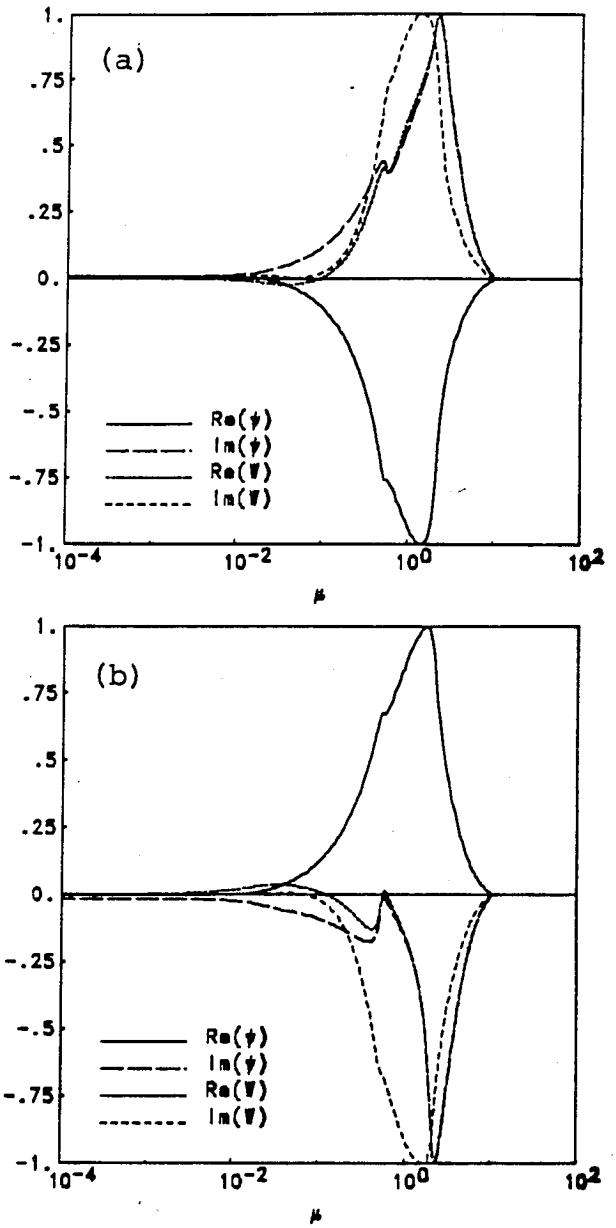

Figure 2.5: Same as Fig. 2.3a with (a) $R = 2.5$. (b) Same as Fig. 2.3b with $R = 2.5$.

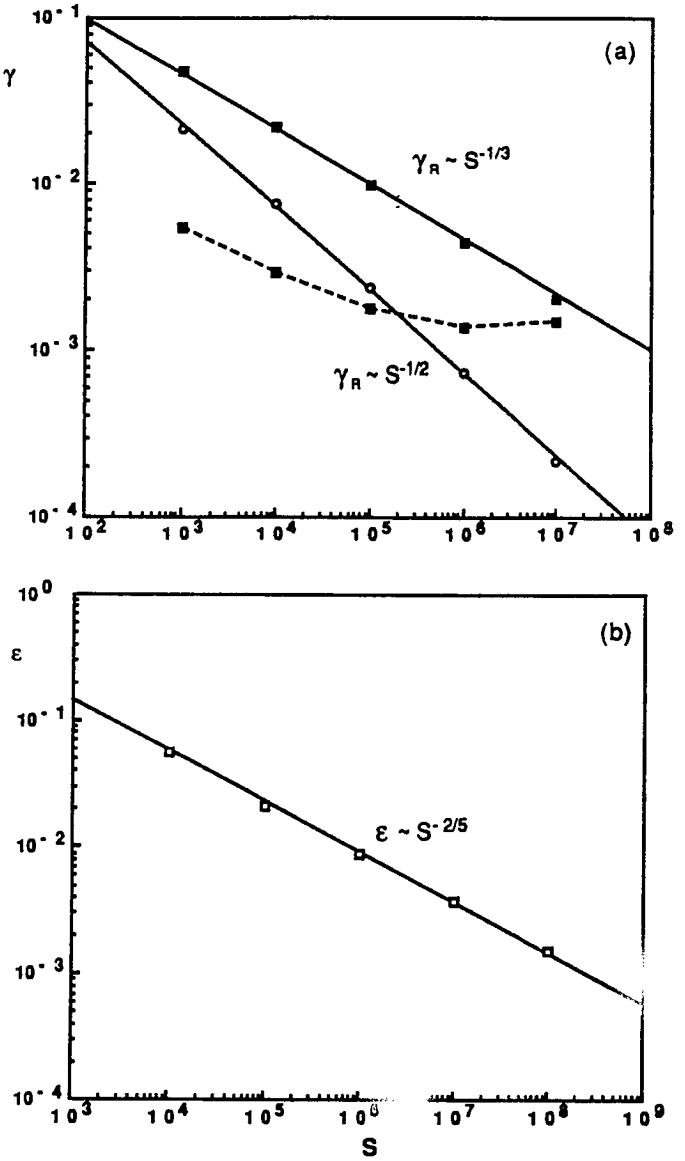

Figure 2.6: Growth rate scaling with S.
(a) $V = 1$, $R = 2.5$, $\alpha = 0.5$ and the sech flow profile, the non constant-ψ case (the squares are the calculated points). The scaling for $V = 1$, $R = 0.73$, $\alpha = 0.5$ and the tanh flow profile (the circles are the calculated points). (b) The scaling with S of the inner layer width ϵ, as defined by the inner peak of W_R, for the tanh profile with the parameters $V = 0.1$ and $R = 0.5$

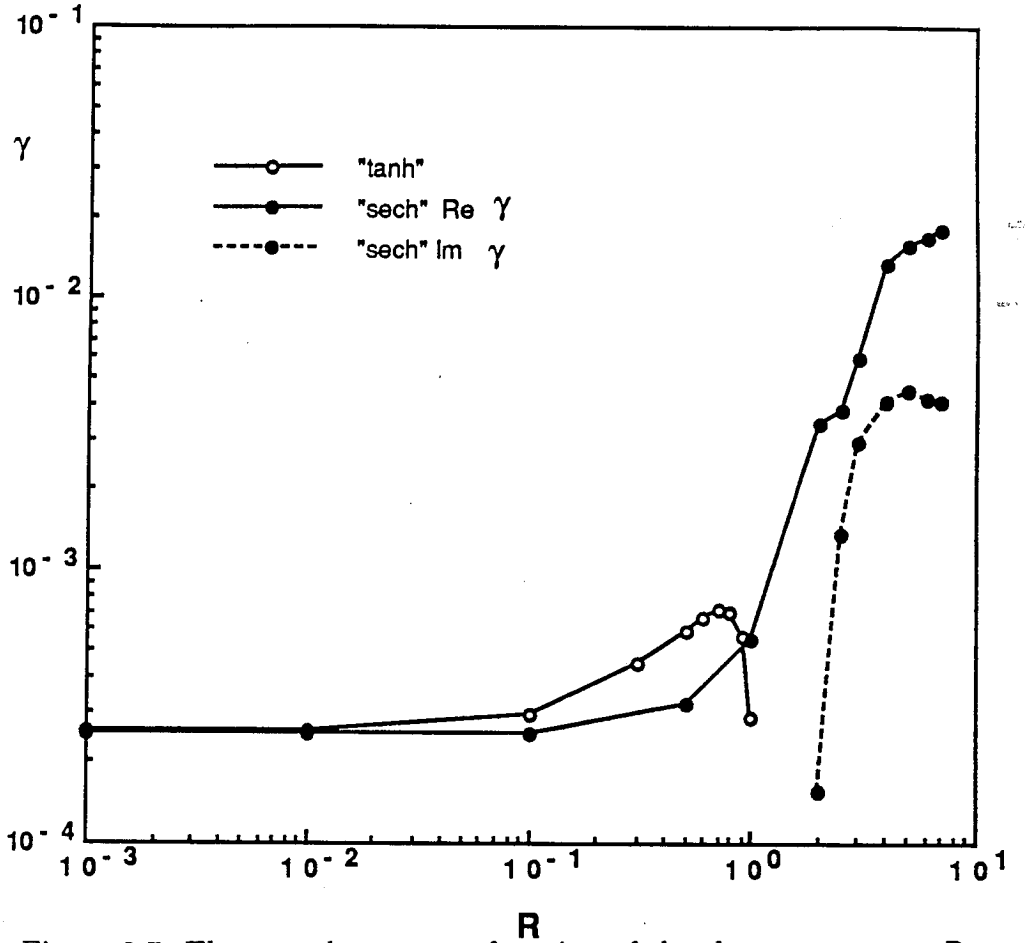

Figure 2.7: The growth rate as a function of the shear parameter R. The parameters are $S = 10^6$, $V = 1$, $\alpha = 0.5$, for the tanh (empty circles) and sech (full circles) equilibrium flows. The peak is located at $R = 0.73$. For small values of R, the FKR growth rate is recovered.

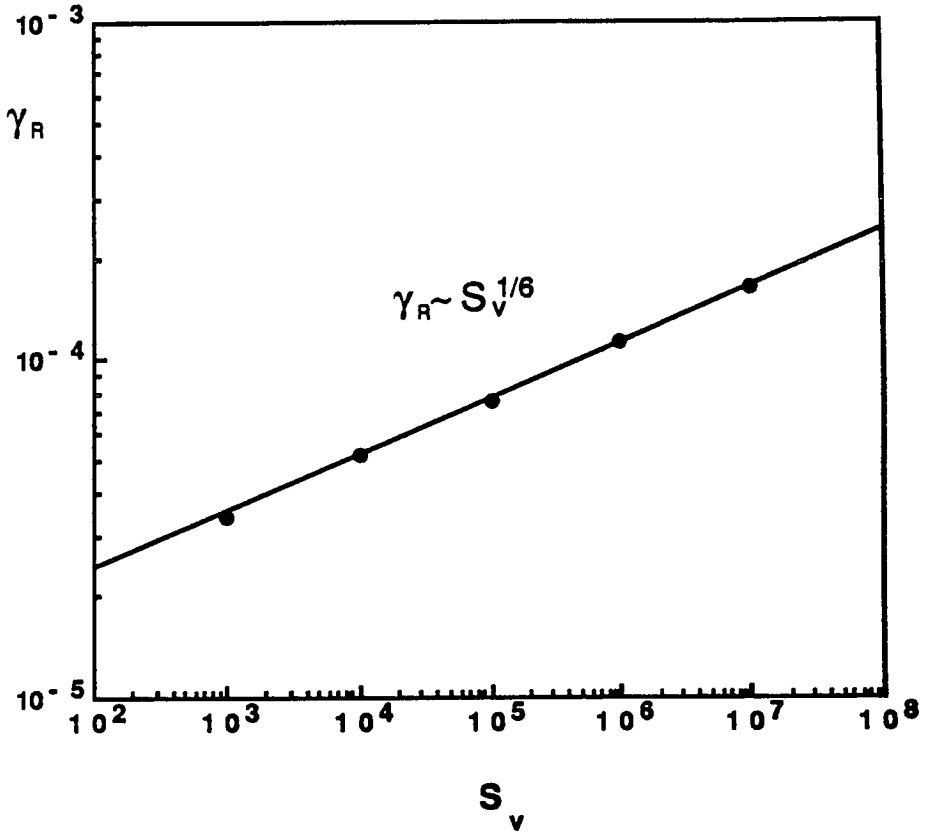

Figure 2.8: Calculated numerical growth rate scaling with viscosity parameter S_v.
The other parameters are $S = 10^6$, $V = 0$, $\alpha = 0.5$.

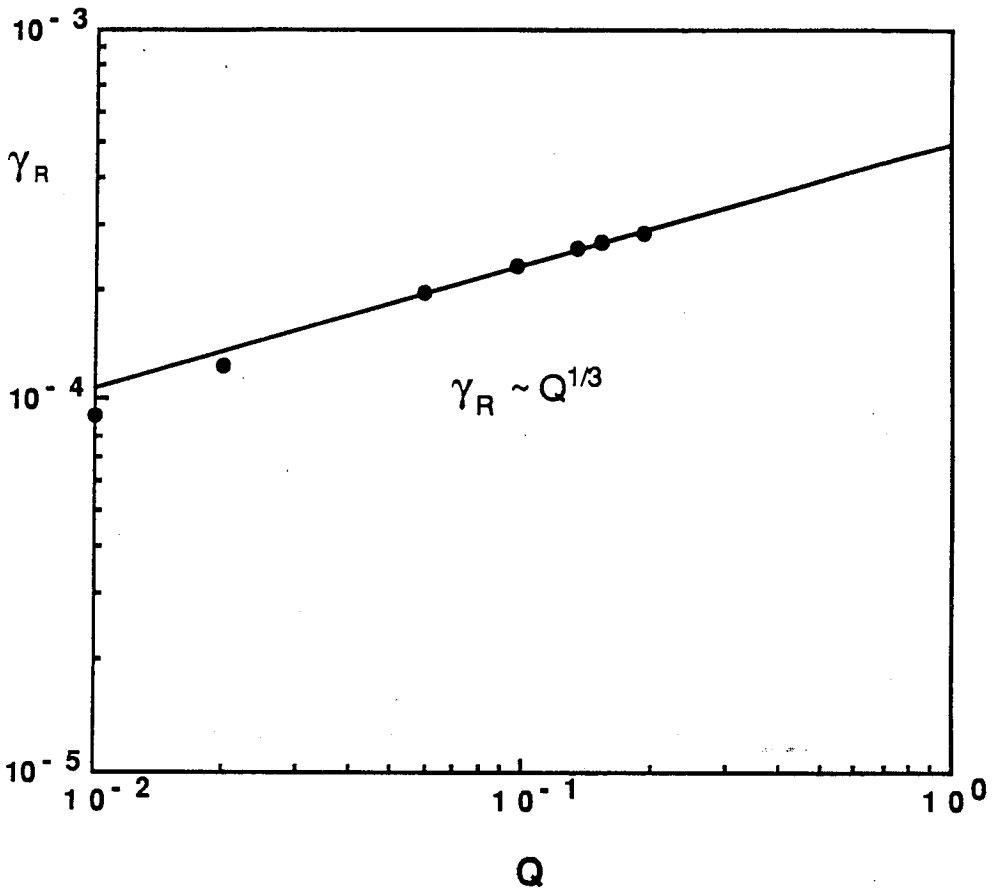

Figure 2.9: The dependence of the growth rate on Q.
The parameters are$S = S_v = 10^6$, $V = 1$, $\alpha = 0.5$. The straight line represents the analytical dependence of $Q^{1/3}$.

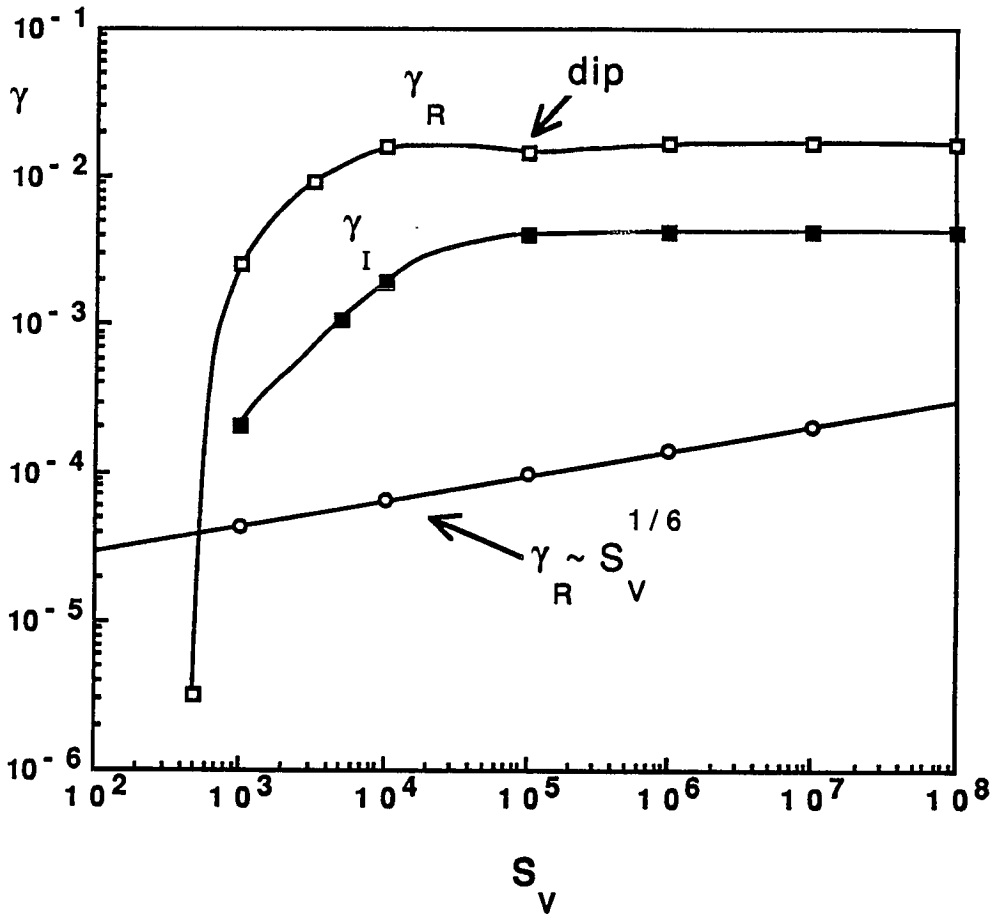

Figure 2.10: The dependence of the growth rate on S_v for sech flow profile and small shear.
The parameters are $V = 1$, $R = 0.44$, $\alpha = 0.5$. The analytical scaling is recovered (empty circles). For $R = 6$, the transition to ideal Kelvin-Helmholtz instability occurs (the squares are the calculated points).

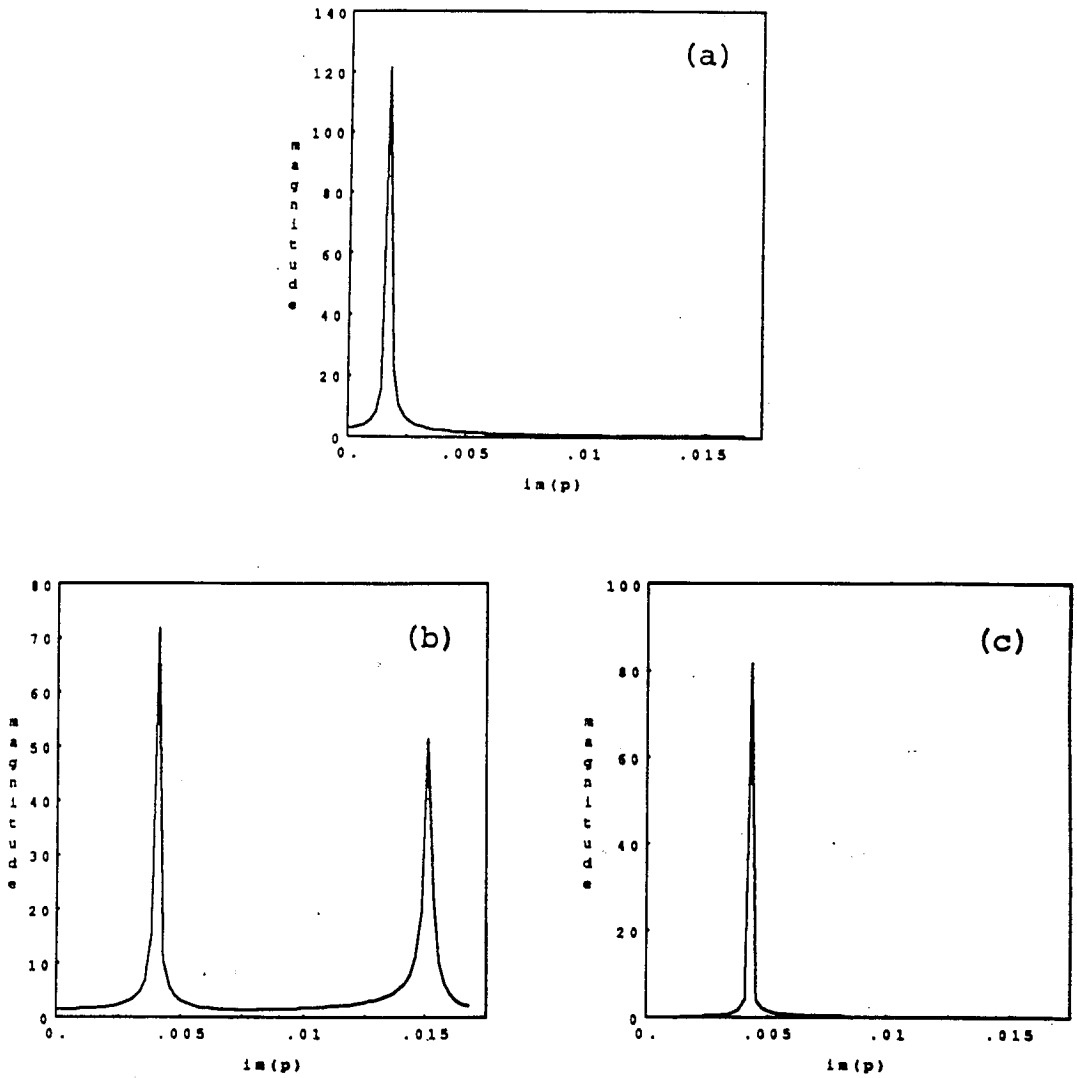

Figure 2.11: The value of γ_I and its magnitude calculated with FFT for sech flow profile.
(a) $V = 1$, $R = 6$, $S = S_v = 10^6$, $\alpha = 0.5$. (b) same as (a) with $S_v = 10^5$. (c) same as (a) with $S_v = 10^4$.

Chapter 3

Linear Studies of the Double Tearing Mode with Equilibrium Shear Flow and Viscosity

3.1 Introduction

The double tearing mode requires two tearing layers that are close enough together to allow nonconstant-ψ effects to enhance the growth rate γ. The analytic linear theory of the single tearing mode in slab geometry with equilibrium shear flow and viscosity has been considered by several authors (Dobrowolny *et al.*, 1983; Paris and Sy, 1983; Poricelli, 1987; Chen and Morrison, 1990a, 1990b). They conclude that flows, approaching the Alfvén velocity can greatly modify the stability criteria of the single tearing instability. This was shown to hold numerically in the linear regime in Chapter 2 and by Einuadi and Rubini (1986, 1989), and Ofman *et al.* (1991).

There is evidence that the double tearing instability has been observed in fusion devices with non-monotonic current profiles in the plasma column (Stix, 1976), and it is also believed to be important in solar flares (Spicer, 1977; Priest, 1985). Large shear flow motions have been observed between the footpoints of solar flares, and along the field lines (Wang and Zirin, 1990). The instability without equilibrium shear flow has been studied by several authors (Furth *et al.*, 1973; Lee *et al.*, 1979; Carreras *et al.*, 1979; Dnestrovskii *et al.*, 1979; Pritchett *et al.*,1980; Kerner and Tasso, 1982; Mahajan and Hazeltine, 1982; Gatilov *et al.*, 1989), and has been subject to few experiments.

The effect of equilibrium shear flow on the double tearing mode has not been considered previously, despite the fact that such coupling of shear flow and double tearing may occur in fusion devices and space plasmas, and may alter the behavior of the instability without shear flow considerably. For instance, equilibrium shear flows can partly stabilize the mode, modify the growth rate dispersion relation, and excite temporal oscillations of the perturbed quantities for relatively small values of flow shear at the tearing layers (see, Secs. 3.3-3.4).

Here, the double tearing mode with equilibrium shear flow parallel to the magnetic field is investigated via MHD simulations. The chapter is organized as follows. In Sec. 3.2 the initial magnetic field configuration, the equilibrium shear flow profiles and the boundary conditions that excite the double tearing mode are presented. In Sec. 3.3 the linear growth rate dispersion relation is presented, and in Sec. 3.4 the numerical methods and results are discussed. Section 3.5 is devoted to a summary and interpretation of the results.

3.2 Model Equations

We use the linearized time dependent MHD Equations (2.3)-(2.4) with the following forms of F and G for the double tearing mode:

$$F(y) = 1 - (1 + F_c)\mathrm{sech}\,(y), \tag{3.1}$$

$$G(Ry) = V\left[1 - \mathrm{sech}\,(Ry)\right], \tag{3.2}$$

where $F_c = \cosh(y_s) - 1$ is determined by the locations $\pm y_s$ where $F(y)$ vanishes and therefore where tearing may occur. As in Chapter 2 the velocity parameter V is given in units of V_a. The spatial dependence of F and G for $V = -0.5$, $y_s = 0.75$, and $R = 0.5$ are shown in Fig. 3.1. The particular choice of the

flow profile (3.2) with an even dependence on y is suggested by the types of flows believed to occur in solar coronal loops, (Priest, 1985; Wang and Zirin, 1990) although the actual shear flow profiles are not well known. The relative importance of the flow shear with respect to the magnetic shear at the tearing layers (for symmetric shear profiles) is measured by the parameter R_s as defined by

$$R_s = \left| \frac{G'(Ry)}{F'(y)} \right|_{y=\pm y_s}, \tag{3.3}$$

In Ofman *et al.*. (1991) we have shown numerically that when $R_s > 1$ a transition to the Kelvin-Helmholtz (K-H) will occur. In this study we are interested in the types of flow profiles with the magnetic field profile (3.2) that are not subject to the K-H instability. The dependence of the growth rate on R_s is presented in Sec. 3.4. Equations (2.3) and (2.4) are solved numerically without any further approximations, subject to zero boundary conditions that are equivalent to conducting walls placed at $\pm|y_{max}|$:

$$W(-|y_{max}|) = W(|y_{max}|) = 0, \tag{3.4}$$

$$\psi(-|y_{max}|) = \psi(|y_{max}|) = 0. \tag{3.5}$$

The value of y_{max} is chosen such as to satisfy the condition $|y_{max}| \gg |y_s|$. When this is satisfied the results of the computations do not depend significantly on the size of the system. The assumption of incompressibility is justified by using small flow at or near the resonant surfaces where the growth of the instability occurs. We will show later that it is the equilibrium shear flow in the vicinity of the resonant surfaces that determine the mode structure and growth. The values R_s are less than one in all the cases considered in this work. The values

of the flow at the computation boundaries are $0.57V_a$ for the simulation with $y_s = 0.75$, $y_{max} = 3.0$, and $0.34V_a$ for $y_s = 0.15$, $y_{max} = 1.0$ considered below.

3.3 Dispersion Relation

The double tearing dispersion relation is generalized here to accommodate equilibrium shear flow. Later the analytical growth rates will be compared with the numerical solutions of Eqs. (2.3)-(2.4) and thereby test the numerical procedures (see Fig. 3.3 in Sec. 3.4). In order to include the flow shear at the resonant surfaces and the viscosity for the general flow profiles, one has to follow the steps of Chen and Morrison (1990a, 1990b) with the boundary conditions and matching appropriate for two adjacent resonant surfaces. This substantially more complicated derivation is not the aim of the present work. Here, the simplifications arising from the centrally peaked, symmetric (with respect to $y = 0$) shear flow profile are used in the derivation. The growth rate of the instability is found from the linearized Fourier-transformed Eqs. (2.10)-(2.11) neglecting the viscous term and using the boundary layer approach. The physical domain is divided in to two types of regions; namely, an inner resistive region near $|y_s|$ in which $|F| \ll 1$, $|G| \ll 1$, where resistivity cannot be neglected in Ohm's law, and an ideal outer region in which the resistive term can be neglected and the ideal MHD equations are used. It is assumed that near the rational surfaces $\alpha^2 \ll \partial^2/\partial y^2$, and $F(y)$ is linearly expanded around y_s. It is further assumed for simplicity that the flow (3.2) can be approximated by

$$G(Ry) = \begin{cases} 0, & \text{if } |y| \le y_s, \\ G_0 = const. & \text{if } |y| > y_s. \end{cases} \tag{3.6}$$

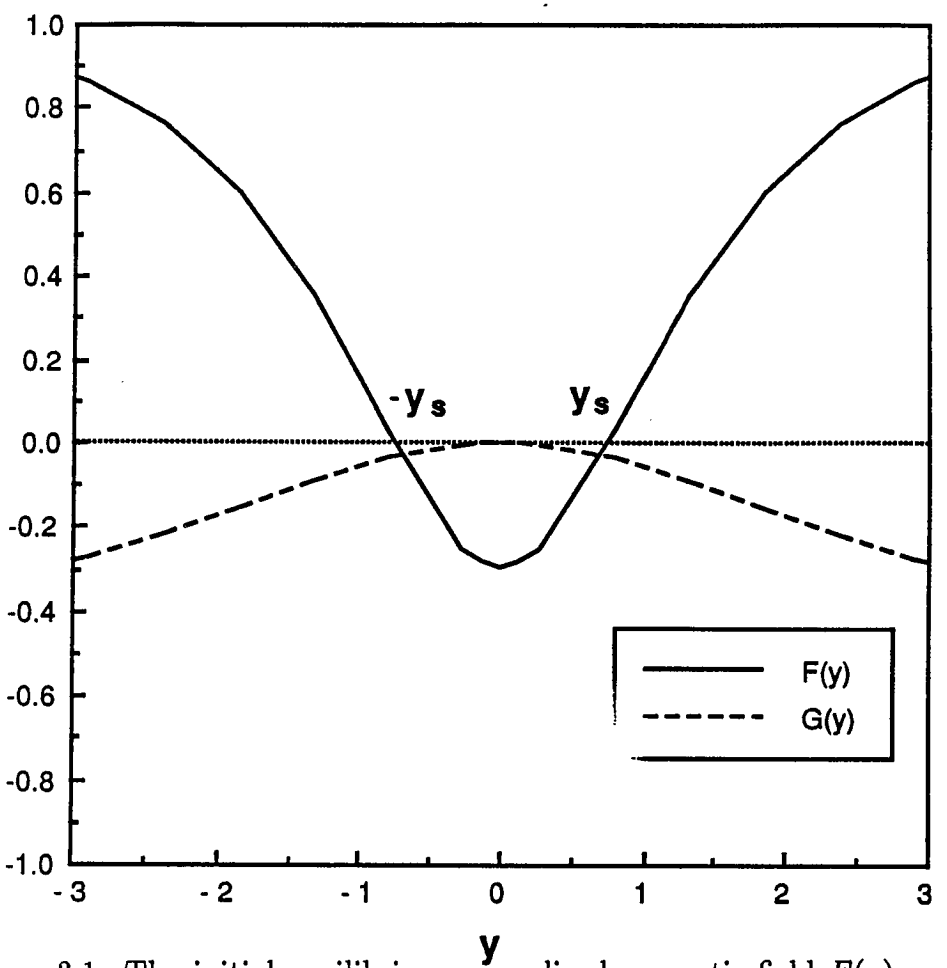

Figure 3.1: The initial equilibrium normalized magnetic field $F(y)$ and shear flow $G(y)$ given by Eqs. (3.1) and (3.2), respectively.
The parameters are $y_s = 0.75$, $R = 0.5$, $V = -0.5$, and $R_s = 0.132$.

Where G_0 is a measure of the flow in the outer region and is constant for a given flow profile. Next, since the flow shear is important near the tearing layers we match the outer region equations with constant flow G_0 to the inner region equations with $G(Ry) = 0$. This amounts to the incorporation of an effective flow shear in the solution. The value of G_0 is determined by

$$G'(Ry_s) \approx \frac{G_0 - G(0)}{Ry_s - 0} = \frac{G_0}{Ry_s} \tag{3.7}$$

and $G'(Ry_s)$ obtained from Eq. (3.2) is the flow shear at the tearing surfaces. Note, that in the limit $Ry_s \to 0$ the above expression (3.6) is exact, and that $|G_0| \approx R_s|F'(y_s)Ry_s|$. The inner resistive equations then become

$$\gamma\psi = \gamma F'(y_s)(y - y_s)\hat{w} + S^{-1}\psi'' \tag{3.8}$$

$$\gamma^2\hat{w}'' = -\alpha^2 F'(y_s)(y - y_s)\psi'' \tag{3.9}$$

where $\hat{w} = i\alpha W/\gamma$. In the ideal regions, the resistive term is neglected in Eq. (2.11), and the flow velocity is G_0, leading to

$$\psi = \frac{i\alpha FW}{\gamma + i\alpha G_0}, \tag{3.10}$$

which is then substituted into Eq. (2.10) to obtain

$$\frac{d}{dy}\left\{\left[(\gamma + i\alpha G_0)^2 + F^2\right]\frac{dw}{dy}\right\} = \alpha^2\left[(\gamma + i\alpha G_0)^2 + F^2\right]w, \tag{3.11}$$

where $w = i\alpha W/(\gamma + i\alpha G_0)$. The above non-resistive equation describes the double kink mode with flow in slab geometry. It is solved asymptotically in terms of a power series expansion with the boundary conditions

$$w(y) = \begin{cases} 0, & \text{if } |y| \gg y_s, \\ w_0 = const. & \text{if } |y| < y_s. \end{cases} \tag{3.12}$$

The form of Eqs. (3.8)-(3.11) is similar to those obtained in Pritchett *et al.* (1980) for the double tearing mode without flow. Following the procedure of Pritchett *et al.* we equate the solution of Eq. (3.11) near $|y_s|$ in the limit $[\alpha F'(y_s)(y-y_s)]/(\gamma + i\alpha G_0) \rightarrow -\infty$ to the external first-order solution. We thereby Doppler shift their solution and obtain the following growth rate γ_h of the double kink mode with flow

$$\gamma_h = -\frac{\pi\alpha^3}{F'(y_s)}\int_0^{y_s} F(y')^2 dy' - i\alpha G_0. \tag{3.13}$$

Finally, matching the external and internal solutions we use the dispersion relation with $G = 0$ of Pritchett *et al.*, which was derived in detail by Coppi *et al.* (1976), and obtain the double tearing dispersion relation corrected for shear flow

$$-\frac{\pi\alpha^3}{F'(y_s)}\int_0^{y_s} F(y')^2 dy' - i\alpha G_0 = 8b^{-3/2}\gamma^{-5/4}\frac{\Gamma\left(\frac{b\gamma^{3/2}+5}{4}\right)}{\Gamma\left(\frac{b\gamma^{3/2}-1}{4}\right)}, \tag{3.14}$$

where $b = \frac{S^{1/2}}{\alpha F'(y_s)}$ and Γ is the complex gamma function. When $G_0 = 0$, the results of the double tearing mode without flow are recovered in agreement with Pritchett *et al.* (see, Fig. 3.3). When $G_0 \neq 0$ Eq. (3.14) expands to the complex plane and exhibits much more complicated behavior than for $G_0 = 0$. The solution now can have more than one branch for a given parameter set. Therefore, one needs to place additional constrains on the solutions of Eq. (3.14) for the growth rate. Reasonable requirements are $\gamma_R > 0$, $\gamma_I \geq 0$ for growing overstable modes. It is interesting to note that the Doppler shift in the growth rate of the external Eq. (3.11) affects both the real and imaginary part of the growth rate in Eq.(3.14). Finally, the condition for small separation of singular surfaces (Pritchett *et al.*, 1980) that was used to select y_s in the numerical

calculations:

$$y_s < \alpha^{-7/9} S^{-1/9} \tag{3.15}$$

holds for the case with flow. In the following section the above analytic results are compared to the numerical calculations and are used as a guide for investigations in the parameter space of the double tearing mode.

3.4 Numerical Results

Since the method of solution is described in detail in Chapter 2, here only a brief discussion of relevant details is presented. The variable grid spacing used expands from a minimum of $\Delta y_{min} = 10^{-3}$ near the singular surfaces to $\Delta y_{max} = 0.5$ near the computational boundaries. When the computation domain, and S are small ($|y_{max}| \leq 2$, $S \leq 10^4$), a fixed grid with up to 500 grid points is used. The time step Δt is selected so that $\delta t \leq min(\gamma_R^{-1}, 0.2\gamma_I^{-1})$, and the simulation is evolved for N time steps until only the fastest growing modes are present in the solutions. The number of time steps required is usually in the range $100 < N < 500$. As in Chapter 2 the growth rates are obtained from the complex solutions in two steps. The real part of the growth rate γ_R is first found by fitting a straight line to the logarithm of the solutions. Next, the exponential growth is removed from the solutions and an FFT is performed on the remaining oscillatory part, which thereby determines the imaginary part of the growth rate γ_I. If the modes are purely growing, then only the first step in the above method is performed.

The results of the numerical computations are presented in Figs. 3.2–3.6. The spatial variations of the perturbed magnetic field ψ and the perturbed

flow W are shown in Fig. 3.2. In Fig. 3.2a the parameters are $S = 10^6$, $S_v = 10^9$, $\alpha = 0.5$, $V = -0.1$, and $R = 0.5$ (the value of R is not changed in Figs. 3.2–3.6). The separation y_s is large in Fig. 3.2a ($y_s = 0.75$) and small in Fig. 3.2b ($y_s = 0.15$). Note the rapid variation of W across the two tearing layers and the location of the sharp peaks that indicate the width of the resistive regions. It has been found that large viscosity reduces the sharpness of the peaks and widens the effective width of the resistive region ϵ; this effect is compatible with the single tearing mode scaling of the tearing layer width with the Reynolds number; i.e. $\epsilon \sim S_v^{-1/3}$ (see, Chen and Morrison, 1990b). Also, setting $y_{max} = 1.0$ for $y_s = 0.15$ and $y_{max} = 3.0$ for $y_s = 0.75$ the condition $|y_{max}| \gg y_s$ is satisfied, that is evident from the negligible values of the perturbations near the boundaries as compared to their values near the tearing layers. In Fig. 3.2b the separation $y_s = 0.15$ is small according to condition (3.15) thereby resulting in a nonconstant-ψ tearing mode that scales as $\gamma_R \sim S^{-1/3}$. For large flow, say $V = -0.5$ as in Fig. 3.2c, the double tearing mode is significantly different from that in Fig. 3.2b where $V = -0.1$. The effect of flow is evident in the external regions adjacent to the tearing layers where partial decoupling of the nonconstant-ψ tearing occurs and results in a lower growth rate.

Analytical and numerical growth rates and their dependence on R_s are presented in Fig. 3.3 with the parameters $S = 10^6$, $\alpha = 0.5$, and $y_s = 0.15$. When $R_s \leq 0.4$ the agreement of the growth rates is very good. For $R_s > 0.4$ both growth rates exhibit a decrease with R_s. The numerically obtained growth rate decrease at a higher rate with R_s than the growth rate obtained from the solution of Eq. (3.14), possibly due to the underestimation of the flow shear in

the approximations [Eqs. (3.6)-(3.7)] used to derive the dispersion relation. It has been found that the analytical dispersion relation yields a decrease in the growth rate when the shear is increased for both positive and negative values of G_0.

In Fig. 3.4 the dependence of the growth rate γ_R on the resistivity for $y_s = 0.15$ is shown. The top three curves are for $\alpha = 0.5$, and the bottom two curves are for $\alpha = 0.05$. The circles correspond to $V = -0.1$ ($R_s = 0.025$), the triangles to $V = -0.5$ ($R_s = 0.125$), and the squares to $V = -2.25$ ($R_s = 0.564$). When the rational surface separation is of the order of the resistive layer width, the growth of the double tearing mode is suppressed, while for small resistivity it scales as $\gamma_R \sim S^{-1/3}$, thus leading to the peaked behavior in Fig. 3.4. For $\alpha = 0.05$ and $V = -0.5$, the values of the growth rate are an order of magnitude smaller than those for $\alpha = 0.5$ and V=-0.5. When $\alpha = 0.05$ and $V = -2.25$ the growth rate decreases significantly with respect to the case where $\alpha = 0.05$ and $V = -0.5$. Thus the contribution of long wavelength perturbations to the growth of the double tearing mode is small. To summarize, the main result in Fig. 3.4 is that flow has a stabilizing effect on the growth rate for all calculated values of S and α, and the decrease of the growth rate with R_s is more significant when the resistive layer width is large compared to y_s.

In Fig. 3.5 we examine the dependence of the complex growth rate on the equilibrium shear flow at the resonant surfaces with $\alpha = 0.5$, $y_s = 0.15$, $S = 10^4$, and $y_s = 0.75$, $S = 10^6$. The numerical values of the shear flow at the resonant surfaces and the corresponding growth rates are presented in Table 3.1. When $y_s = 0.15$ and $S = 10^4$, the real part of the growth rate decreases by an

order of magnitude for $R_s = 0.752$, and $V = -3.0$, as compared to the case where $V = 0$, while the flow shear at the resonant surface is $G'(y_s) = \pm 0.11$. When $y_s = 0.75$ and $S = 10^6$, the real part of the growth rate decreases by an order of magnitude for $R_s = 0.237$ and $V = -0.9$ from its value for $V = 0$. In this case the flow shear was $G'(y_s) = \pm 0.15$. It is interesting to note that in both cases the same amount of suppression of the growth rate is achieved when the flow shear at the tearing layers is of the same order of magnitude, while the flow is an order of magnitude lower for the small y_s than that for the large y_s. The frequency of the temporal oscillations increases with V at a rate slower than that predicted from the linear Doppler shift for both small and large y_s. The oscillations dominate the behavior of the double tearing instability, in contrast to the single tearing mode with flow, where the imaginary part of the growth rate was always found to be considerably smaller than the real part. This is in part due to the non-zero flow at the tearing layers used in this model.

The effect of viscosity on the double tearing mode with $y_s = 0.75$, $S = 10^4$, and $\alpha = 0.5$ is examined in Fig. 3.6. Small viscosity does not significantly affect the growth rate. When $S_v \leq 10^2 \times S$ a simple scaling law behavior emerges. For $V = 0$ and $V = -0.1$ the scaling is $\gamma_R \sim S_v^{0.22}$, when $V = -0.5$ the double tearing mode approaches the standard tearing mode growth rate scaling with viscosity $\gamma_R \sim S_v^{1/6}$. This further indicates that large flow reduces the nonconstant effects and has a stabilizing effect. The imaginary part of the growth rate was found to be independent of viscosity, and it increases with V (see, Fig. 3.5).

Table 3.1: The values of the flow parameter V, the shear at the resonant surfaces R_s, and the growth rates for $y_s = 0.15$, $S = 10^4$, and $y_s = 0.75$, $S = 10^6$ with $R = 0.5$.

	$y_s = 0.15$			$y_s = 0.75$		
V	R_s	γ_R	γ_I	R_s	γ_R	γ_I
0.0	0.000	$4.15 \cdot 10^{-3}$	0.0	0.000	$1.69 \cdot 10^{-3}$	0.0
-0.1	0.025	$4.15 \cdot 10^{-3}$	$8.03 \cdot 10^{-5}$	0.026	$1.52 \cdot 10^{-3}$	$5.06 \cdot 10^{-4}$
-0.3	0.075	$3.92 \cdot 10^{-3}$	$1.65 \cdot 10^{-4}$	0.079	$8.39 \cdot 10^{-4}$	$1.26 \cdot 10^{-3}$
-0.5	0.125	$3.73 \cdot 10^{-3}$	$2.77 \cdot 10^{-4}$	0.132	$4.66 \cdot 10^{-4}$	$1.72 \cdot 10^{-3}$
-0.8	0.201	$3.41 \cdot 10^{-3}$	$4.00 \cdot 10^{-4}$	0.211	$2.10 \cdot 10^{-4}$	$1.96 \cdot 10^{-3}$
-1.0	0.251	$3.14 \cdot 10^{-3}$	$4.94 \cdot 10^{-4}$	0.263	$1.34 \cdot 10^{-4}$	$2.07 \cdot 10^{-3}$
-2.0	0.501	$1.67 \cdot 10^{-3}$	$8.09 \cdot 10^{-4}$			
-2.6	0.652	$7.84 \cdot 10^{-4}$	$9.29 \cdot 10^{-4}$			
-3.0	0.752	$2.41 \cdot 10^{-4}$	$9.89 \cdot 10^{-4}$			

3.5 Summary and Discussion

We have investigated the double tearing mode instability with shear flow by numerically solving the resistive MHD equations with equilibrium magnetic field and shear flow. Comparison with the linear dispersion relation was made. The enhancement of the growth rate due to nonconstant-ψ effects in the double tearing mode without flow is reduced by the presence of significantly large shear flow at the tearing layers ($R_s < 0.8$). A stabilizing effect was found for both large and small surface separation. Shear flow induces temporal oscillations of the perturbed quantities, and the frequency of the oscillations increases with V at a rate lower than that expected from a simple Doppler shift of the frequency. Overstable modes were found from the analytical dispersion relation, and their values are in good agreement with those obtained numerically. We have also calculated several cases with a flow profile that has an odd dependence on y [i.e., $G = V\tanh(Ry)$] and found that for small V and R that the flow has a stabilizing effect comparable to that obtained with (3.2), but for larger V or R (such as $R_s > 1$) and with the magnetic field profile (3.1) the double tearing mode was further destabilized by the K-H instability.

The effect of viscosity on the double tearing mode was also investigated numerically. When $S_v \gg 10^2 \times S$ the viscosity had no significant affect on the growth rate. When $S_v \leq 10^2 \times S$, it had a stabilizing affect, and the growth rate exhibited a power law dependence on S_v. In the presence of large flow the growth rate scaling with viscosity approximates that of the standard tearing mode scaling, namely, $\gamma_R \sim S_v^{1/6}$, and γ_I is independent of viscosity.

Double tearing instability with flow exhibits a complicated behavior in the physical and parameter space, and is significantly modified by the pres-

ence of shear flow. The main result of the present work is that equilibrium shear flow has a stabilizing effect on the double tearing instability. As a result, fusion devices with non-monotonic current profiles and equilibrium shear flows may be less unstable than those with monotonic current profiles that are subject to the development of the usual single tearing mode. Suggestions that the double tearing mode may explain the fast evolution times of solar flares must be re-examined when shear flow is present due to its stabilizing effect, as demonstrated in this chapter.

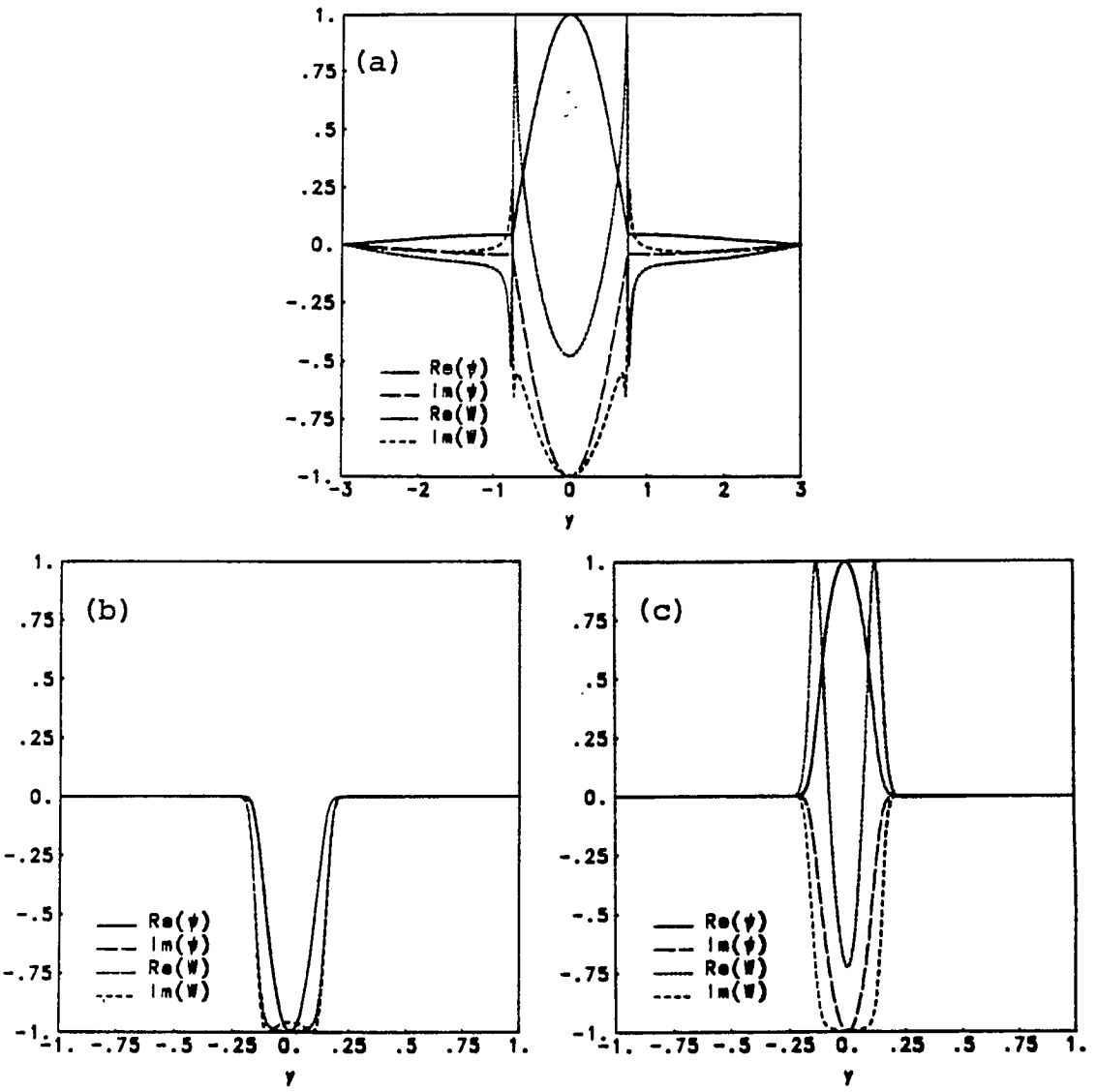

Figure 3.2: The spatial dependence of the complex perturbed magnetic field ψ and flow W.
(a) The parameters are $S = 10^6$, $\alpha = 0.5$, $y_s = 0.75$, $V = -0.1$, $S_v = 10^9$, and $R_s = 0.026$. (b) Same as (a), but with $y_s = 0.15$, and $R_s = 0.025$. (c) Same as (b) except $S = 10^4$, $\alpha = 0.5$, $V = -0.5$, and $R_s = 0.125$.

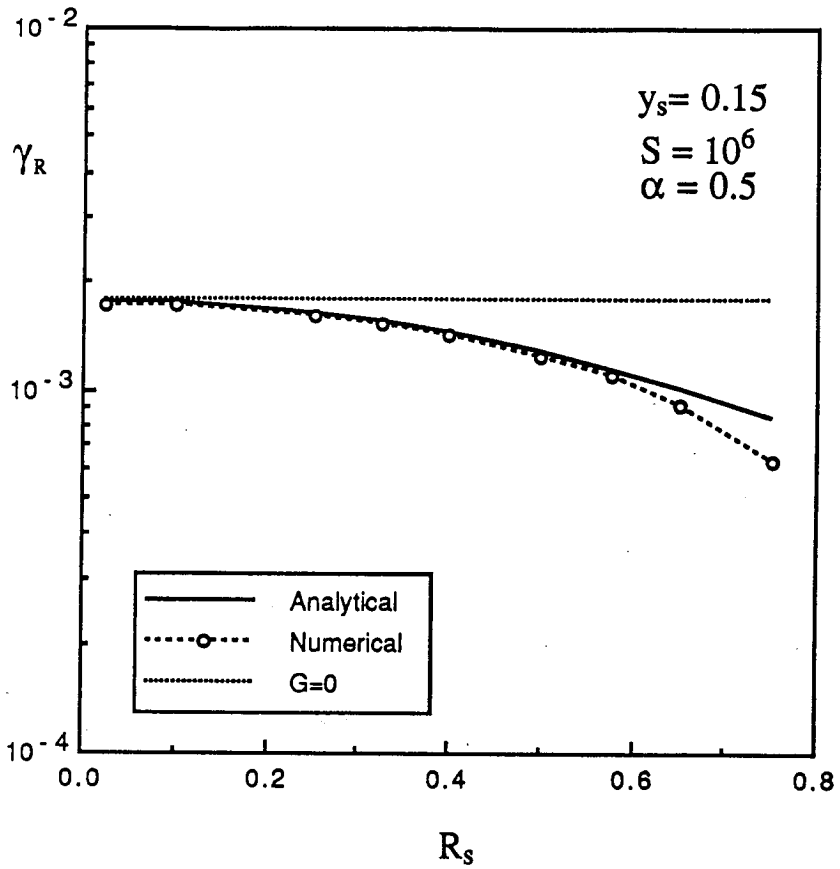

Figure 3.3: Growth rate dependence on R_s
The growth rates obtained from Eq. (3.14) (solid curve) are compared with the growth rates obtained from the numerical MHD simulations (empty circles). The parameters are $R = 0.5$, $y_s = 0.15$, $S = 10^6$, and $\alpha = 0.5$. The value of the growth rate with $G = 0$ is shown (dotted line).

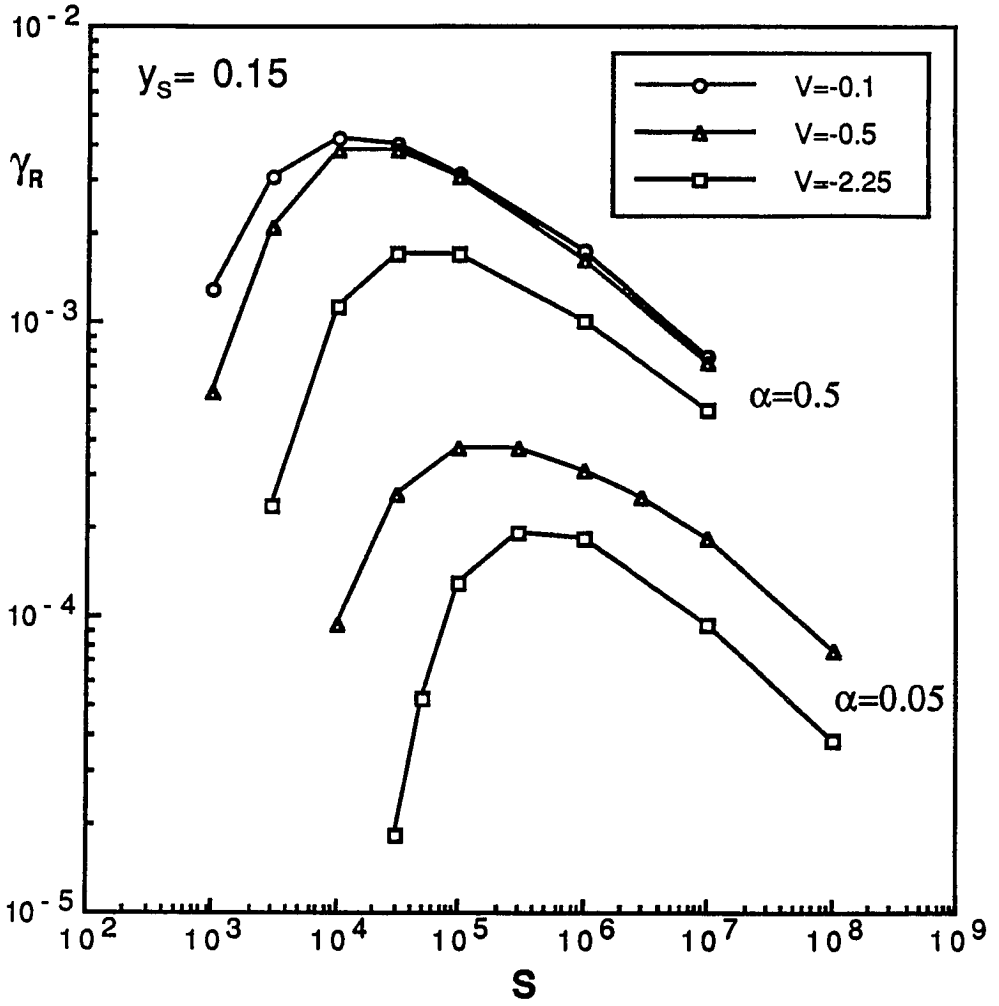

Figure 3.4: Growth rate dependence on S.
The parameters are $y_s = 0.15$, $\alpha = 0.5$ (top three curves), and $\alpha = 0.05$ (bottom two curves) with $V = -0.1$, $R_s = 0.025$ (circles), $V = -0.5$, $R_s = 0.125$ (triangles), and $V = -2.25$, $R_s = 0.564$ (squares).

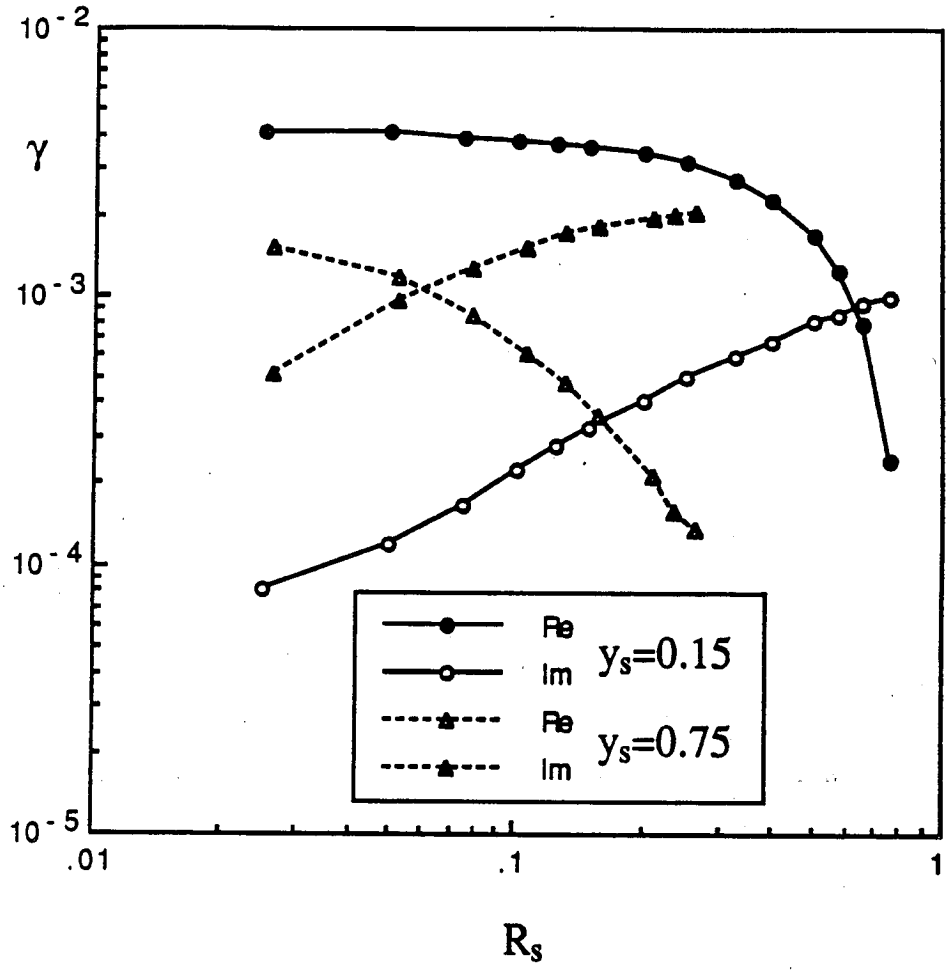

Figure 3.5: The dependence of the complex growth rate γ on the shear parameter R_s.
The parameters are $y_s = 0.75$, $S = 10^6$, (circles), and $y_s = 0.15$, $S = 10^4$ (squares) with $\alpha = 0.5$, $R = 0.5$.

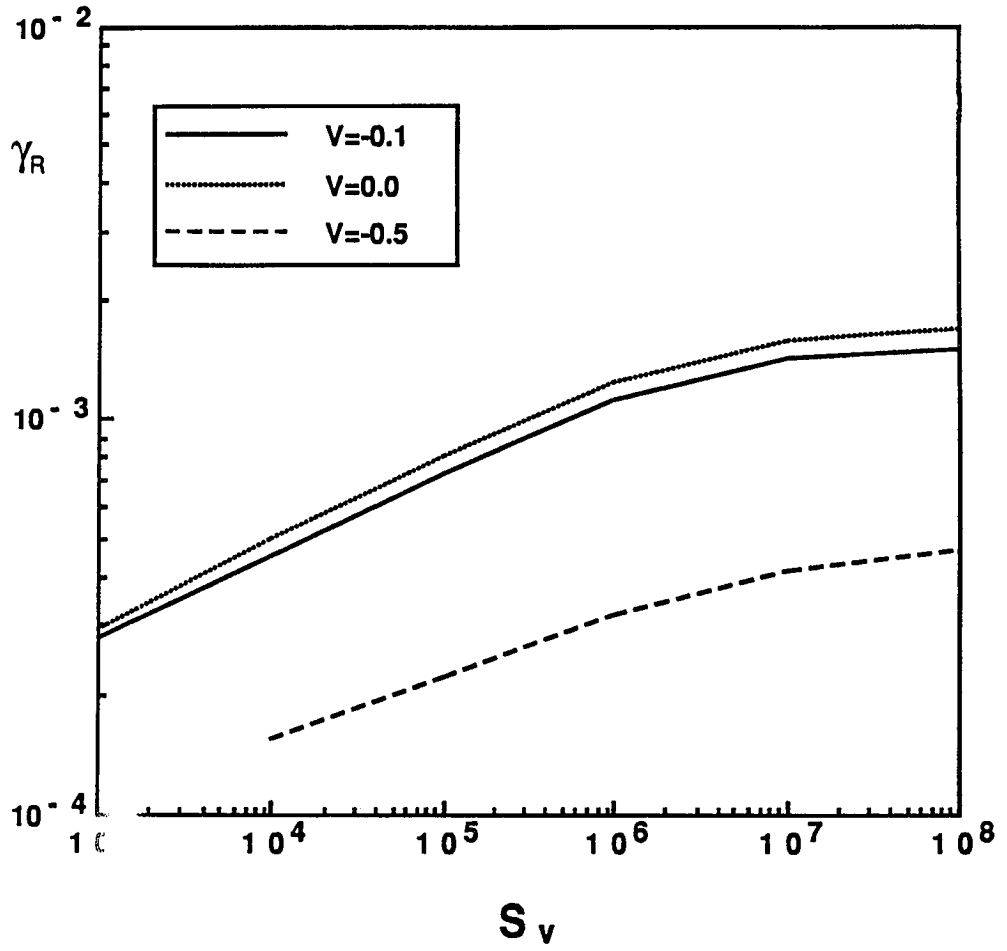

Figure 3.6: Growth rate scaling with viscosity parameter S_v.
The parameters are $y_s = 0.75$, $S = 10^4$, $\alpha = 0.5$, $V = 0$ (dotted curve), $V = -0.1$ and $R_s = 0.026$ (solid curve), $V = -0.5$ and $R_s = 0.079$ (dashed curve).

Chapter 4

Nonlinear Evolution of the Tearing Mode with Equilibrium Shear Flow

4.1 Introduction

Nonlinear saturation of the tearing mode occurs within one or several growth times and the growth slows down from exponential to algebraic (Rutherford, 1973). Numerical evolution of the nonlinear tearing mode (without flow) in slab geometry was studied by Schnack (1977), and Schnack and Killeen (1979) using the finite difference alternative direction implicit (ADI) approach. The energetics, growth rate and spatial behavior for several values of resistivity and for both constant-ψ and nonconstant-ψ regimes were investigated by Steinolfson and Van Hoven (1984). The effect of plasma rotation on the nonlinear tearing mode was considered recently by Persson and Bondeson (1990), and Persson (1991). They solved the reduced MHD equations with the spectral approach, and found that when flow is sufficiently strong, the viscosity sufficiently small, and the $m = 2/n = 1$, $m = 4/n = 2$ modes are present, the nonlinear evolution of the tearing mode can lead to nonlinear oscillatory behavior. These nonlinear oscillations were obtained analytically by Chen and Morrison (1991) using center manifold reduction.

In Chapter 2 we studied the linear evolution of the tearing mode with equilibrium shear flow parallel to the magnetic field. Here, the nonlinear evolution of the tearing mode is investigated numerically via solution of

the incompressible two-dimensional resistive MHD equations in slab geometry using the finite difference ADI method. We find that the presence of equilibrium shear flow can reduce magnetic energy release, increase the saturation time, and can affect the topology of the field and currents generated by the instability.

This chapter is organized as follows: In Sec. 4.2 the nonlinear MHD equations in slab geometry, the initial magnetic field configuration, the equilibrium flow profiles and the relevant conservation relations are presented. In Sec. 4.3 the numerical method of solution is presented. Section 4.4 is devoted to the numerical results, and a summary is given in Sec. 4.5.

4.2 MHD Equations

We use the MHD model presented in Chapter 1, and choose the 2-D equilibrium magnetic and velocity fields to be of the form:

$$\mathbf{B} = B_0(y)\mathbf{e_x} + \nabla_\perp \psi \times \mathbf{e_z} \equiv \nabla_\perp \Psi \times \mathbf{e_z} \tag{4.1}$$

$$\mathbf{V} = V_0(y)\mathbf{e_x} + \nabla_\perp \phi \times \mathbf{e_z} \equiv \nabla_\perp \Phi \times \mathbf{e_z}, \tag{4.2}$$

where Ψ and Φ are the total flux and stream functions, and ψ, ϕ are the flux and stream functions relative to the equilibrium quantities B_0 and V_0.

Substituting Eqs. (4.1) and (4.2) in Eqs. (1.1)–(1.4), taking the curl of Eq. (1.1), thus eliminating the pressure P, and considering the $\mathbf{e}_x$ and $\mathbf{e_y}$ components in dimensionless form, gives the following 2-D MHD equations

$$\frac{\partial \psi}{\partial t} = -\left(\frac{\partial \phi}{\partial y} + G\right)\frac{\partial \psi}{\partial x} + \left(\frac{\partial \psi}{\partial y} + F\right)\frac{\partial \phi}{\partial x} + \frac{1}{S}\nabla_\perp^2 \psi \tag{4.3}$$

$$\frac{\partial(\nabla_\perp^2\phi)}{\partial t} = -\left(\frac{\partial\phi}{\partial y}+G\right)\frac{\partial(\nabla_\perp^2\phi)}{\partial x}+\frac{\partial\phi}{\partial x}\left[\frac{d^2G}{dy^2}+\frac{\partial(\nabla_\perp^2\phi)}{\partial y}\right]+$$

$$+\left(\frac{\partial\psi}{\partial y}+F\right)\frac{\partial(\nabla_\perp^2\psi)}{\partial x}-\frac{\partial\psi}{\partial x}\left[\frac{d^2F}{dy^2}+\frac{\partial(\nabla_\perp^2\psi)}{\partial y}\right]+\frac{1}{S_v}\nabla_\perp^4\phi, \qquad (4.4)$$

where $\nabla_\perp^2 \equiv \frac{\partial^2}{\partial x^2}+\frac{\partial^2}{\partial y^2}$ and $\frac{\partial}{\partial z}=0$. We have also assumed that the equilibrium magnetic field is maintained by an external electric field and we imagine that a similar agent maintains the equilibrium flow. The coordinates are referenced to the magnetic shear length scale a_b, the time to the Alfvén time τ_h, magnetic field to $B = |\mathbf{B}_0(y_{max})|$, where y_{max} is the distance from the tearing layer to the y-boundary.

Resistive reconnection of the B_y component of the magnetic field across the tearing layer is measured by the change in the magnetic flux across $y=0$

$$\Delta\hat{\Phi}(t) \equiv \int_0^{x_{\max}}\left|\frac{\partial}{\partial x'}\psi(x',0,t)\right|dx' \ , \qquad (4.5)$$

where $x_{\max}$ is one period for the periodic boundary conditions. The nonlinear growth rate p is given by

$$p = \frac{\partial}{\partial t}\Delta\Phi(t) \ . \qquad (4.6)$$

The growth rate calculated from Eq. (4.6) agrees with that for linear tearing (when the instability is in the linear regime) for both $V=0$ (Steinolfson and Van Hoven 1984) and $V\neq 0$ (Ofman *et al.*, 1991). Additional relevant quantities are the changes of the magnetic and kinetic energies relative to the equilibrium values ; i.e.

$$\Delta E_M(t) = \int_{y_{\min}}^{y_{\max}}\int_0^{x_{\max}}\left[\left(F+\frac{\partial\psi}{\partial y}\right)^2+\left(\frac{\partial\psi}{\partial x}\right)^2-F^2\right]dx\,dy \qquad (4.7)$$

$$\Delta E_K(t) = \int_{y_{\min}}^{y_{\max}} \int_0^{x_{\max}} \left[\left(G + \frac{\partial \psi}{\partial y} \right)^2 + \left(\frac{\partial \phi}{\partial x} \right)^2 - G^2 \right] dx\, dy. \quad (4.8)$$

The total energy is given by

$$E_{\text{tot}}(t) = \Delta E_M(t) + \Delta E_K(t) + E_{M0} + E_{K0}, \quad (4.9)$$

where E_{M0} and E_{K0} are the initial magnetic and kinetic energies stored in the equilibrium shear flow and magnetic field. Because of resistive and viscous dissipation E_{tot} satisfies

$$\frac{dE_{\text{tot}}}{dt} = 2 \int_{y_{\min}}^{y_{\max}} \int_0^{x_{\max}} \left[-\frac{J}{S} (J - F') - \frac{1}{S_v} \omega(\omega - G') \right], \quad (4.10)$$

where $J = -\nabla^2 \psi$ is the nonequilibrium current in the z-direction, and $\omega = -\nabla^2 \phi$ is the nonequilibrium vorticity. The resistive dissipation of the magnetic helicity, which is given by

$$\frac{d}{dt} \int_{y_{\min}}^{y_{\max}} \int_0^{x_{\max}} \psi\, dx\, dy = -\frac{1}{S} \int_{y_{\min}}^{y_{\max}} \int_0^{x_{\max}} J\, dx\, dy, \quad (4.11)$$

is also of interest. Equations (4.10) and (4.11) are valid for the periodic x and zero y boundary conditions and are used as a means of estimating the quality of the numerical solutions by comparing the calculated values of the r.h.s and the l.h.s of the equations. Equation (4.10) is also used to estimate the effective viscous dissipation that arises in the numerical solution of the MHD equations.

4.3 Method of Solution

We initiate the nonlinear computations with the solutions of the linearized Eqs. (2.4) and (2.3) (see, Chapter 2). The amplitude factors of the linearized growing solutions are chosen so that the nonlinear terms as calculated from the linear ϕ and ψ, are important. This procedure insures that the

nonlinear code is initiated at an amplitude where the subsequent evolution of the mode is in the nonlinear regime (Steinolfson and Van Hoven, 1984). In this study the normalized spatial wavenumber $\alpha = 2\pi/\lambda$ was 0.5, which implies that the size of the longest wavelength λ in the x-direction is 4π in units of a_b. As mentioned, the alternating direction implicit (ADI) finite-difference technique was used to obtain the nonlinear evolution. The solutions are first advanced one half time step in the x-direction using the initial linear solutions. Next, the solutions are advanced another half time step in the y-direction using the finite difference results in the x-direction from the previous half time step. This procedure for a single time step is repeated until the full temporal evolution is obtained. In the x-direction the finite difference form of Eqs. (4.3) and (4.4) is given by the following:

$$\frac{2}{\Delta t}\psi_{i,j}^{n+1/2} + G_j\delta_x\psi_{i,j}^{n+1/2} - F_j\delta_x\phi_{i,j}^{n+1/2} + \delta_x\psi_{i,j}^{n+1/2}\delta_y\phi_{i,j}^{n} - \delta_y\psi_{i,j}^{n}$$

$$-\delta_y\psi_{i,j}^{n}\delta_x\phi_{i,j}^{n+1/2} = \frac{2}{\Delta t}\psi_{i,j}^{n} - \frac{1}{S}J_{i,j} \qquad (4.12)$$

$$\frac{2}{\Delta t}\omega_{i,j}^{n+1/2} + \left(\delta_y\phi_{i,j}^{n} + G_j\right)\delta_x\omega_{i,j}^{n+1/2} - \left(G_j'' - \delta_y\omega_{i,j}^{n}\right)\delta_x\phi_{i,j}^{n+1/2}$$

$$+\left(\delta_y\psi_{i,j}^{n} + F_j\right)\delta_x J_{i,j}^{n+1/2} + \left(F_j'' - \delta_y J_{i,j}^{n}\right)\delta_x\psi_{i,j}^{n+1/2} =$$

$$= \frac{2}{\Delta t}\omega_{i,j}^{n} + \frac{1}{S_v}\left(\delta_x^2 + \delta_y^2\right)\omega_{i,j}^{n}, \qquad (4.13)$$

where $\Delta t = t_{n+1} - t_n$, and

$$J_{i,j}^{n} = -\left(\delta_x^2 + \delta_y^2\right)\psi_{i,j}^{n}, \quad \omega_{i,j}^{n} = -\left(\delta_x^2 + \delta_y^2\right)\phi_{i,j}^{n}\ .$$

The grid spacing in the x-direction is uniform, thus the finite differences are given by

$$\delta_x\psi_{i,j}^{n} = \frac{\psi_{i+1,j}^{n} - \psi_{i-1,j}^{n}}{2\Delta x}\ , \quad \delta_x^2\psi_{i,j}^{n} = \frac{\psi_{i+1,j}^{n} - 2\psi_{i,j}^{n} + \psi_{i-1,j}^{n}}{(\Delta x)^2},$$

where $\Delta x = \frac{1}{2}(x_{i+1} - x_{i-1})$, while in the y-direction

$$\delta_y \psi^n_{i,j} = \frac{1}{2}\left(\frac{\psi^n_{i,j+1} - \psi^n_{i,j}}{y_{j+1} - y_j} + \frac{\psi^n_{i,j} - \psi^n_{i,j-1}}{y_j - y_{j-1}}\right),$$

$$\delta^2_y \psi^n_{i,j} = \frac{1}{y_{j+1} - y_{j-1}}\left(\frac{\psi^n_{i,j+1} - \psi^n_{i,j}}{y_{j+1} - y_j} - \frac{\psi^n_{i,j} - \psi^n_{i,j-1}}{y_j - y_{j-1}}\right).$$

The variable grid spacing $\Delta y_j = y_{j+1} - y_j$ expands from a minimum of $\Delta y_{\min} = 10^{-3}$ at the tearing layer to $\Delta y_{\max} = 0.5$ near the computational boundaries according to the prescription

$$\Delta y_j = \Delta y_{\max}\left(\frac{\Delta y_{\min}}{\Delta y_{\max}}\right)^{(j_{\max}-j)/(j_{\max}-1)}, \tag{4.14}$$

where $j_{\max}$ denotes the boundary grid point. Up to 200 grid points in the y-direction, and up to 64 grid points in the x-direction were used. Constant grid spacing in the y-direction was also used for low S values. Fourth order smoothing (Strauss, 1978) was applied to the solutions away from the tearing layer. Equations (4.12)-(4.13) are written in tridiagonal form

$$-A^n_i\, U^{n+1/2}_{i+1,j} + B^n_i\, U^{n+1/2}_{i,j} - C^n_i\, U^{n+1/2}_{i-1,j} = D^n_{i,j}, \tag{4.15}$$

where A, B, C are 2 by 2 matrices, and U, and D are two-dimensional vectors. Equation (4.15) is solved for U using Gaussian elimination. For the next half time step $n \to n + 1/2$ and $n + 1/2 \to n + 1$ in the above Eqs. (4.15), and the solutions are advanced one time step. The boundary conditions are $\psi(y = \pm y_{\max}) = 0$, $\phi(y = \pm y_{\max}) = 0$, where $y_{\max}$ is the distance to the boundary from the tearing layer, and both ψ and ϕ are periodic in the x-direction. Due to the presence of the symmetry breaking equilibrium shear flow one cannot use the simplifying symmetry assumptions that enable the solutions of the MHD equations to be computed in one quarter of the present domain (Steinolfson and

Van Hoven, 1984). Also, to impose the periodic boundary conditions requires three passes through the mesh for each integration in the x-direction (Schnack, 1977). Only two passes through the mesh are necessary in the non periodic y-direction.

For a fully implicit scheme the time step Δt is limited to the size of Δx; i.e., $\Delta t < \Delta x$ (Pritchett *et al.*, 1980). In our case the terms higher than second order are treated explicitly, and it has been found that the relation $\Delta t < \Delta x/2$ gives satisfactory results. When nonconstant grid spacing is used, Δx is one or several orders of magnitude larger than Δy across the tearing layer. Reasonable computation times on the Cray II for S as large as 10^6 are possible with this technique. A typical run with $S = 10^4$ takes about 1/2 hour of CPU time.

4.4 Numerical Results

In Figs. 4.1–4.15 we examine the spatial structure and the temporal evolution of the nonlinear tearing mode with flow. In these runs the parameters were $S = 10^2, 10^4, 10^5, R = 0.73, \alpha = 0.5$, and the flow parameter was $V = 0$, 0.1, 0.2, 0.3, 0.5 for the tanh profile, while $V = 0.1, 0.5$ for the sech flow profile.

The spatial variations of ψ, ϕ, Ψ, Φ, and the current $J_T = J - F'$ after two resistive times, normalized to their respective maximal values are shown in Figs. 4.1–4.9. In Figs. 4.1–4.2 the equilibrium shear flow is the tanh velocity profile, with $V = 0.1$ and $V = 0.2$. In Figs. 4.3–4.4 the equilibrium shear flow is the sech velocity profile with $V = 0.1$ and $V = 0.5$. The other parameters are $S = 10^2$, $R = 0.73$, and $\alpha = 0.5$. When $V = 0$, ψ is symmetric with respect to the x and y axes, while ϕ is anti-symmetric in both the linear and nonlinear

regimes. When flow is present this symmetry is broken and the perturbations align themselves with the equilibrium flow, namely, in Fig. 4.1, ψ and ϕ deform in opposite directions with respect to the x axis and the distortion away from the tearing layer increases with V. Similar alignment with the flow occurs for the sech equilibrium in Figs. 4.3–4.4, but for larger V the values of ψ and ϕ are distorted more near the tearing layer (where the shear is zero) than away from it, in agreement with the stabilizing effect of higher shear regions (see, Fig. 2.1) as expected from the linear theory (see, Chen and Morrison, 1990).

The contour lines of the total flux and stream functions for the tanh flow profile at $t = 200\tau_h$, with $V = 0.5$ and $S = 100$ are shown in Fig. 4.5. The velocity and the magnetic field lines are parallel to the contours of Ψ and Φ. The magnetic field lines exhibit the saturated island structure, where the island width is an order of magnitude larger than the tearing layer width ϵ. Similar island structures appear in the contour plot of Φ. The appearance of the stream function is different from the standard FKR case due to the presence of the equilibrium shear flow. Note that the x-point in the center of contour plot of Φ is distorted in agreement with the structure of ϕ in Fig. 4.2 and small distortion of the magnetic x-point appears in the contour plot of Ψ. We present the low resistivity solutions with $S = 10^4$, $V = 0.1$, and the sech flow profile at $t = 2000\tau_h$ in Figs. 4.6–4.7. In Fig. 4.6 contours of Ψ and Φ are shown, while in Fig. 4.7 displays the contours of ψ and ϕ. The saturated magnetic island structure is evident in the contours of Ψ . The width of the islands is an order of magnitude larger than the width of the tearing layer. For $S = 10^4$ both the tearing layer width and the island width are smaller than for $S = 10^2$ as expected from the linear ϵ scaling with resistivity. The appearance of sharp

features along the y axis indicates the narrow tearing layer. It is interesting to compare the contours of ψ in Fig. 4.7 to the contours of ψ in Fig. 4.3. In both figures similar sharp features form along the y axis, indicating that the tearing layer is narrow compared to the high resistivity, low shear flow cases. In Fig. 4.7 this is due to the low resistivity ($S = 10^4$ with $V = 0.1$), while in Fig. 4.3 this is due to the high shear flow ($V = 0.5$ with $S = 10^2$). For the sech profile the flow near the y axis is small compared to the flow away from the y axis, and thus the contour of Φ shows a relatively flat region of width a_b along the y axis, where ϕ and its vortices are dominant. The effect of the narrow boundary layer is clearly seen in Fig. 4.7.

The current J_T for $V = 0$ and $V = 0.3$ (tanh velocity profile) is shown in Fig. 4.8. When $V = 0$ the current is symmetric with respect to the x and y axes, its maximum $J_{T\mathbf{max}}$ occurs near the center of the slab, and it points in the negative z-direction. When $V = 0.3$ the current has a more complicated two-dimensional structure, again aligned with the equilibrium flow. Additional regions of significant current appear far from the tearing layer, around $y = \pm 2.5$ with $|J_T(x, 2.5)/J_{T\mathbf{max}}| \sim 0.2$, thus the flow generates significant currents in the external regions of the tearing mode.

We initiate the nonlinear evolution with a single linear mode in the x-direction. Its wavelength, and hence the size of the computational domain in the x-direction, is determined by the value of α. In Fig. 4.9 the solutions ψ and ϕ for the tanh profile with $V = 0.3$ are plotted as functions of x for $y = 0.5$. A single mode corresponding to $\alpha = 0.5$ ($x_{\mathbf{max}} = 2\pi/\alpha = 4\pi$) is present, and the phase shift between ψ and ϕ is caused by the equilibrium flow. Detailed treatments of the linear tearing mode with flow are given in Einaudi

and Rubini (1990), and Ofman *et al.* (1991).

Figure 4.10 depicts the temporal evolution of the growth rate, the reconnected flux and the perturbed magnetic, kinetic, and total energies for eight resistive times ($800\tau_h$) with $V = 0.1$, the tanh flow profile, and $S = 10^2$. In Fig. 4.10a we present the temporal evolution of the growth rate (curve A) and the reconnected flux (curve B). Initially the growth rate calculated from Eq. (4.6) corresponds to the linear growth calculated directly from the exponential growth of the solutions (Ofman *et al.*, 1991), and the reconnected flux grows exponentially with time. After $10\tau_h$ the growth rate drops considerably and the reconnected flux grows linearly with time as expected in Rutherford regime (Rutherford, 1973). After another $100\tau_h$ the growth of the reconnected flux slows to less than the linear rate and after $400\tau_h$ the mode saturates completely and the amount of the reconnected flux remains practically constant with time. The growth rate continues to decrease at an exponential rate.

In Fig. 4.10b curve A represents the change of the magnetic energy in the x component of the magnetic field ΔE_{Mx}, (defined by setting $\partial\psi/\partial x = 0$ in Eq. (4.7) while curve B represents the change of the magnetic energy in the y component, ΔE_{My} (defined by $\Delta E_M = \Delta E_{Mx} + \Delta E_{My}$). Curve C corresponds to the total change of the magnetic and kinetic energies $\Delta E_{\rm tot} \equiv \Delta E_m + \Delta E_k$. All these quantities are presented on a log scale, thus their absolute values are shown — ΔE_{Mx} and $\Delta E_{\rm tot}$ are negative for most of the evolution time indicating energy loss. The changes of sign of $\Delta E_{\rm tot}$ and ΔE_{Mx} appear as sharp minima at $t \approx 5$ and $t \approx 30$, respectively. Most of the transfer of energy occurs from the x component of the magnetic field to the y component (curve B) and to resistive dissipation. A small fraction of ΔE_{My} is transferred to

the kinetic energies (see Table 4.1). The change of the kinetic energies ΔE_K in Fig. 4.10c is initially comparable in magnitude (but opposite in sign) to ΔE_M, but after about one resistive time ΔE_{Kx} saturates at values an order of magnitude smaller than ΔE_M, and the transition from exponential to linear growth occurs in a time $t < 100\tau_h$, when ΔE_{Ky} is an order of magnitude smaller than ΔE_{Kx}.

In Fig. 4.11 we compare the change in the magnetic and total energies for the cases $V = 0.2$ and $V = 0.3$ with $S = 10^2$. For $V = 0.3$ the rate of change of the energies is initially ($t < 100\tau_h$) lower than for $V = 0.2$, but after the growth saturates the changes occur at similar rates. The initial wiggling of the total energy is due to transient effects that arise when the nonlinear code is initiated with the linear solutions. The total energy release of the tearing mode with $V = 0.3$ is only 60% of the energy released when $V = 0.2$. This decrease of energy release with increasing V is a trend seen in all runs as evidenced in Table 4.1.

The case where $S = 10^4$, $V = 0.5$, with the tanh equilibrium flow profile is presented in Fig. 4.11 up to a time $2000\tau_h$. The temporal behavior of the $S = 10^4$ case is similar to the $S = 10^2$ case, but as expected from the lower resistivity, proceeds on a longer time scale. The absolute values of the magnetic and total energy changes are shown in Fig. 4.12a. Note, that the change of sign of E_{tot} (curve C) occurs at $\sim 700\tau_h$ that is about an order of magnitude smaller than for $S = 10^2$. This is consistent with the linear growth rate scaling of $S^{-1/2}$ for the tearing mode with flow. In Fig. 4.12b total energy dissipation (curve A) is compared to the resistive dissipation (curve B). Due to an initial transient instability the total energy dissipation exhibits rapid oscillations that

Table 4.1: The change in the magnetic, kinetic, and total energies.

V	ΔE_{Mx}	ΔE_{My}	ΔE_{Kx}	ΔE_{Ky}	ΔE_{tot}
$S = 10^2$, $t = 200\tau_h$					
0.0	-0.792	0.488	$0.94 \cdot 10^{-2}$	$0.73 \cdot 10^{-3}$	-0.294
tanh flow profile					
0.1	-0.482	0.305	$1.24 \cdot 10^{-2}$	$2.71 \cdot 10^{-3}$	-0.162
0.2	-0.296	0.189	$1.76 \cdot 10^{-2}$	$5.71 \cdot 10^{-3}$	$-8.37 \cdot 10^{-2}$
0.3	-0.237	0.153	$2.58 \cdot 10^{-2}$	$9.86 \cdot 10^{-3}$	$-4.83 \cdot 10^{-2}$
$S = 10^4$, $t = 2000\tau_h$					
0.0	$-9.11 \cdot 10^{-2}$	$4.38 \cdot 10^{-2}$	$1.44 \cdot 10^{-5}$	$4.74 \cdot 10^{-7}$	$-4.73 \cdot 10^{-2}$
tanh flow profile					
0.1	$-4.46 \cdot 10^{-2}$	$2.12 \cdot 10^{-2}$	$0.22 \cdot 10^{-3}$	$0.16 \cdot 10^{-3}$	$-2.30 \cdot 10^{-2}$
0.5	$-2.08 \cdot 10^{-2}$	$0.88 \cdot 10^{-2}$	$2.02 \cdot 10^{-3}$	$1.51 \cdot 10^{-3}$	$-8.47 \cdot 10^{-3}$
sech flow profile					
0.1	$-3.25 \cdot 10^{-2}$	$1.53 \cdot 10^{-2}$	$5.50 \cdot 10^{-5}$	$2.45 \cdot 10^{-5}$	$-1.72 \cdot 10^{-2}$
0.5	$-1.15 \cdot 10^{-2}$	$5.43 \cdot 10^{-3}$	$4.07 \cdot 10^{-4}$	$9.64 \cdot 10^{-5}$	$-5.59 \cdot 10^{-3}$

decay within several hundred Alfvén times, and the evolution proceeds with the resistive dissipation being significantly larger than the dissipation due to numerical viscosity. The quantities ΔE_{Kx} and ΔE_{Ky} are shown in Fig. 4.12c. The initial exponential growth slows down after only $500\tau_h$ and the nonlinear saturation is evident. The change in the kinetic energies after $1000\tau_h$ is an order of magnitude lower than the change in the magnetic energies in Fig. 4.12a, thus the energy release is dominated by resistive effects. Nonlinear saturation of the growth rate (curve A) and the reconnected flux (curve B) are presented in Fig. 4.12d. The growth rate defined in Eq. (4.6) decreases by a factor of 2 after $2000\tau_h$ and the slower than exponential growth of the reconnected flux is evident after $500\tau_h$. This is consistent with the nonlinear saturation of the energies in Figs. 4.12a and 4.12b.

In Fig. 4.13 we present the temporal evolution of the energies for $S = 10^5$, $V = 0.5$ and the tanh flow profile. In Fig. 4.13a the initial ΔE_{Mx} is 1.5 times larger than ΔE_{Mx} in the case where $S = 10^4$, and it becomes negative after $\sim 1400\tau_h$. Its slower evolution is consistent with the $S^{-1/2}$ linear growth rate scaling, and due to the large resistive time the nonlinear effects are still not significant after $2000\tau_h$ or $0.02\tau_r$. The kinetic energies in Fig. 4.13b evolve with the corresponding linear growth rate. From the previous results for $S = 10^2$ and $S = 10^4$ it is evident that the nonlinear saturation becomes significant on a time scale of $0.1\tau_r$ that corresponds to $10^4\tau_h$ for $S = 10^5$.

Figures 4.14a and 4.15 are devoted to the calculation of the conservation relations of Eqs. (4.10)–(4.11). As a test of the overall behavior of the numerical code we calculated the temporal change in the total energy, and the magnetic helicity for $V = 0.3$ with the tanh profile, and compared it to the

resistive dissipation according to Eq. (4.10) and (4.11b). After an initial transit period of $\sim 20\tau_h$ a very good agreement is seen between the calculated energy dissipation and the resistive dissipation. The initial ($\lesssim 30\tau_h$) energy discrepancy is due to transient numerical solutions excited initially in the nonlinear code. Values of the actual viscosity S_v in the code were estimated using the energy conservation relation [Eq. (4.10)] and were found to be $10^3 - 10^5$. The obtained values of S_v were found to depend strongly on the amount of the numerical fourth order smoothing applied to the solutions. In the case of helicity, the conservation was two order of magnitude better than the resistive energy dissipation.

The final distribution of energies for several values of V with the tanh and sech equilibrium flow, and with $S = 10^2$, 10^4 is summarized in Table 4.1. The calculated distribution of energies for the cases with $V = 0$ agrees with the results obtained by Steinolfson and Van Hoven (1984). When $S = 10^2$ (as noted above) the change in the magnetic energy decreases with V, while the change in the kinetic energy increases with V. When $V = 0.3$ the release of the magnetic energy is approximately 3 times lower, and the change in total energy ΔE_{tot} is 6 times lower than for $V = 0$. At the same time ΔE_{Kx} increased by 50% and ΔE_{Ky} increased by a factor of ~ 3. When $S = 10^4$ and $V = 0.5$ the release of the magnetic energy is 47% of ΔE_{Mx} when $V = 0.1$, and less than 25% of the energy released without equilibrium flow. When $V = 0.5$ the change in the kinetic energies is an order of magnitude smaller than the change in the magnetic energy, and when $V = 0.1$, ΔE_K is two orders of magnitude smaller than ΔE_M. The kinetic energy is even less significant when $V = 0$.

4.5 Summary and Discussion

We have investigated the effect of equilibrium shear flow on the evolution of the nonlinear tearing mode via numerical solution of incompressible resistive MHD equations, with V ranging up to $0.5V_a$, and S up to 10^5. The perturbed flow and stream functions loose the symmetries of the $V = 0$ tearing mode and are found to distort in the direction of the equilibrium shear flow. Their mode structure in the x-direction, determined initially by the linear wavenumber α is not greatly affected during the nonlinear evolution. Additional currents are generated far from the tearing layer by the presence of relatively small shear flow, in agreement with the linear result that flow has a significant affect on the external region of the tearing mode. The amount of the released magnetic energy decreased with V, for both low resistivity ($S = 10^4$) and high resistivity ($S = 10^2$) tearing. Exponential decrease of the growth rate, and the corresponding saturation of the reconnected flux occurred in all the calculated cases; its time scale was primarily determined by the resistivity and the shear flow. Nonlinear saturation of the energies was found to occur after 0.1 τ_r. The change in the kinetic energy was seen to be two orders of magnitude lower than the magnetic energy release for small V, and one order of magnitude lower for large $V = 0.5$. The total energy and helicity dissipation were calculated and found to agree with that predicted by theory.

One potential application of the present results is to flaring loops, a phenomenon that occurs when magnetic flux tubes rise through the sheared magnetic fields of solar active regions. The loops often have flows parallel to their axis (Priest, 1981) and, hence, most likely parallel to the magnetic field. It is well known that the growth of the usual tearing mode without flow and

with classical dissipation is an order of magnitude too slow to explain the rapid energy release in such loops (Sturrock, 1980). The growth rate can be increased, of course, if the dissipative effects are somehow increased by nonclassical effects, such as turbulence. However, no generally accepted theory has been developed for such enhanced dissipation. Therefore, at least for classical dissipation, the present results predict that the tearing mode is even *less* likely to play a role in the energy release in flaring loops with flows.

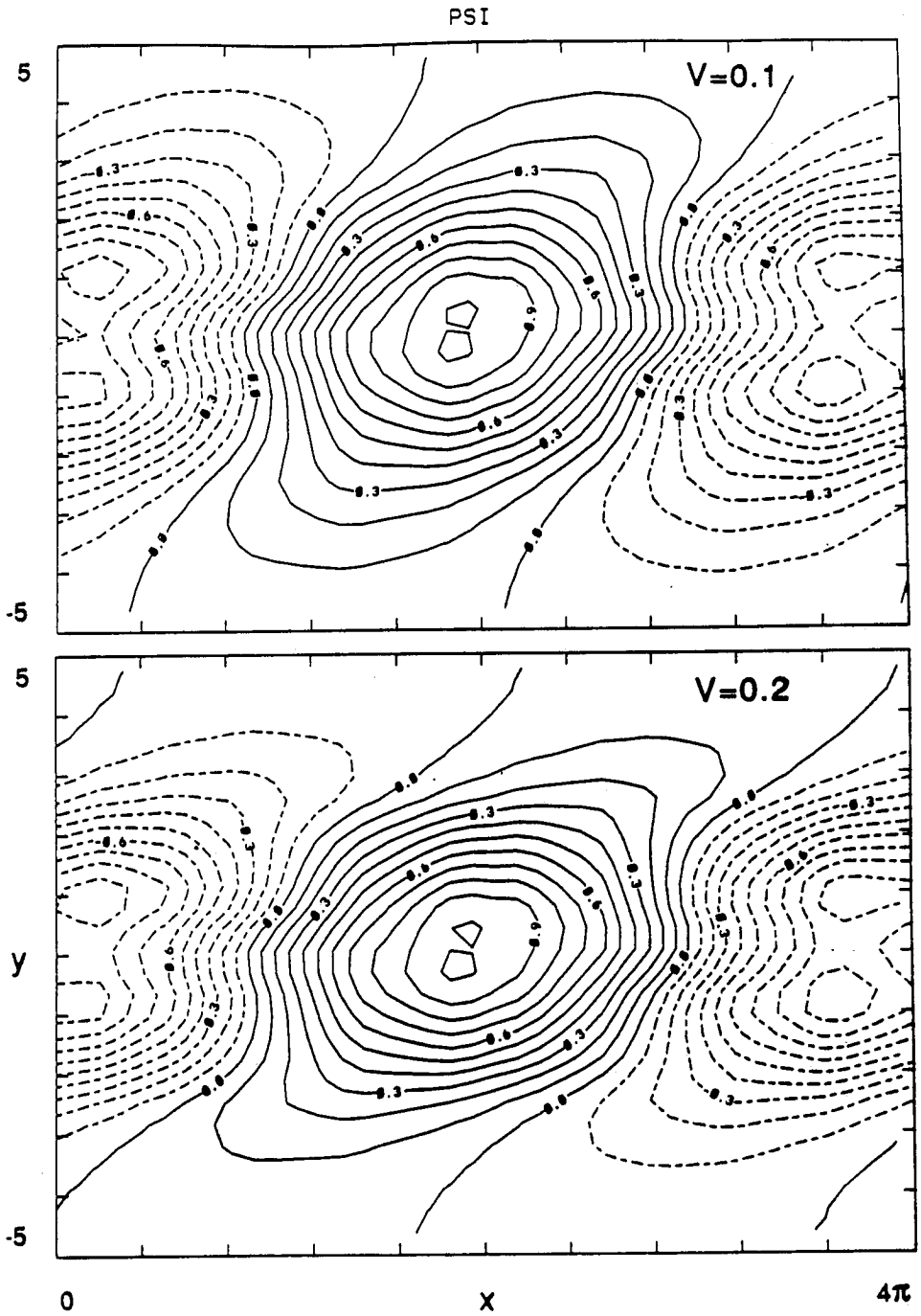

Figure 4.1: Spatial dependence of the flux functions with $S = 10^2$, $V = 0.1$ (top figure), $V = 0.2$ (bottom figure) and tanh equilibrium flow profile.

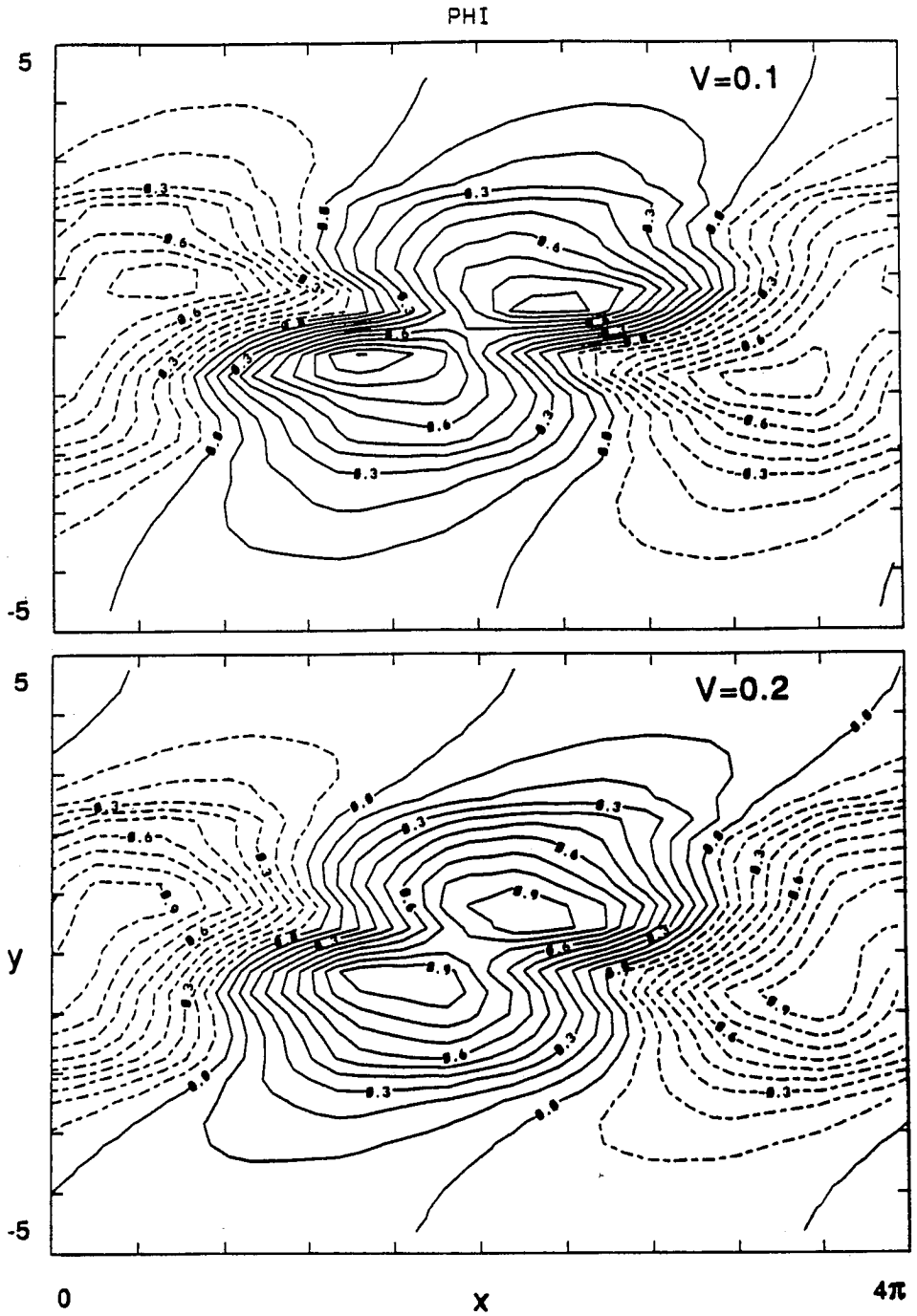

Figure 4.2: Spatial dependence of the stream functions with $S = 10^2$, $V = 0.1$ (top figure), $V = 0.2$ (bottom figure) and tanh equilibrium flow profile.

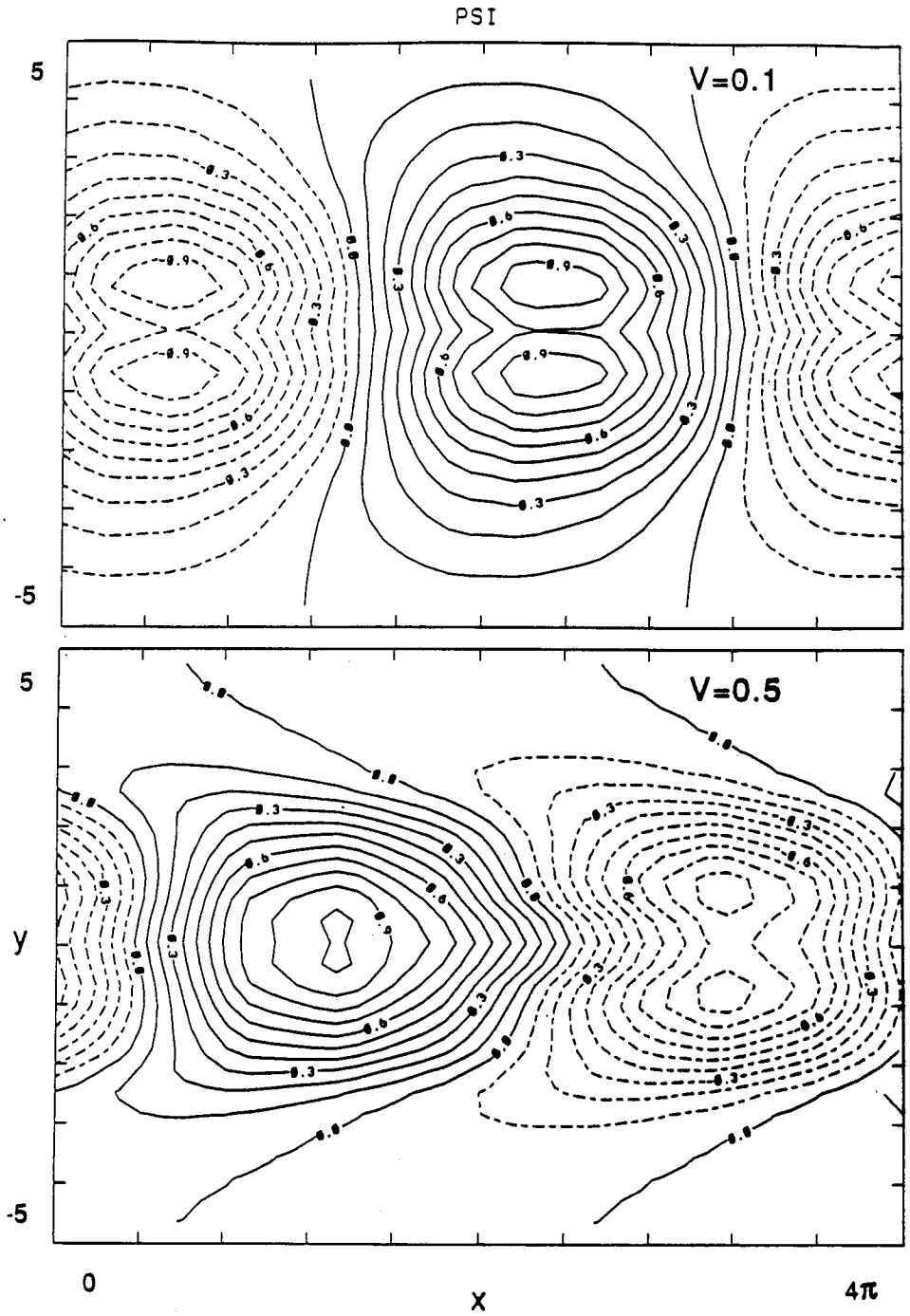

Figure 4.3: Spatial dependence of the flux functions with $S = 10^2$, $V = 0.1$ (top figure), $V = 0.5$ (bottom figure), and sech equilibrium flow profile.

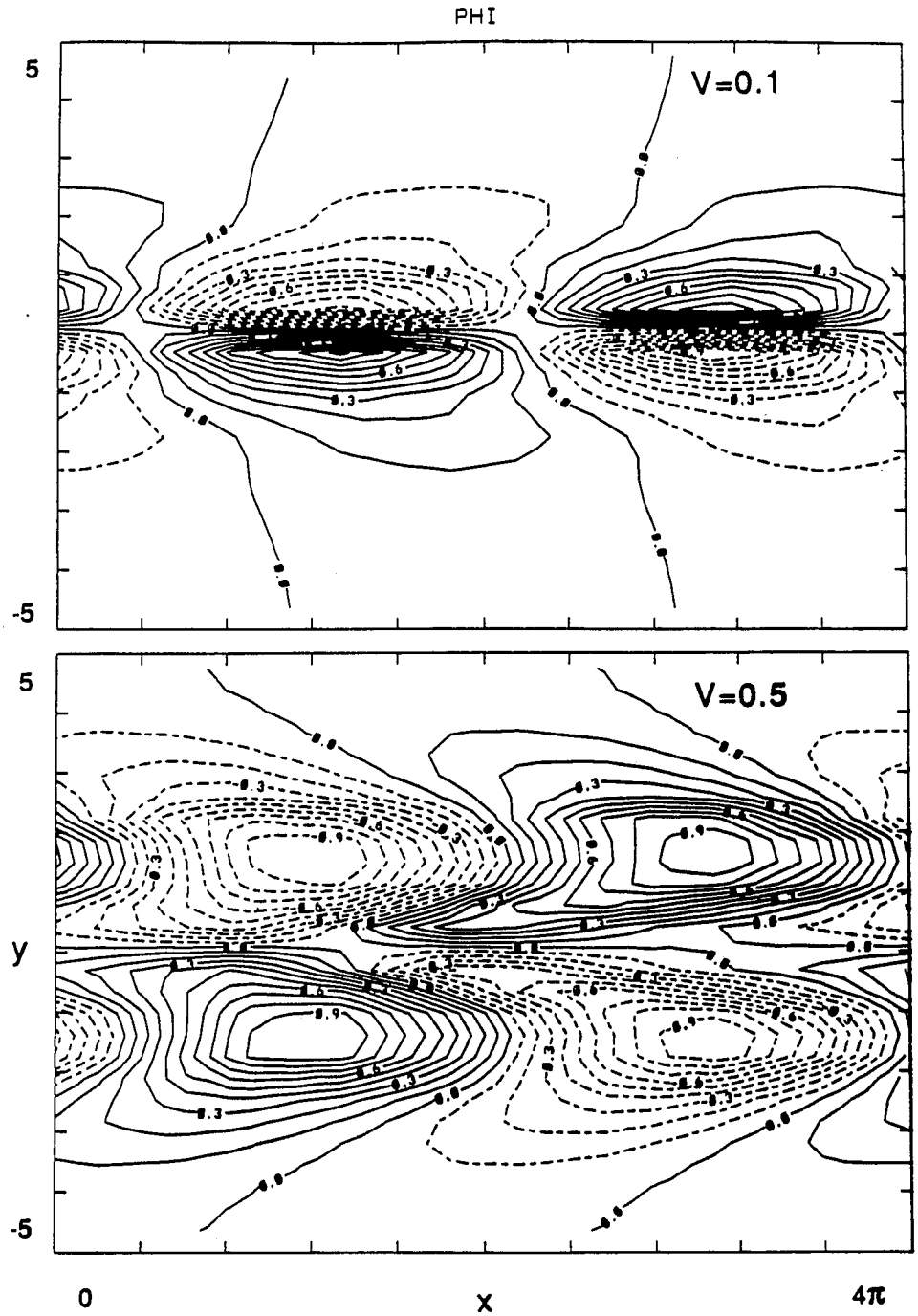

Figure 4.4: Spatial dependence of the stream functions with $S = 10^2$, $V = 0.1$ (top figure), $V = 0.5$ (bottom figure), and sech equilibrium flow profile.

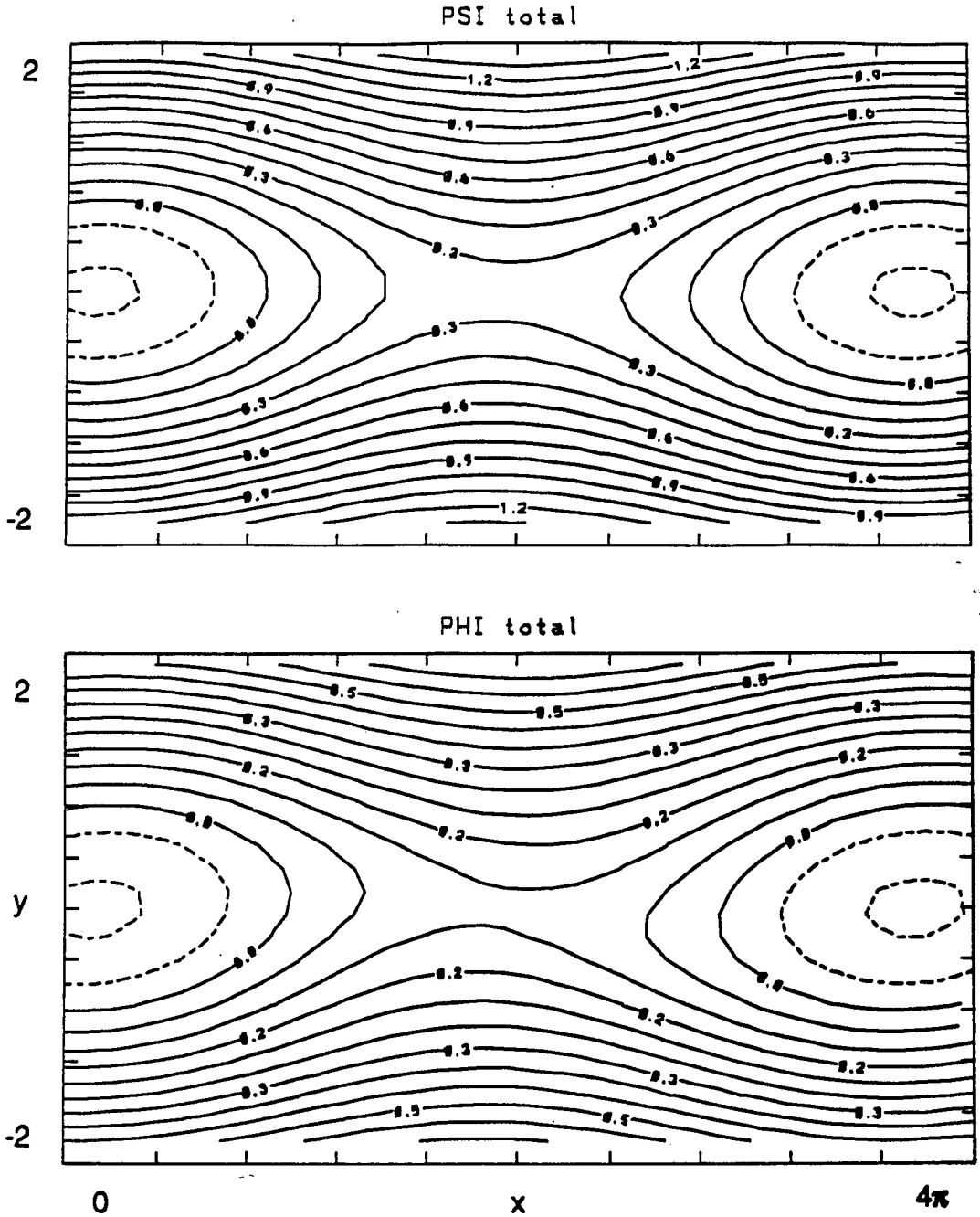

Figure 4.5: Contour plot of Ψ and Φ with $V = 0.5$, $S = 10^2$, and the tanh flow profile.

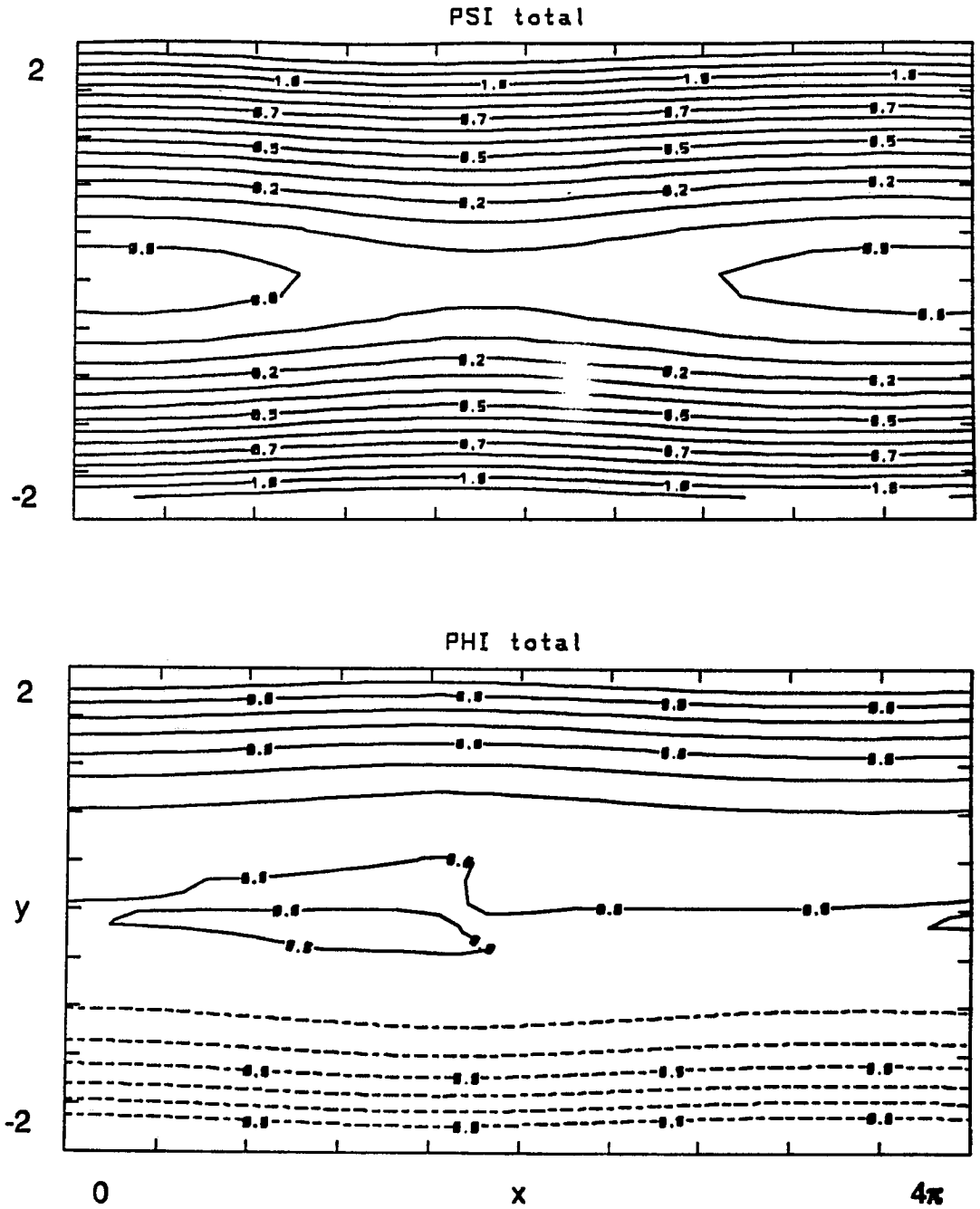

Figure 4.6: Contour plot of Ψ and Φ with $V = 0.1$, $S = 10^4$, and the sech flow profile.

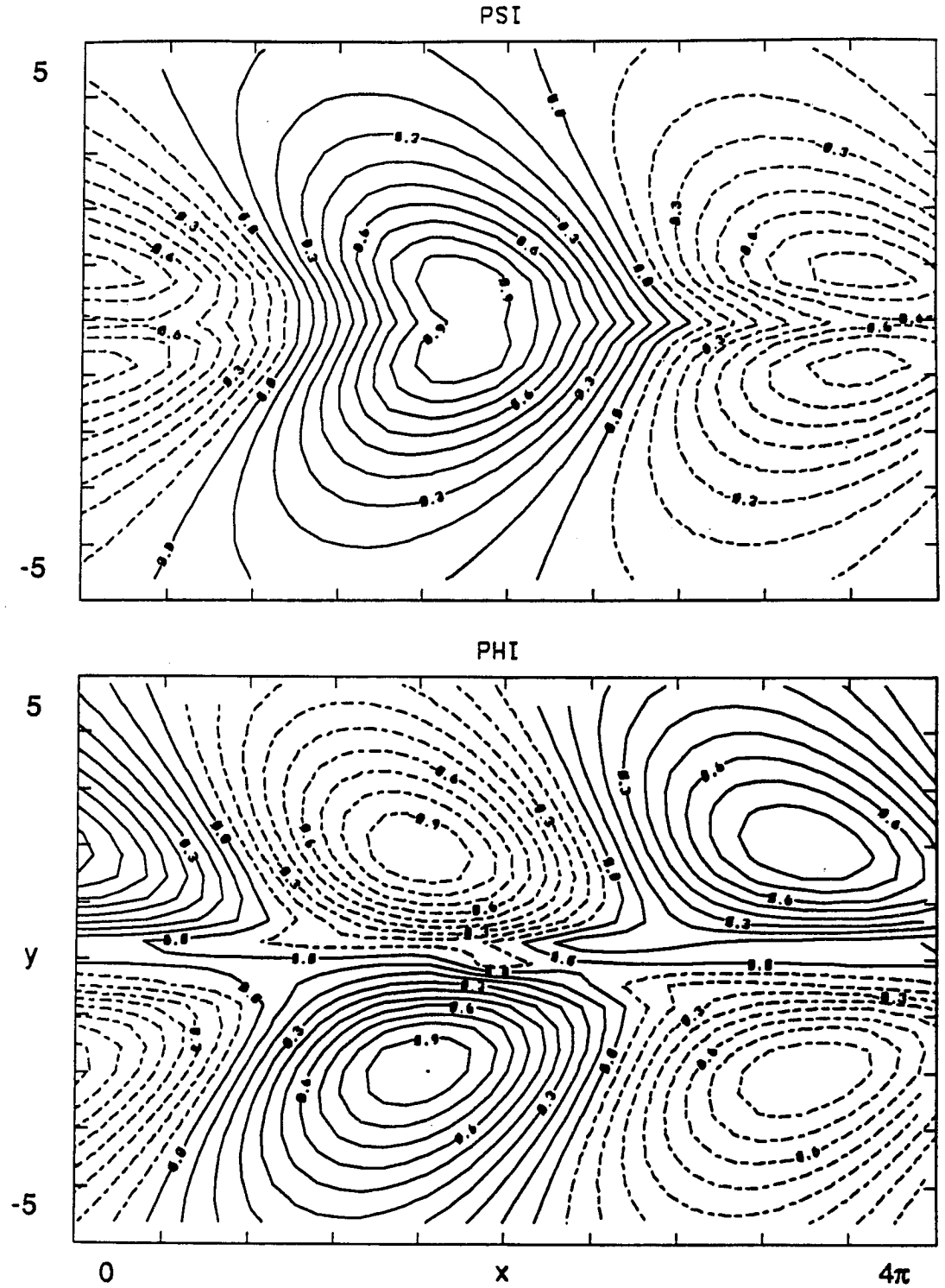

Figure 4.7: Contour plot of ψ and ϕ with $V = 0.1$, $S = 10^4$, and the sech flow profile.

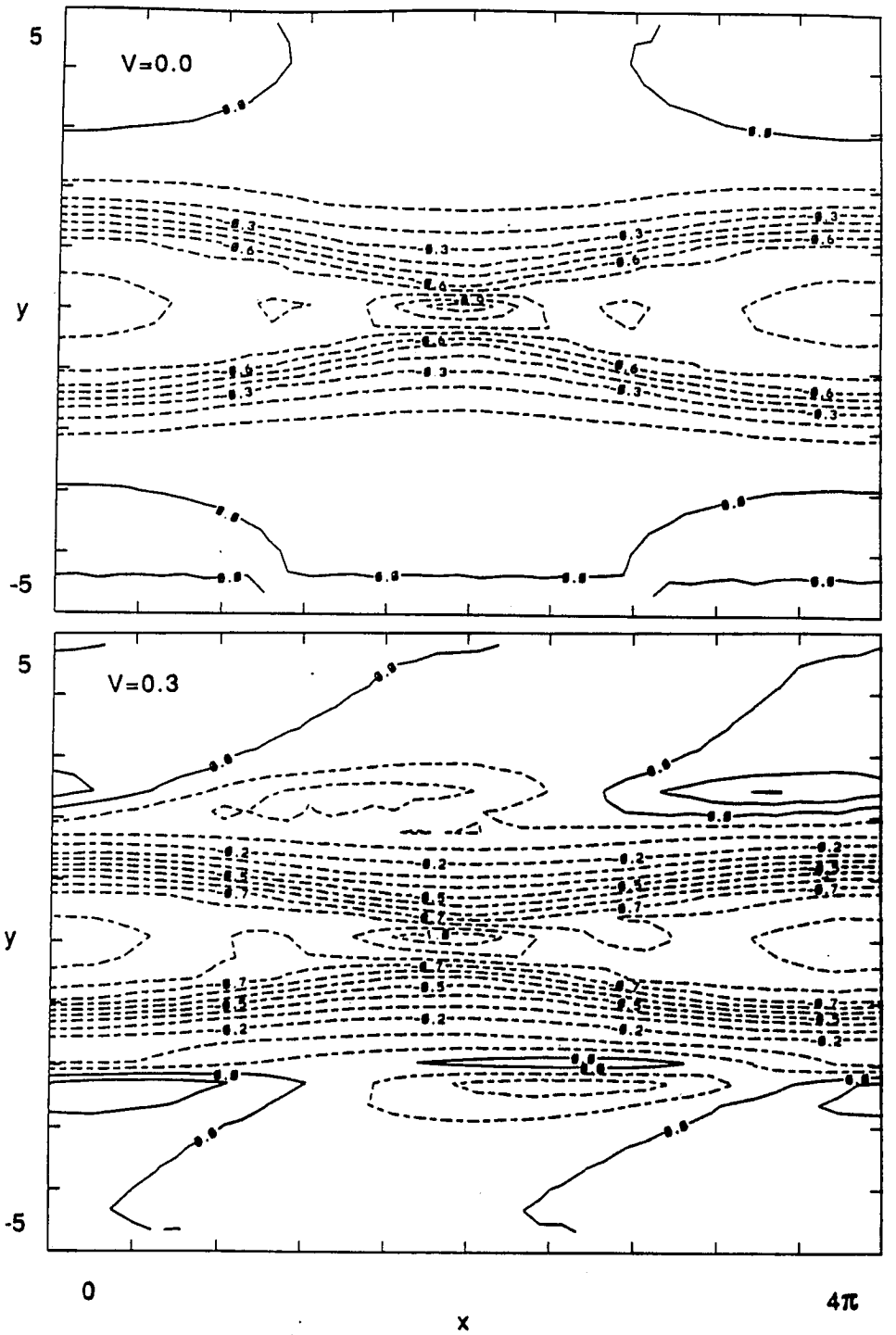

Figure 4.8: Contour plot of $J = -\nabla^2\psi$ with $V = 0.0$ (top figure), and $V = 0.3$ (bottom figure) and the tanh flow profile for $S = 10^2$.

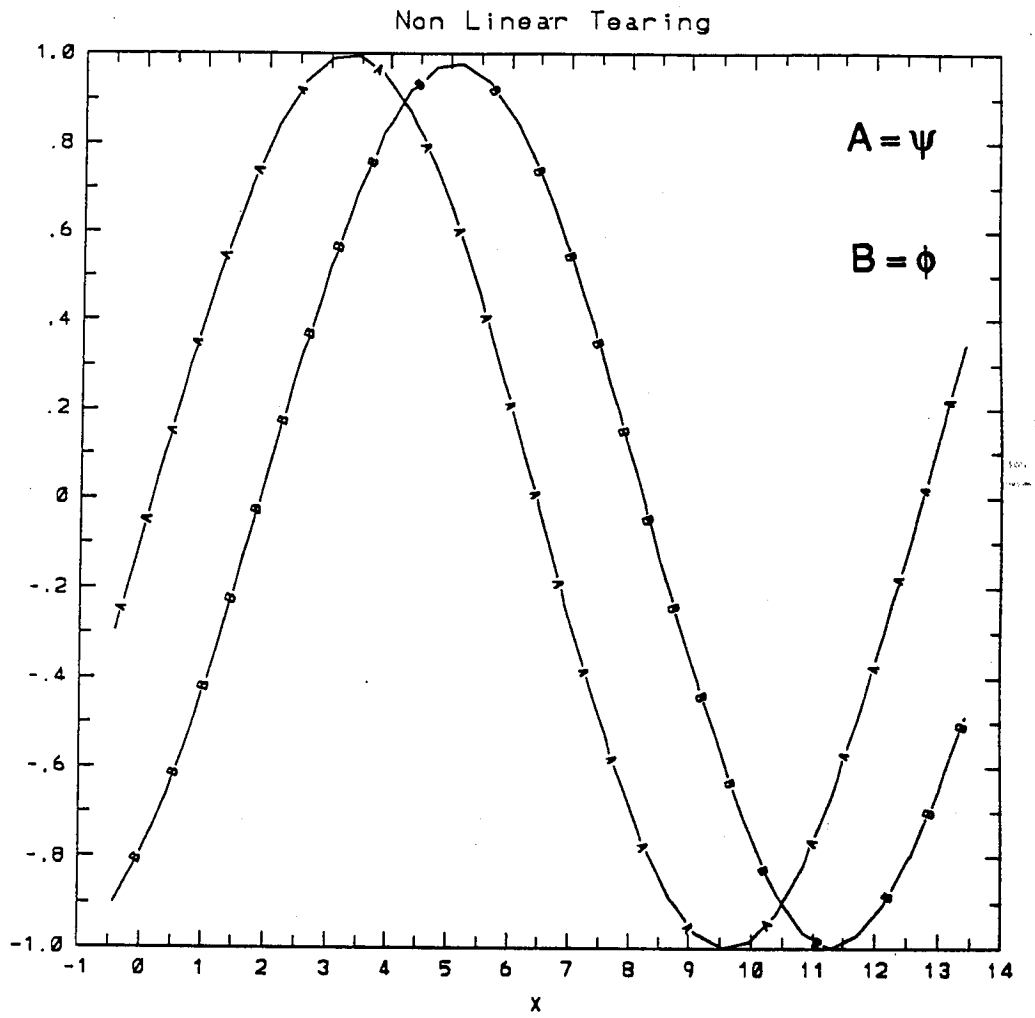

Figure 4.9: The mode structure of ψ and ϕ with $V = 0.3$ and the tanh equilibrium flow profile for $S = 10^2$.

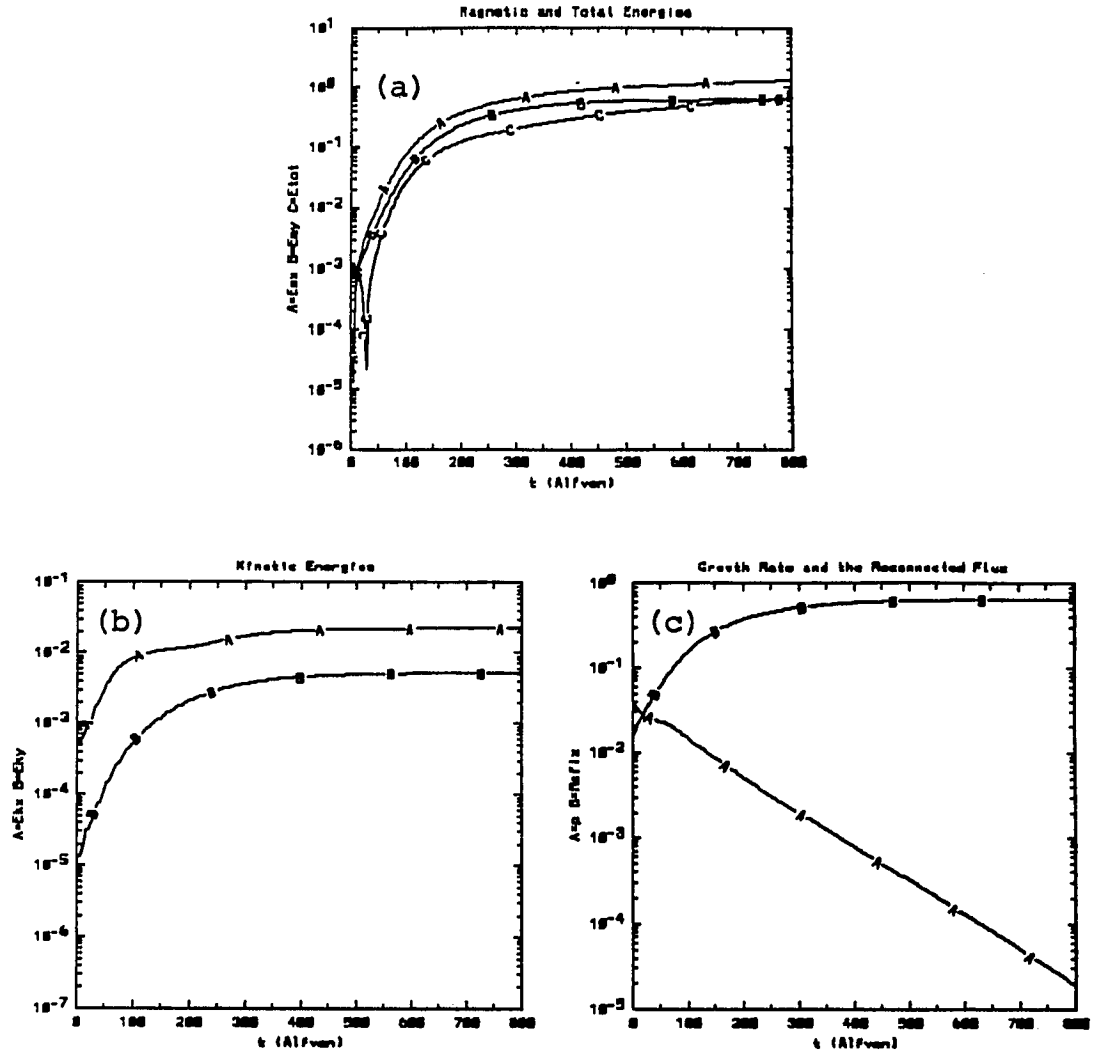

Figure 4.10: The temporal evolution for the case where $S = 10^2$, $V = 0.1$ with the tanh equilibrium flow profile.
(a) The growth rate (curve A) and the reconnected flux (curve B). (b) ΔE_{Mx} (curve A), ΔE_{My} (curve B), and ΔE_{tot} (curve C).(c) ΔE_{Kx} (curve A), ΔE_{Ky} (curve B).

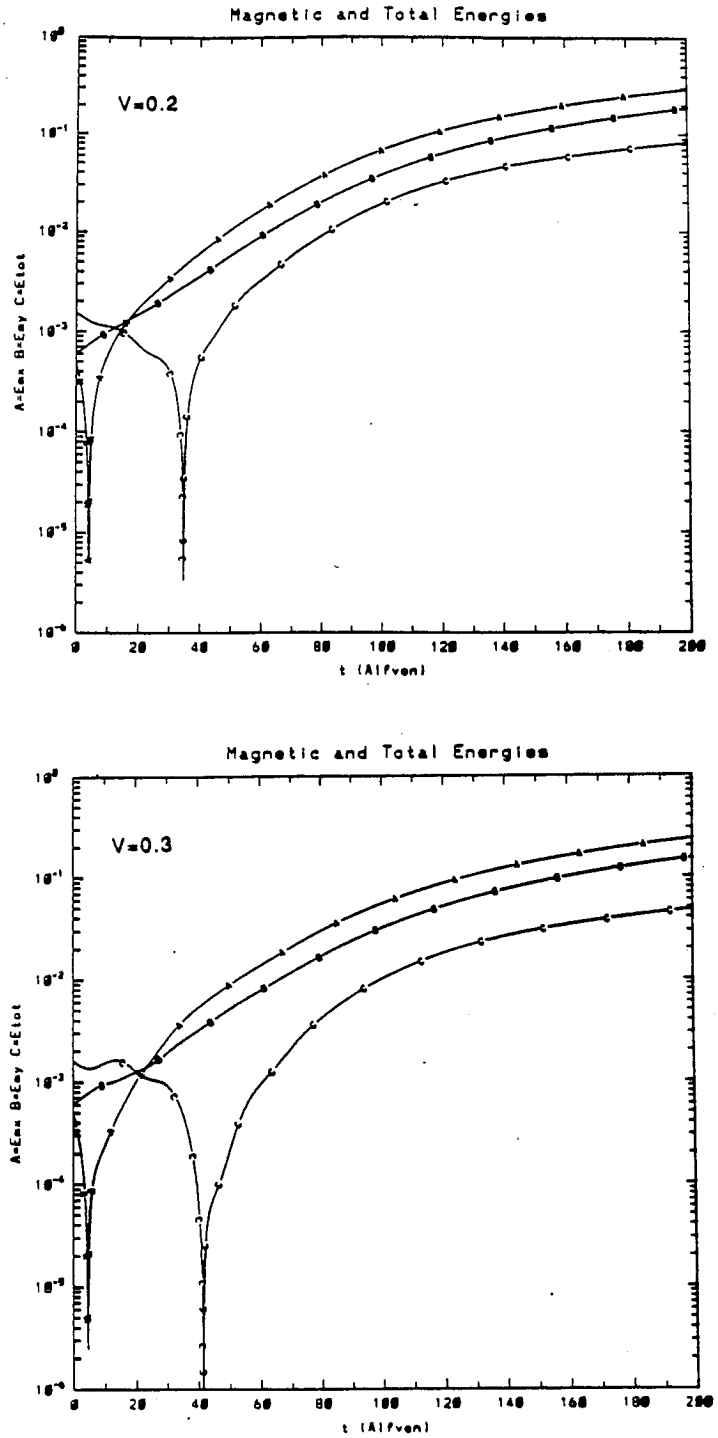

Figure 4.11: The temporal evolution of ΔE_{Mx} (curve A), ΔE_{My} (curve B), and ΔE_{tot} (curve C), with $V = 0.2$ (top figure), and $V = 0.3$ (bottom figure).

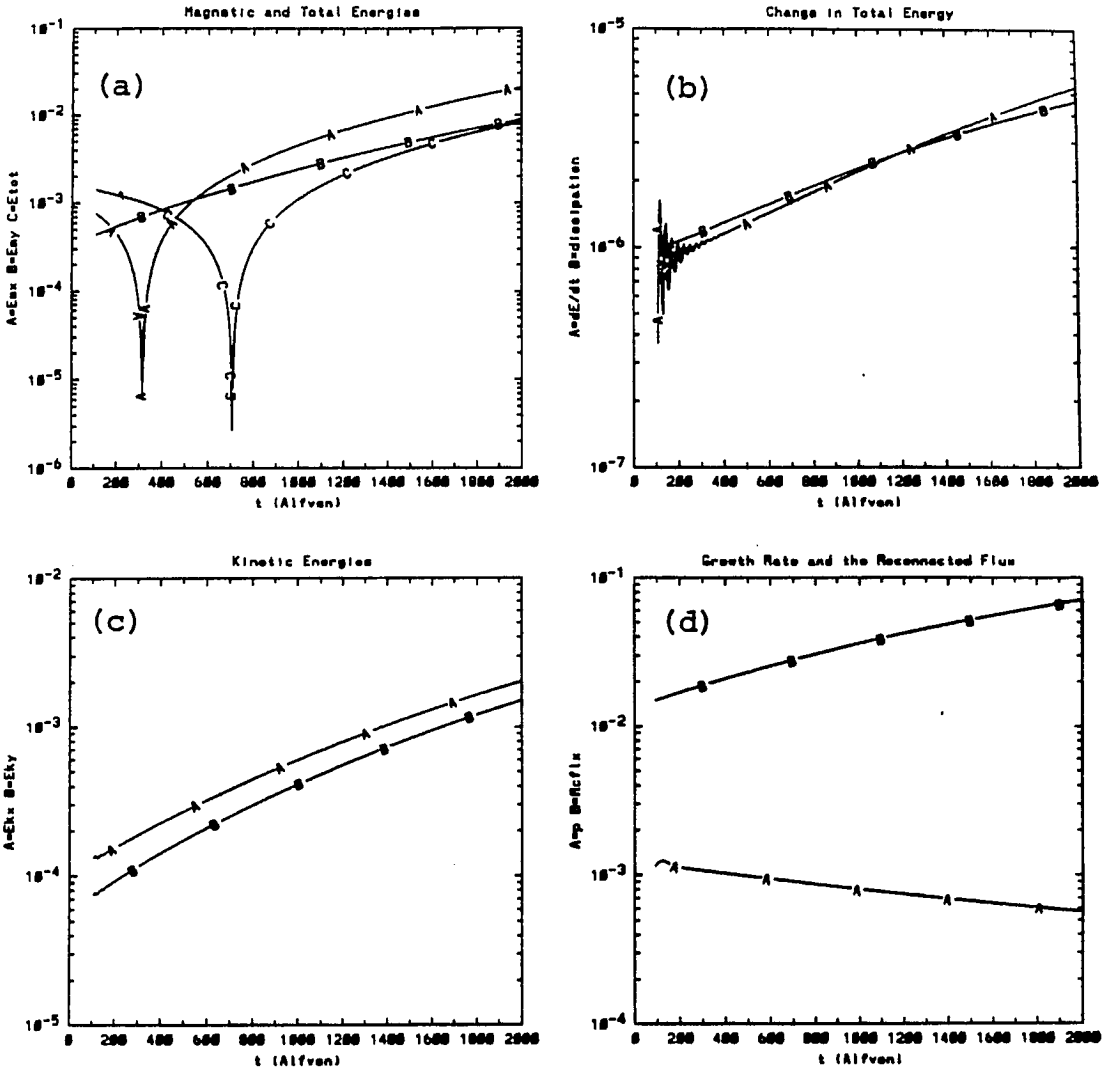

Figure 4.12: The nonlinear evolution of the $S = 10^4$, $V = 0.5$ tearing mode with the tanh equilibrium flow profile.
(a) ΔE_{Mx} (curve A), ΔE_{My} (curve B), and ΔE_{tot} (curve C). (b) The total energy dissipation $dE_{\rm tot}/dt$ (curve A), and the resistive dissipation (curve B). (c) ΔE_{Kx} (curve A), ΔE_{Ky} (curve B). (d) The temporal evolution of the growth rate (curve A) and the reconnected flux (curve B).

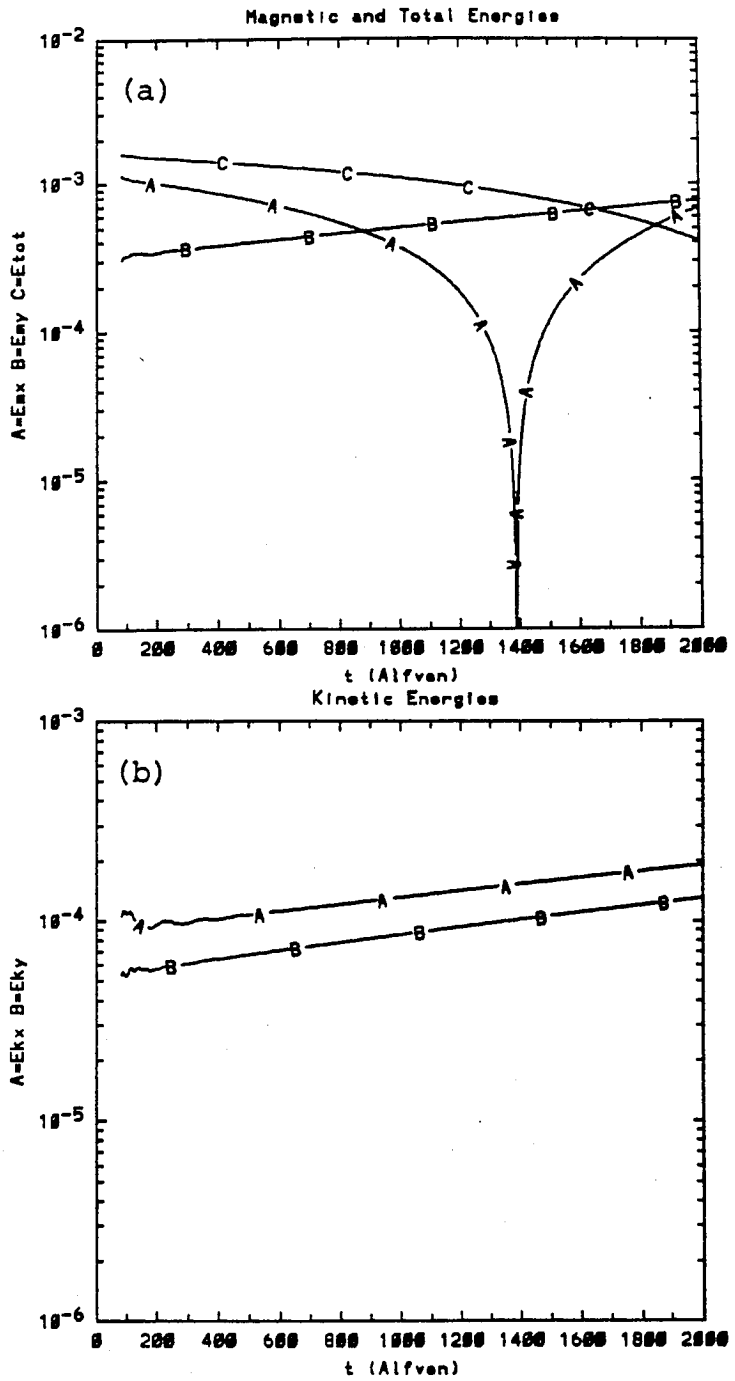

Figure 4.13: The nonlinear evolution for the case where $S = 10^5$, $V = 0.5$ with the tanh equilibrium flow profile.
(a) ΔE_{Mx} (curve A), ΔE_{My} (curve B), and ΔE_{tot} (curve C).(b) ΔE_{Kx} (curve A), ΔE_{Ky} (curve B).

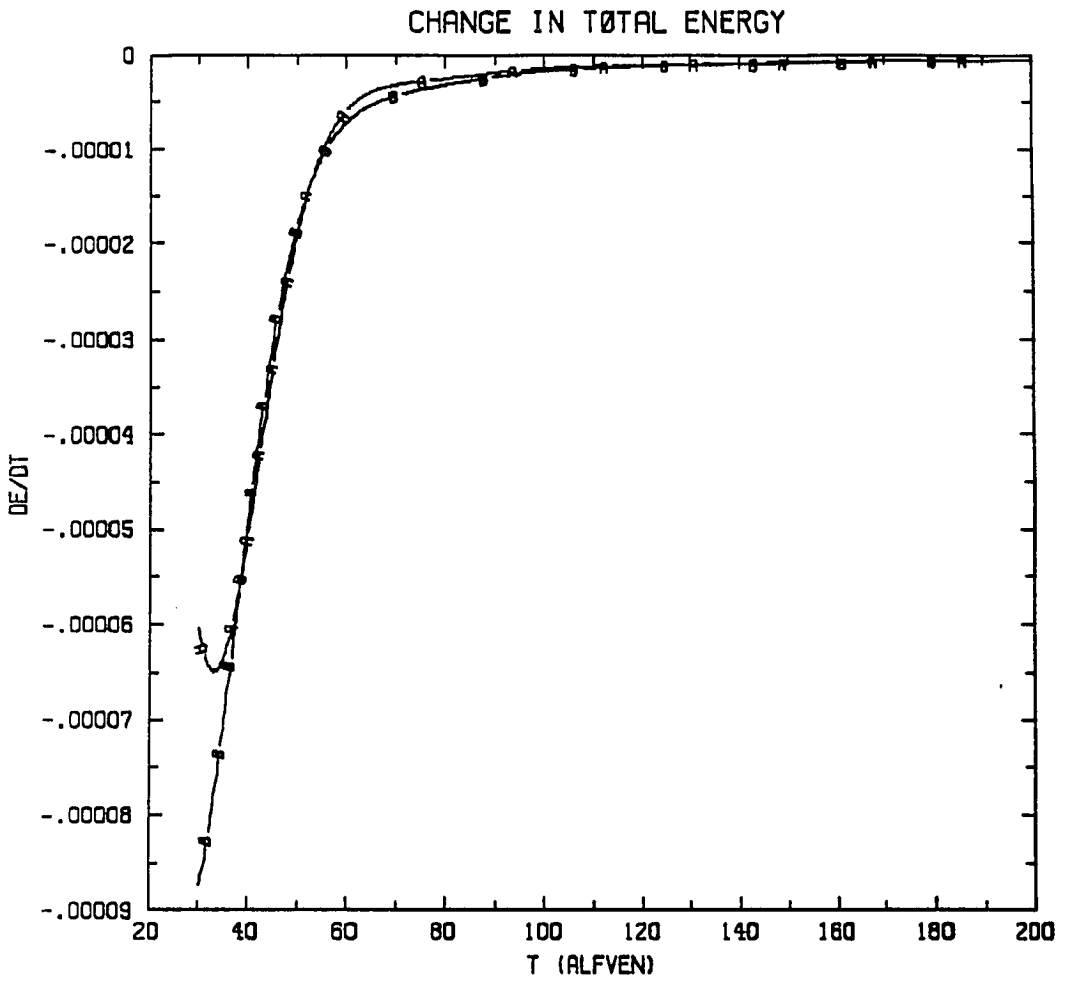

Figure 4.14: Numerical test of the energy conservation relation with $S = 10^2$. The energy dissipation as calculated from the l.h.s. of Eq. (4.10) (curve A), and the r.h.s. of Eq. (4.10) (curve B).

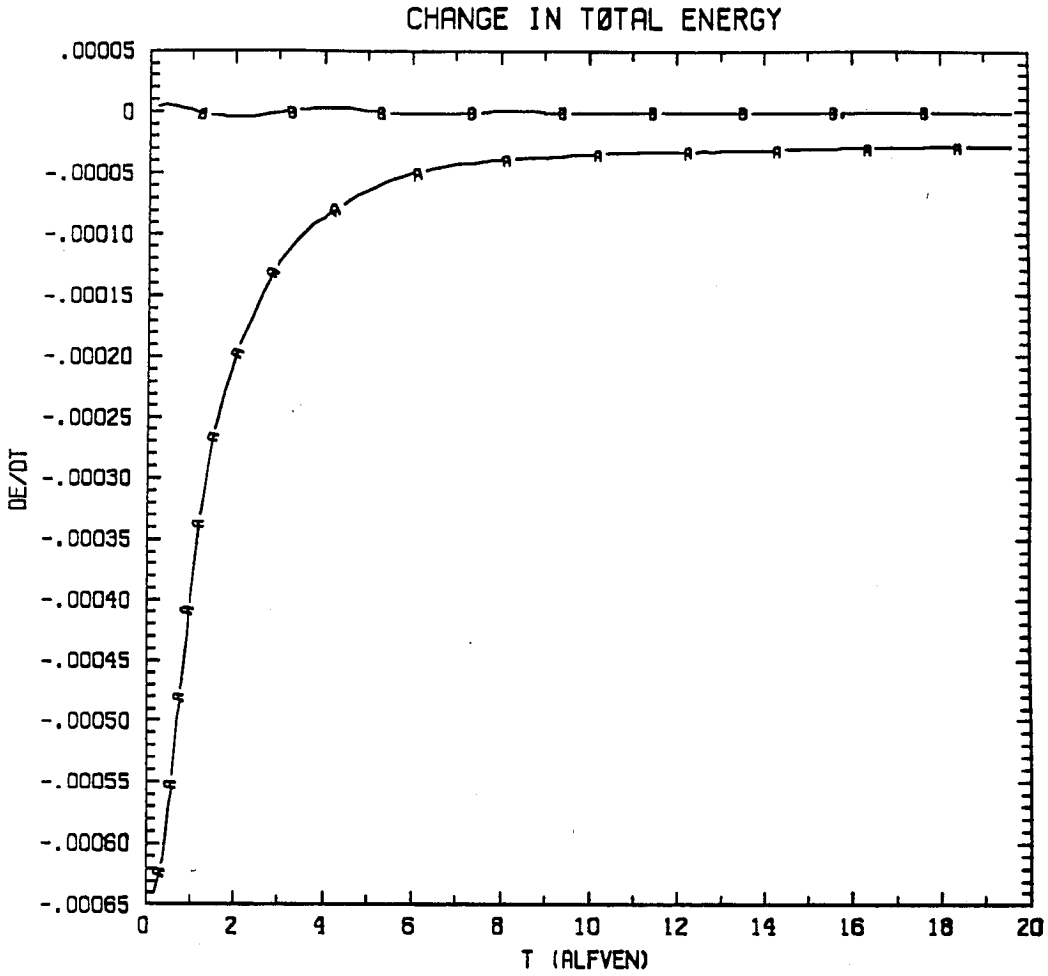

Figure 4.15: Numerical test of the helicity conservation relations with $S = 10^2$. The magnetic helicity dissipation as calculated from l.h.s. of Eq. (4.11) (curve A), and the r.h.s. of Eq. (4.11) (curve B).

Chapter 5

Resistive Reconnection of an X-type Neutral Point

5.1 Introduction

Magnetic reconnection is believed to occur in solar coronal loops, the magnetopause boundary, the solar wind, extragalactic jets and fusion experiments. Giovanelli (1947) was the first to observe that solar flares frequently occur near magnetic neutral points. Based on these observations Dungey (1953, 1958) proposed an x-type neutral point mechanism for particle acceleration, onset of sheet currents, and energy release in solar flares, provided that the magnetic field sources are free to move. Chapman and Kendall (1962) solved the nonlinear ideal MHD equations for the x-type neutral point and found growth on an Alfvén time scale, while Syrovatsky (1966) included the mechanism in a solar flare model. Sweet (1958) and Parker (1963) used dimensional arguments for a model involving merging of antiparallel magnetic fields, and concluded that the reconnection rate scales as $\eta^{1/2}$, while Petschek (1964) predicted an Alfvénic reconnection rate based on semi-quantitative Alfvén shock wave solutions. As stated in Chapter 2, Furth, Killeen and Rosenbluth (1963) developed analytic boundary layer theory, and derived the $\eta^{3/5}$ linear tearing growth rate scaling, while Rutherford (1973) considered the nonlinear stage (see, Chapter 4) and found that in the reconnected flux $\Phi \sim \eta t$ and the reconnection rate diminishes from an exponential to an algebraic rate. Hassam (1991), and Craig and McClymont (1991) have considered an x-point mag-

netic field configuration with fixed (conducting wall) boundary conditions and solved the linearized compressible MHD equations, for azimuthally symmetric $m = 0$ modes, both analytically and numerically. They found that the perturbed x-point magnetic configuration relaxes to the force-free x-point with an intermediate decay rate that is slower than the Alfvén rate, but faster than the resistive diffusion rate. Experimental studies by Bratenahl and Yeates (1970), Baum and Bratenahl (1974a,b), Baum *et al.* (1973a,b) found that the initially perturbed x-type magnetic field configuration will rapidly relax to the force-free state. For a detailed review see for example Priest (1981).

Here we solve the 2-D nonlinear resistive MHD equations and the linear dispersion relation with conducting wall boundary conditions, and find the rate for relaxation of the stressed (perturbed) x-point back to the force-free x-point configuration. We find (not surprisingly) that the type of boundary conditions imposed determine the subsequent evolution. Conducting wall boundaries that are more appropriate to fusion devices and laboratory plasma, lead to relaxation of the stressed x-point back to the unstressed state. Free, or sheared boundary conditions that are more appropriate to space plasma (see, for example, Vekstein and Priest, 1992) may lead to instability and transition from an x-point to sheet current of the type proposed by Dungey (1958) to explain solar flares.

This chapter is organized as follows: In Sec. 5.2 the basic MHD equations for our model, and the initial magnetic field configuration are presented. In Sec. 5.3 we present the linear dispersion relation. Section 5.4 is devoted to the numerical results of the nonlinear MHD simulations, and the summary and discussion are in Sec. 5.5.

5.2 Incompressible 2-D MHD Equations

We assume that collisional MHD theory (Drake and Lee, 1977) is applicable, that the plasma resistivity η is constant and isotropic, and that gravitational and viscous effects are negligible. We use Eqs. (1.1)–(1.5) with the equilibrium Eq. (5.3) below. Assuming that the evolution is two-dimensional ($\frac{\partial}{\partial z} = 0$) we solve the above set of equations using three separate approaches:

1. Solution of the dispersion relation arising from the linearized Eqs. (1.1)–(1.4), with the assumption $\nabla P = 0$ in Eq. (1.1).

2. Numerical solution of the 2-D MHD equations in slab geometry given below in Eqs. (5.4)–(5.5), which are derived from Eqs. (1.1)–(1.4) with the assumption of incompressibility ($\nabla \cdot \mathbf{v} = \mathbf{0}$).

3. Numerical solution of the compressible MHD Equations (1.1)–(1.3) and Eq. (1.5) in the (r, θ) plane without any further approximations [Eq. (1.4) is not solved explicitly]

The linearized equations resulting from the first approach and their solution will be presented in Sec. 5.3. In the remainder of this section we present the equations arising from the second approach.

The 2-D incompressible MHD equations are obtained as follows. The magnetic field and velocity are written as

$$\mathbf{B} = \nabla\Psi \times \mathbf{e}_z \tag{5.1}$$

$$\mathbf{V} = \nabla\phi \times \mathbf{e}_z \tag{5.2}$$

where Ψ and ϕ are the flux and stream functions respectively, and $\Psi = \psi_E + \psi$ with the equilibrium stream function ψ_E given by

$$\psi_E = B_0(x^2 - y^2)/2a. \tag{5.3}$$

The contour lines of ψ_E (which are parallel to the magnetic field lines) are shown in Fig. 5.1. Next, substituting Eqs. (5.1)–(5.3) in Eqs. (1.1)–(1.2) with $\rho = \rho_0 = const.$, and taking a curl of Equation (1.1) to eliminated the pressure P, we obtain the following set of equations in dimensionless form:

$$\frac{\partial \psi}{\partial t} = -\frac{\partial \phi}{\partial y}\left(\frac{\partial \psi}{\partial x} + x\right) + \left(\frac{\partial \psi}{\partial y} - y\right)\frac{\partial \phi}{\partial x} - \frac{1}{S}J \tag{5.4}$$

$$\frac{\partial \omega}{\partial t} = -\frac{\partial \phi}{\partial y}\frac{\partial \omega}{\partial x} + \frac{\partial \phi}{\partial x}\frac{\partial \omega}{\partial y} + \left(\frac{\partial \psi}{\partial y} - y\right)\frac{\partial J}{\partial x} - \left(\frac{\partial \psi}{\partial x} + x\right)\frac{\partial J}{\partial y}, \tag{5.5}$$

where $J = -\nabla_\perp^2 \psi$ is the z-component of the current, $\omega = -\nabla_\perp^2 \phi$ is the z-component of the vorticity, and $\nabla_\perp^2 \equiv \frac{\partial^2}{\partial x^2} + \frac{\partial^2}{\partial y^2}$ with $\frac{\partial}{\partial z} = 0$. The time is normalized to the Alfvén time $\tau_h = a_b(4\pi\rho_0)^{1/2}/B_0$, the coordinates are scaled in units of the typical magnetic field variation length a_b, and B_0 is the average magnitude of the magnetic field at the boundary. The dimensionless parameter in these equations is the magnetic Reynolds number $S = \tau_r/\tau_h$, where $\tau_r = 4\pi a_b^2/c^2\eta$ is the resistive diffusion time. We have also assumed that the equilibrium magnetic field is maintained by an external electric field (i.e., the equilibrium magnetic field is not dissipated resistively). In Sec. 5.4 we present the numerical results obtained with Eqs. (5.4)–(5.5).

5.3 Linear Dispersion Relation

We neglect the pressure gradient and linearize the MHD equations around the equilibrium quantities ψ_E, $\rho_0 = 1$, and $\mathbf{v}_0 = 0$, whereupon Eqs. (1.1)–(1.3) in terms of ψ, ρ, and $\mathbf{v}$ become

$$\frac{\partial \rho}{\partial t} + \nabla \cdot \mathbf{v} = 0 \tag{5.6}$$

$$\frac{\partial \mathbf{v}}{\partial t} = -\nabla \psi_E \nabla^2 \psi \tag{5.7}$$

$$\frac{\partial \psi}{\partial t} + \mathbf{v} \cdot \nabla \psi_E = S^{-1} \nabla^2 \psi. \tag{5.8}$$

Next, upon multiplying Eq. (5.7) by $\nabla \psi_E$, Eqs. (5.6)–(5.8) can be combined into a single equation for ψ,

$$\frac{\partial^2 \psi}{\partial t^2} - S^{-1} \frac{\partial}{\partial t} \nabla^2 \psi = |\nabla \psi_E|^2 \nabla^2 \psi, \tag{5.9}$$

where $|\nabla \psi_E|^2 = r^2 = x^2 + y^2$. Assuming the following separation of variables in cylindrical geometry $\psi(r, \theta, t) = e^{-\gamma t} f(r) e^{im\theta}$, the eigenvalue equation for $f(r)$ becomes

$$r \frac{d}{dr} \left(r \frac{df}{dr} \right) = \left(\frac{\gamma^2}{1 - \gamma / S r^2} + m^2 \right) f. \tag{5.10}$$

The conducting wall boundary condition is given by

$$f(r = 1) = \psi(r = 1, \theta) = 0. \tag{5.11}$$

Equation (5.10) is mapped into the hypergeometric equation by the transformations $z = r^2 S / \gamma$, and $f = z^\alpha \xi$:

$$z(z - 1)\xi'' + (m + 1)(z - 1)\xi' - \gamma^2 / 4\xi = 0, \tag{5.12}$$

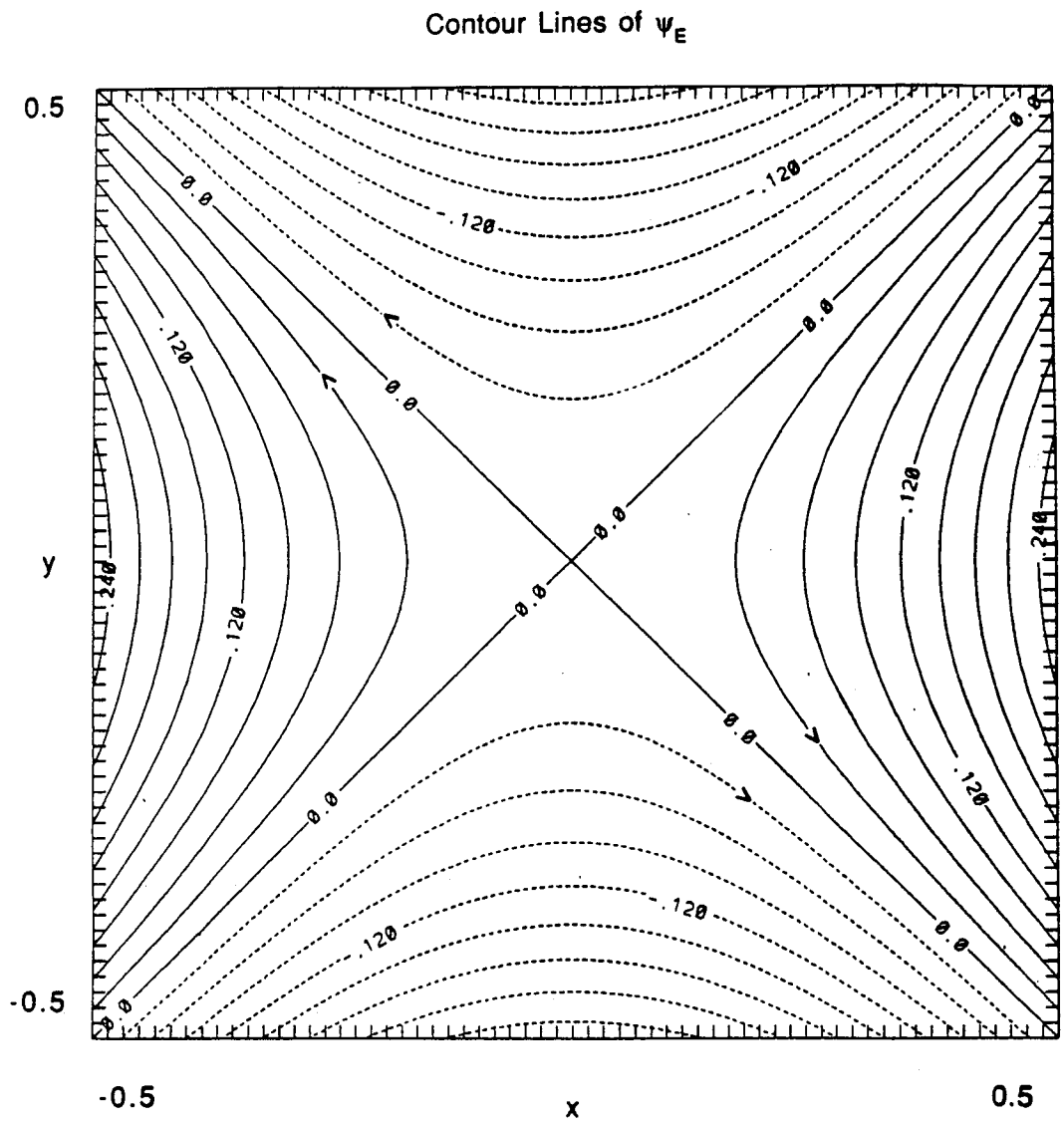

Figure 5.1: The initial equilibrium magnetic field configuration with an x-point.

where we have set $\alpha = m/2$. The solution of Eq. (5.12) that is regular at $r = 0$ is the hypergeometric function $F(a, b, c, z)$ with $a = m/2 + \Delta/2$, $b = m/2 - \Delta/2$, $c = m + 1$, and $\Delta = \sqrt{m^2 + \gamma^2}$. From the boundary condition (5.11) we obtain the dispersion relation,

$$F(m/2 + \Delta/2, m/2 - \Delta/2, m + 1, S/\gamma) = 0. \tag{5.13}$$

For the cases of interest, $|z| = |S/\gamma| > 1$; hence, the transformation formula (Oberhettinger, 1972),

$$F(a, b, c, z) = \frac{\Gamma(c)\Gamma(b-a)}{\Gamma(b)\Gamma(c-a)}(-z)^{-a}F(a, 1-c+a, 1-b+a, 1/z) +$$

$$+\frac{\Gamma(c)\Gamma(a-b)}{\Gamma(a)\Gamma(c-b)}(-z)^{-b}F(b, 1-c+b, 1-a+b, 1/z),\ |arg(-z)| < \pi \tag{5.14}$$

is needed to obtain the dispersion relation. Substituting the values of a, b, and c, using the properties of the Gamma function, and using Eq. (5.13) yields the following linear dispersion relation for the reconnecting x-point:

$$\frac{(m+\Delta)\Gamma(-\Delta)\Gamma^2(m/2+\Delta/2)}{(m-\Delta)\Gamma(\Delta)\Gamma^2(m/2-\Delta/2)} =$$

$$= -\left(-\frac{S}{\gamma}\right)^{\Delta} \frac{F(m/2-\Delta/2, -m/2-\Delta/2, 1-\Delta, \gamma/S)}{F(m/2+\Delta/2, -m/2+\Delta/2, 1+\Delta, \gamma/S)} \tag{5.15}$$

Equation (5.15) can be further simplified with the assumption $\gamma/S \ll 1$, which results in the following asymptotic expression for the r.h.s of 5.15

$$= -\left(-\frac{S}{\gamma}\right)^{\Delta} \frac{1 + \frac{\gamma^3}{4S(1-\Delta)}}{1 + \frac{\gamma^3}{4S(1+\Delta)}}. \tag{5.16}$$

A special case of this dispersion relation for $n = m = 0$ was derived by Hassam (1991). When $m = n = 0$ and in the limit $|\gamma| \ll 1$, the dispersion

relation (5.15) can be approximated by the following asymptotic expressions:

$$Im\,\gamma \sim \frac{\pi}{\log S}\left[1 - \frac{\log(\log S))}{\log S}\right] \tag{5.17}$$

$$Re\,\gamma \sim \frac{\psi/2}{\log S} Im\,\gamma \sim \frac{\pi^2}{2(\log S)^2}. \tag{5.18}$$

We have solved the dispersion relation (5.15) numerically for both $m = 0$, and $m \neq 0$, with S varied over several orders of magnitude. We have used the values of γ from Eqs. (5.17)–(5.18) as an initial guess in our numerical solution of the exact dispersion relation. The resulting decay rates and their dependence on S, with $m = n = 0$ and $n = 1,\ m = 2, 4$ are presented in Fig. 5.2. The near linear dependence for the various modes agrees with the $\log S$ scaling of Eqs. (5.17)–(5.18). The real and imaginary parts of the eigenfunction $f(r)$ with $m = 0$, $n = 1$, $S = 10^3$ and $m = 1$, $n = 3$, $S = 10^5$ are presented in Fig. 5.3. The "quantum" number n determines the number of radial nodes of $f(r)$ in the interval $r \in (0, 1)$. When $m = 0$, $Re\{f(r)\}$ approaches a constant as $r \to 0$. When $m = 1$, $f(r \to 0) \to 0$. The solution of the exact dispersion relation for the $n = m = 0$ modes is compared with the asymptotic expression (5.18) for $10 \leq S \leq 10^{100}$, and with the decay rates obtained from the incompressible MHD simulation. For $S = 10^4$ (characteristic of laboratory plasmas) the $n = m = 0$ perturbation decay time is about 20 Alfvén times with similar oscillation period. For $S = 10^{10}$ (a typical value for the solar coronal plasma) the $n = m = 0$ perturbation decay time is about 120 Alfvén times and is longer than two oscillation periods. Very good agreement is seen in Fig. 5.4 between the nonlinear simulation with $10^2 \leq S \leq 4 \cdot 10^4$, the exact dispersion relation, and the asymptotic expression. The nonlinear terms in the MHD simulations become smaller as the perturbation decays, and the

decay rates approach the linear rate (see Appendix). The asymptotic nature of Eq. (5.18) is evident from the figure, since agreement with the dispersion relation is improved at very larger values of S.

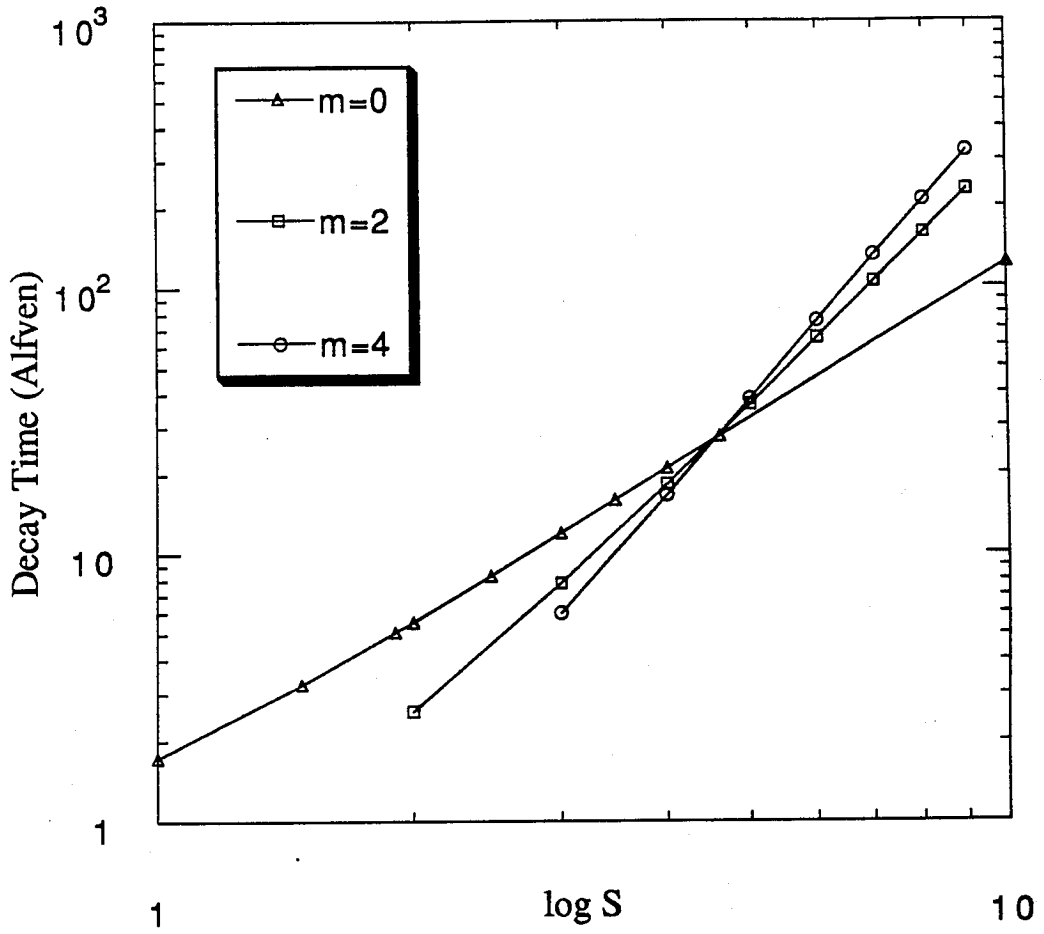

Figure 5.2: Decay rates of the modes with $m = n = 0$, and $n = 1$, $m = 2, 4$ obtained from the solution of the linear dispersion relation.

5.4 Nonlinear Simulations

5.4.1 Incompressible MHD

Now we describe results obtained by using the Alternative Direction Implicit (ADI) method to solve the 2-D incompressible MHD Eqs. (5.4)–(5.5) in slab geometry. The method of solution was discussed in detail Chapter 3 and in Ofman *et al.*(1991). We have imposed the conducting wall, and no-slip boundary conditions in x and y-directions, respectively; namely, $\psi(x = \pm x_{max}, y) = 0$, $\phi(x = \pm x_{max}, y) = 0$, $\psi(x, y = \pm y_{max}) = 0$, and $\phi(x, y = \pm y_{max}) = 0$. The calculations are initiated with a small perturbation in ψ (that is nearly azimuthally symmetric). Figures 5.5– 5.7 show the relaxation of an x-point with conducting wall boundary conditions and with a nearly azimuthal initial perturbation (equivalent to $m = 0$ in cylindrical coordinates). Here $S = 10^4$. In Fig. 5.5 a plot of the energies stored in the x and y-components of the magnetic field, and the total energy as a function of time are displayed. The relaxation of the x-point proceeds at the rate predicted by the linear theory and the perturbed energies are transferred alternately between the x-component (curve A) and y-component (curve B) of the magnetic field. The total energy (curve C) is conserved within the anticipated resistive dissipation rate. The perturbed energies stored in the x and y-components of the magnetic field are given by

$$\Delta E_M(t) =$$

$$= \int_{-x_{\max}}^{x_{\max}} \int_{-y_{\max}}^{y_{\max}} \left[\left(\frac{\partial \psi}{\partial y} - y \right)^2 + \left(\frac{\partial \psi}{\partial x} + x \right)^2 - y^2 - x^2 \right] dx\, dy, \quad (5.19)$$

where the size of the computation domain is $2x_{\max}$ by $2y_{\max}$. The change in the total energy ΔE_{tot} was defined in Eq. (4.8). Figure 5.6 shows $\psi(0, 0, t)$ (curve

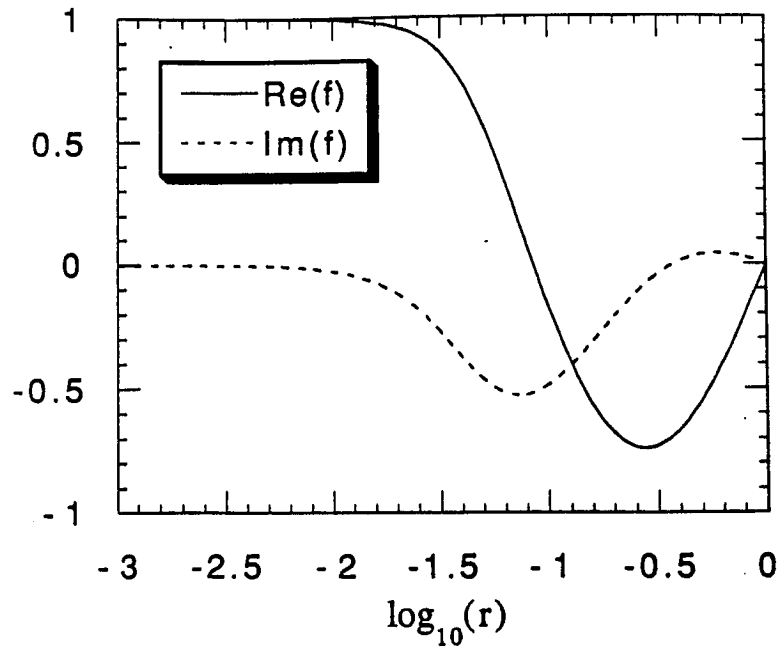

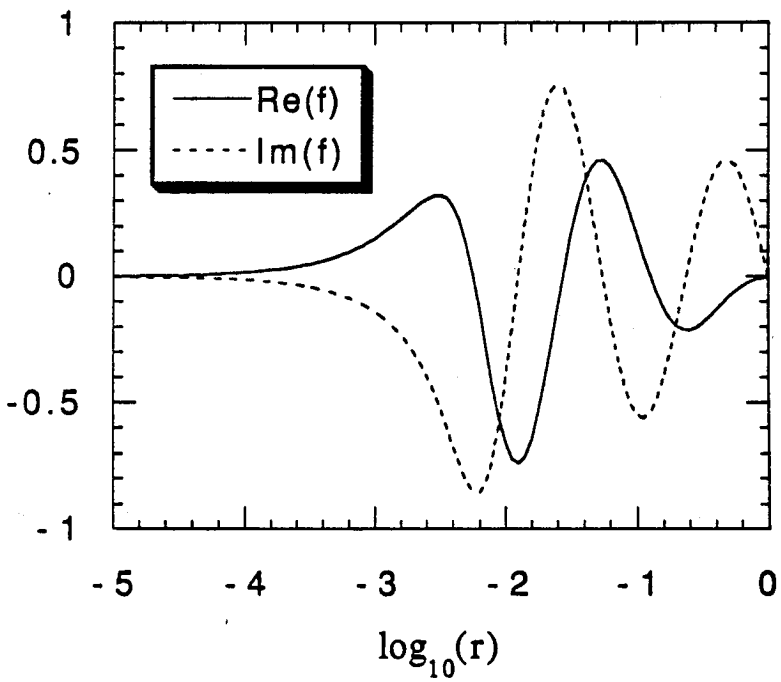

Figure 5.3: The real and imaginary parts of the eigenfunctions $f(r)$ with $m = 0$, $n = 1$, $S = 10^3$, $\gamma = 0.292 + 1.248i$ (top figure), and $m = 1$, $n = 3$, $S = 10^5$, $\gamma = 0.275 + 2.343i$ (bottom figure).

A), and the reconnected flux (curve B) defined by

$$\Delta\Phi(t) \equiv \int_{-x_{\max}}^{x_{\max}} \left| \frac{\partial}{\partial x'} \psi(x', 0, t) \right| dx' + \int_{-y_{\max}}^{y_{\max}} \left| \frac{\partial}{\partial y'} \psi(0, y', t) \right| dy'. \quad (5.20)$$

When the initial perturbation decays, the decay rate and the oscillation frequency approach the values predicted by the linear theory. These can be determined from $\psi(0,0,t)$, or the perturbed energies. In Fig. 5.7 we present the contour lines of the total flux function $\Psi = \psi + \psi_E$ at several representative times during the relaxation with $S = 10^4$. The region shown is 0.25 by 0.25 (in units of a_b) centered at the origin. Fig. 5.7a is at the minimum of an oscillation with negative $\psi(0,0,t)$, Fig. 5.7b is at a time that $\psi(0,0,t)$ is nearly zero, and in Fig. 5.7c $\psi(0,0,t)$ is at its maximum (see, Fig. 5.6). The angle between the separatrices (the solid lines adjacent to the region of $\psi(0,0,t) < 0$) in Fig. 5.7a is larger than $\pi/2$, and in Fig. 5.7c is less than $\pi/2$, indicating the stressing of the magnetic configuration. In Fig. 5.7b, the separatrices are nearly perpendicular and the magnetic configuration is close to the force-free state. The oscillation are damped by the resistive reconnection, and the final state is the force-free x-point configuration given by ψ_E.

When the magnetic fields at the boundaries are free to adjust, the perturbed x-point evolves into a sheet current. In Fig. 5.8a we present a magnetic configuration obtained with the free boundary conditions. The transition to the sheet current occurs rapidly on an Alfvén time scale, and is more than an order of magnitude faster than the resistive relaxation time. The rate of the transition is weakly dependent on resistivity, and the mechanism of the transition involves large flow vortices that are generated around the x-point. In Fig. 5.8b the dotted contour line vortices correspond to clockwise rotation,

while solid contour line vortices correspond to anticlockwise rotation. An outflow along the x and y axis is present, and flow through the boundaries is evident.

5.4.2 Compressible MHD

Equations (1.1)–(1.3) and Equation 1.5 were solved using the Lax-Wendroff differencing scheme, in a manner similar to that given by Richtmyer and Morton (1967), along with a smoothing term suggested by Lapidus (1967). The computation domain is in the (r, θ) plane, where $0 \leq \theta \leq \pi$, $0 \leq r \leq 1$. Equation (1.4) is not solved explicitly, however, the quality of the solutions can be monitored by checking that Eq. (1.4) is satisfied. The code was tested, and successfully applied to other MHD problems (Steinolfson and Winglee, 1992). Here the code is used with conducting wall boundary conditions at the outer boundary $r = 1$, $0 \leq \theta \leq \pi$, and symmetry boundary conditions at the diameter $0 \leq r \leq 1, \theta = 0, \pi$. The calculations are initiated with single m mode magnetic field perturbations that are zero at $r = 1$. The simulations are evolved until the magnetic field configuration reaches a steady state (i.e., relaxes to the force-free x-point). The temporal evolution of the magnetic field at $r_i = 0.02, 0.04, 0.06, 0.08, 0.1$, and $\theta = \pi/2$ is shown in Figs. 5.9–5.10 (curves A-E, respectively). The values shown are of $\Delta B_\theta = [B_\theta(r_i, \theta, t) - B_\theta(r_i, \theta, 1)] / B_\theta(r_i, \theta, 1)$, with $S = 10^4$, and $m = 0$. The fields oscillate almost in phase at r_i, and the frequency agrees well with that predicted by linear theory. The minor phase difference, and the higher harmonics are due to nonlinear effects, and can be made arbitrary small by reducing the magnitude of the initiating perturbation. In Fig. 5.9b the initial $m = 0$

perturbation is an order of magnitude smaller than the one in Fig. 5.9a, and the evolution at r_i approaches that expected from linear theory. In Fig. 5.10 we show the temporal evolution of ΔB_θ, where the initial perturbation was $m = 2$. The frequency and the decay rate of the evolution agree with the linear theory predictions. The rapid relaxation (compared to τ_r) to the force-free state agrees with the experimental results [Bratenahl and Yeates (1970); Baum and Bratenahl (1974a); Baum *et al.* (1973a,b)]

When magnetic field and flow are allowed to change at the outer $r = 1$ boundary (free boundary conditions), the perturbed x-point evolves into a sheet current. We have approximated the free boundary conditions by the zero order extrapolation boundary conditions given by,

$$\mathbf{v}(r_J, \theta, t_n) = \mathbf{v}(r_{J-1}, \theta, t_n), \tag{5.21}$$

$$\mathbf{B}(r_J, \theta, t_n) = \mathbf{B}(r_{J-1}, \theta, t_n), \tag{5.22}$$

$$\rho(r_J, \theta, t_n) = \rho(r_{J-1}, \theta, t_n), \tag{5.23}$$

$$P(r_J, \theta, t_n) = P(r_{J-1}, \theta, t_n), \tag{5.24}$$

where $r_J = 1$ is the radial grid point at the boundary. These boundary conditions allow magnetic and velocity flux through the boundary and, with the Lax-Wendroff differencing scheme, are equivalent to approximating the value of the flux through the boundary at the current half-time-step by the value from the previous half time step. The sheet current is subject further to the tearing mode instability, and a large (compared to the width of the current layer) magnetic island that is centered at the origin is created. The transition proceeds on a shorter time scale than that for resistive reconnection, and the time scale

estimated from the compressible code is longer than the time scale obtained from the incompressible model. In Figs. 5.11a–5.11c we show the evolution of the magnetic field configuration at $t = 0.4483$, 0.7011, and 1.00 minutes. It is evident in Figs. 5.11a–5.11b that the x-point transforms to two y-points connected with a sheet current, and in Fig. 5.11c it reaches its maximal extent and is subject to the tearing mode instability. In Fig. 5.12 we show the velocity stream lines; the outflow parallel to the sheet current is clearly seen. The direction of the stream lines in Fig. 5.12a at $t = 0.5\ min$ agree with the direction of the flow in Fig. 5.8a near the x and y axis. In Fig. 5.12b $t = 0.7503\ min$ and the flow points toward the origin parallel to $\theta = 0, \pi$ and $0 \leq r \leq 1$, while the outflow is parallel to the sheet current ($\theta = \pi/2$), in agreement with Dungey's qualitative analysis.

5.5 Summary and Discussion

We have derived the linear dispersion relation for the reconnection rate of an x-type neutral point with conducting wall boundary conditions. Numerical solution of the dispersion relation agrees with the asymptotic expressions for the decay rate. We have solved the nonlinear incompressible 2-D MHD Equations (5.4)–(5.5) in slab geometry, using the ADI method. The computations were initiated with small nearly azimuthally symmetric perturbation of ψ with large $\Delta t \sim 0.8\tau_h$, and the magnetic Reynolds number was in the range $10^2 \leq S \leq 4 \cdot 10^4$. We have found that the perturbations decay in agreement with the linear dispersion relation for $n = m = 0$ modes. Rapidly growing instability on an Alfvén time scale was found in the incompressible simulations when the fields at the boundaries are allowed to adjust; the growth

rate dependents weakly on S. The x-type neutral point evolved into a sheet current in accordance with Dungey's (1958) qualitative description.

We have solved compressible 2-D MHD equations in the (r, θ) plane using the Lax-Wendroff differencing scheme, and found that with conducting wall boundary conditions the perturbed x-point relaxes to the force-free state for $m = 0$ and for $m \neq 0$ initial perturbations. The decay rate and the oscillation frequency in the linear stage agree well with the values obtained from the solution of the dispersion relation. A transition to a sheet current was found when free (zero order extrapolation) boundary conditions were used. The transition is faster than the resistive reconnection rate, but slower than the rate obtained from the incompressible simulations. The outflow along the sheet current and the flow towards the x-point at the origin along the x-axis $(\theta = 0, \pi, 0 \leq r \leq 1)$ occurred in the incompressible, and the compressible simulations. The evolution of the x-point that emerged from the simulations, for both conducting wall, and free boundary conditions agree well with the theoretical predictions.

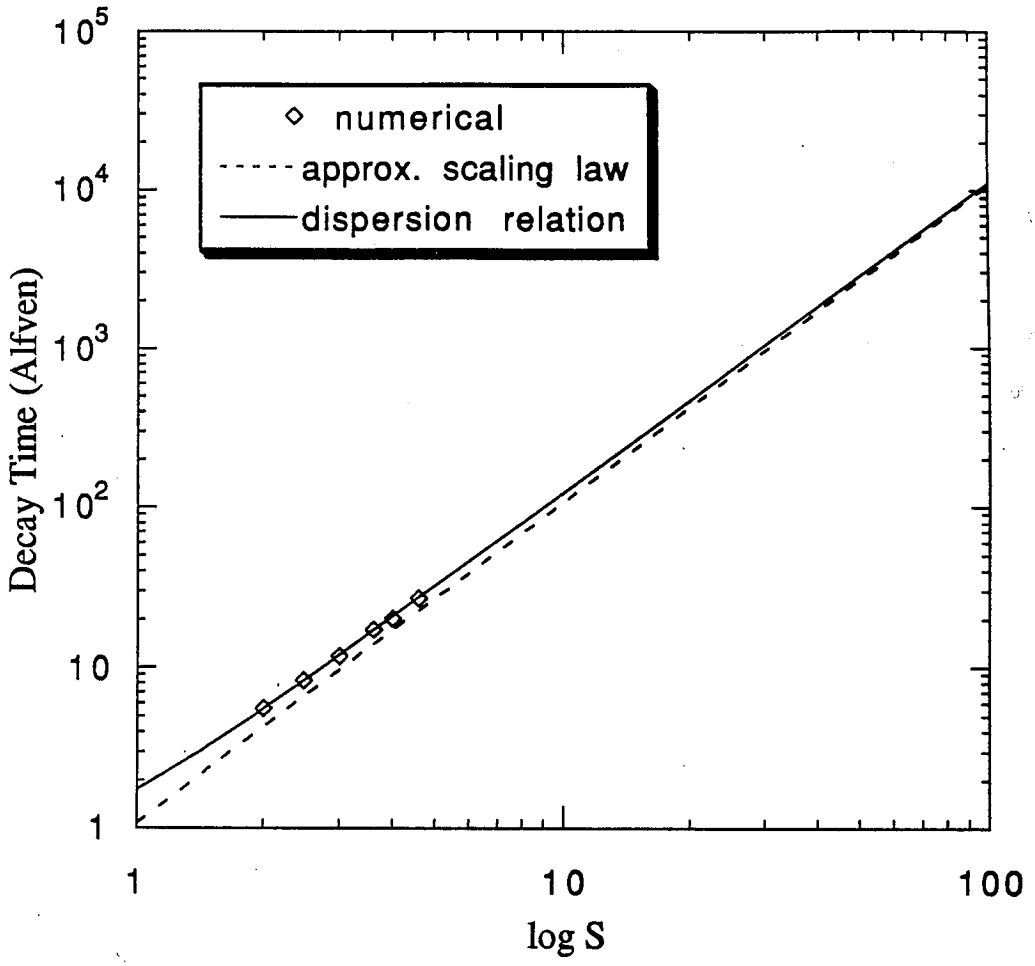

Figure 5.4: The decay rate scaling with S of the $m = n = 0$ mode.

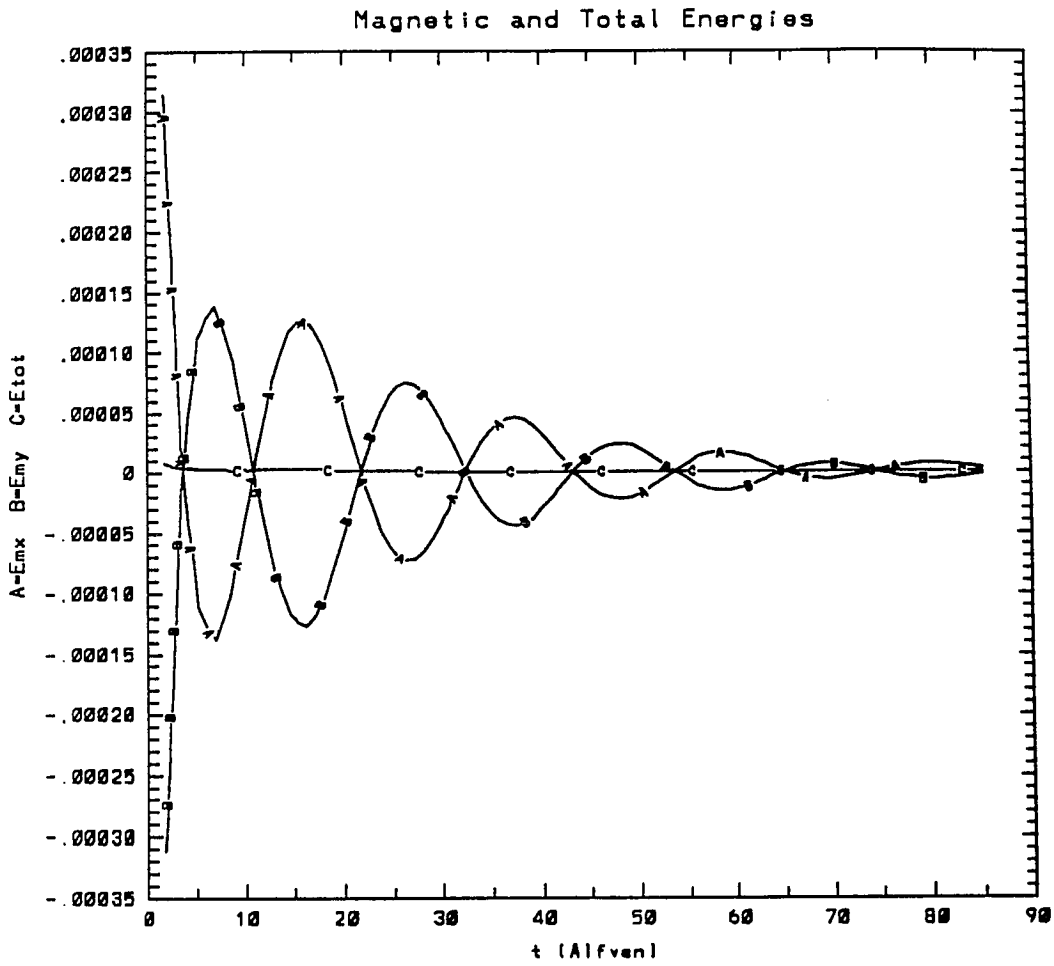

Figure 5.5: The perturbed energies of an x-point. ΔE_{Mx} (curve A), ΔE_{My} (curve B), and ΔE_{tot} (curve C).

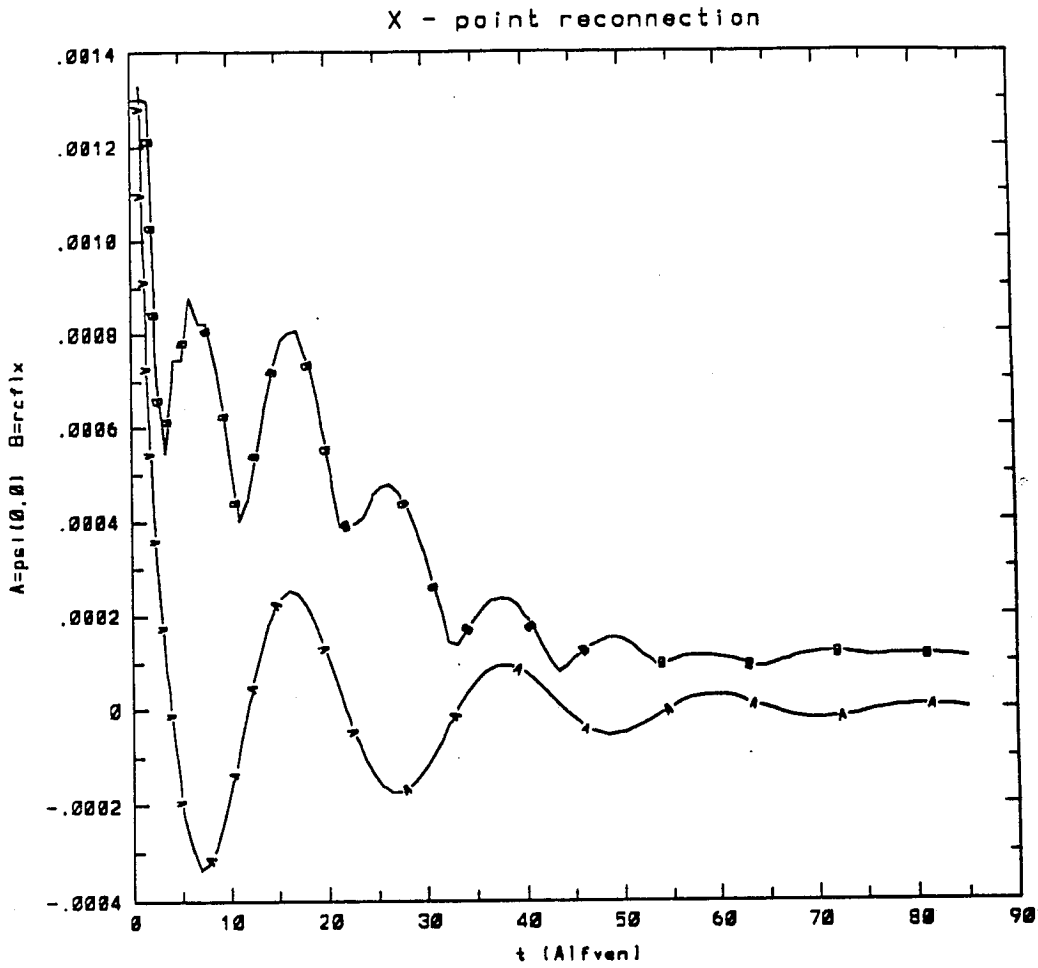

Figure 5.5: The value of $\psi(0,0,t)$ (curve A), and the reconnected flux (curve B).

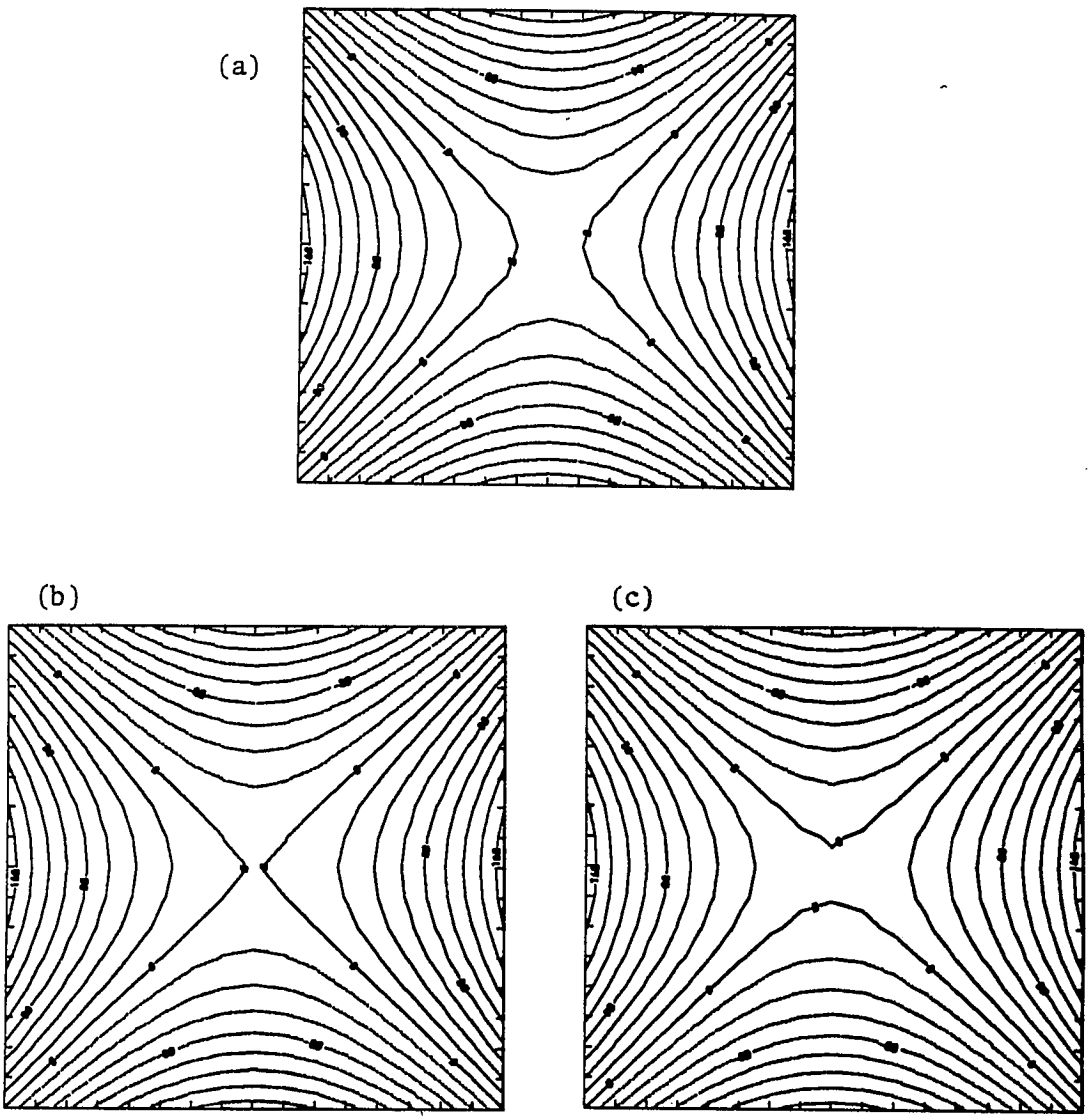

Figure 5.7: Contour lines of Ψ.
(a) At a time of a minimum of an oscillation ($\psi(0,0,t) < 0$). (b) At a time of $\psi(0,0,t) \sim 0$. (c) At a time of a maximum of an oscillation ($\psi(0,0,t) > 0$).

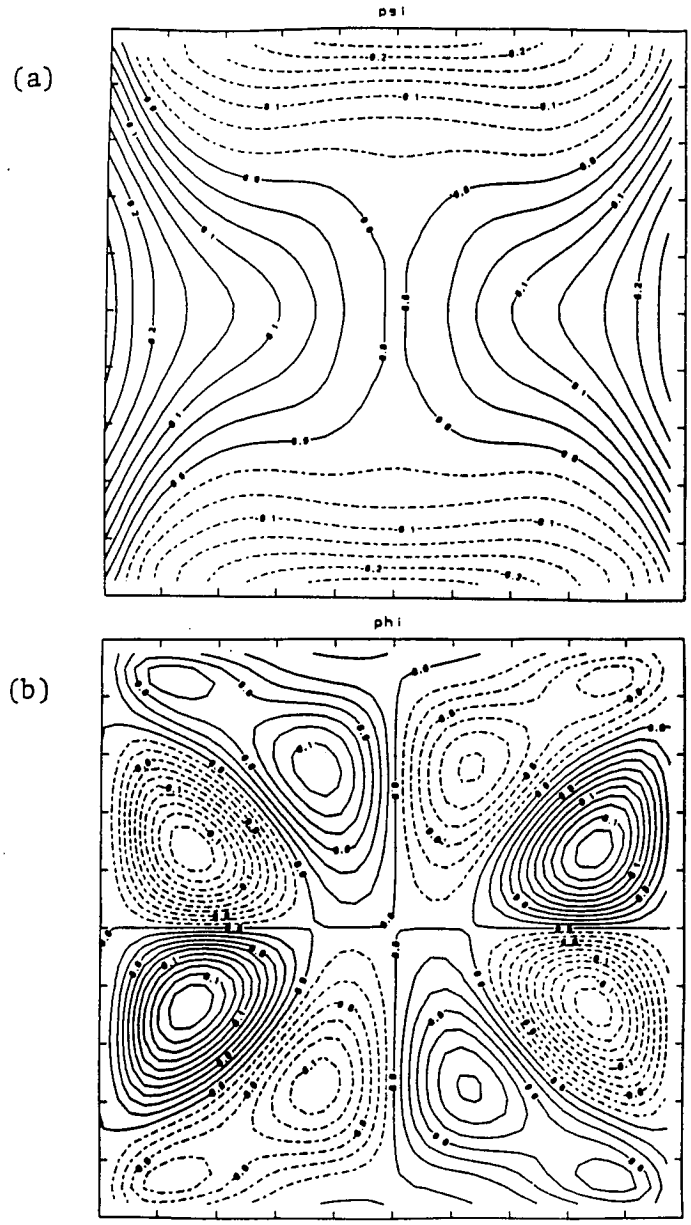

Figure 5.8: The sheet current at $t = 5.3\tau_h$ with the incompressible MHD simulations.
(a) Contour lines of Ψ. (b) Contour lines of ϕ.

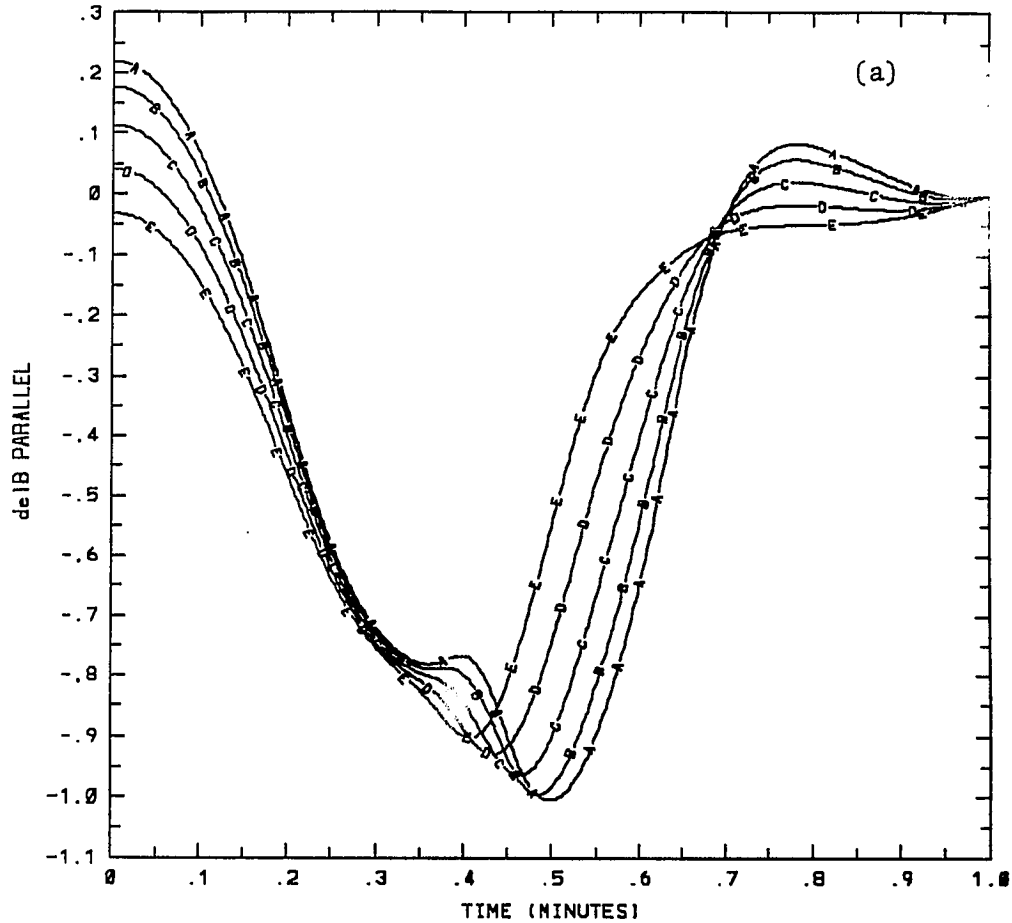

Figure 5.9: Compressible MHD simulation of the relaxation of an x-point with $m = 0$ initial perturbation.
(a) The change of the magnetic field at r_i, $\theta = \pi/2$.

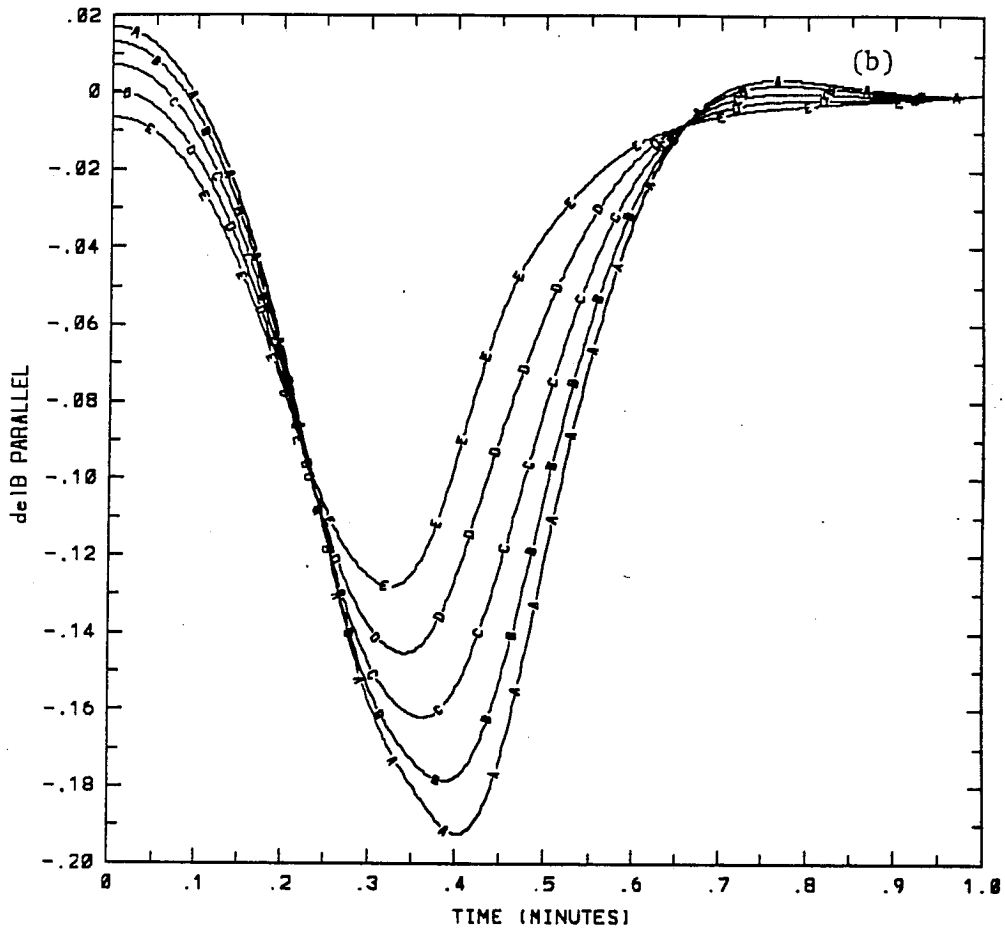

(b) Same as (a) with smaller magnitude $m = 0$ initial perturbation.

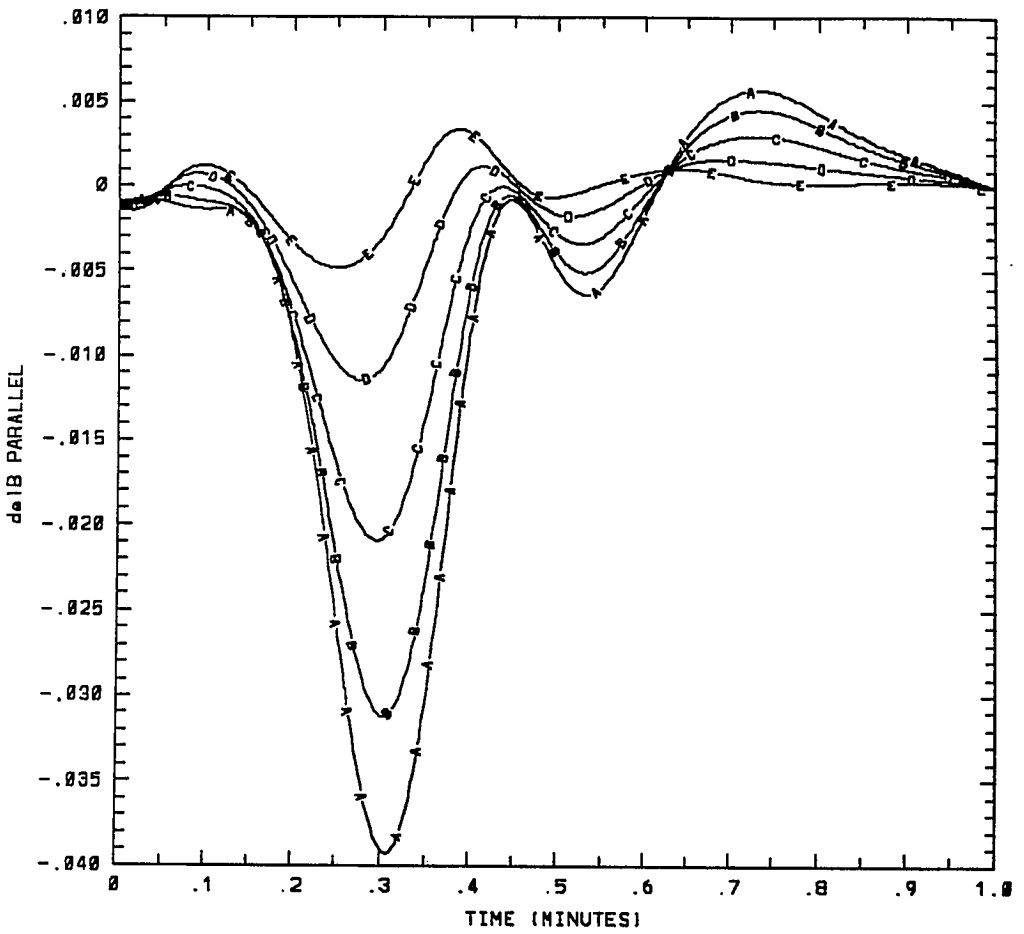

Figure 5.10: Compressible MHD simulation of the relaxation of an x-point with $m = 2$ initial perturbation.

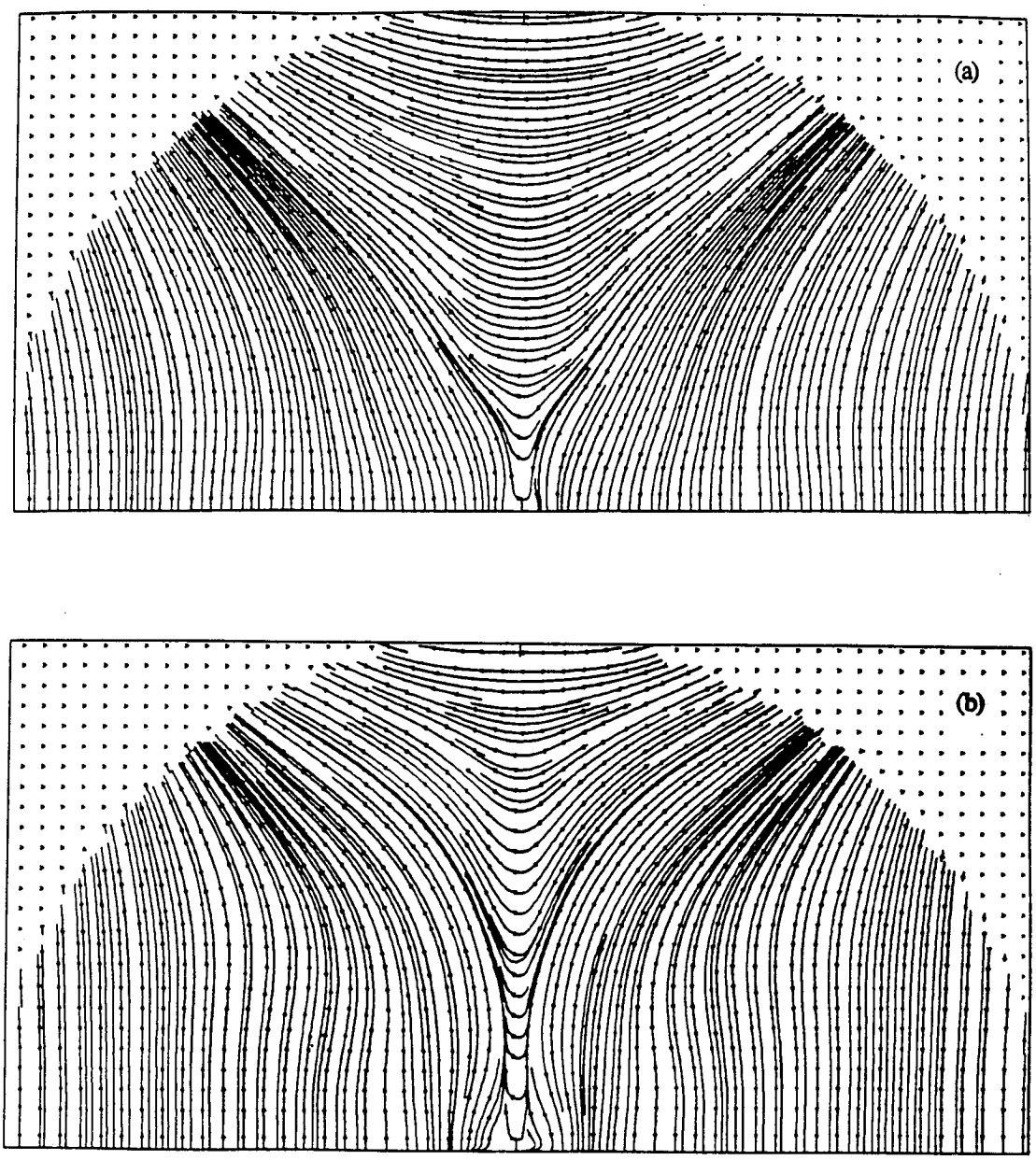

Figure 5.11: The evolution of a sheet current with the compressible MHD simulations.
(a) The magnetic field lines at $t = 0.4483$ *min*. (b) Same as (a) at $t = 0.7011$ *min*.

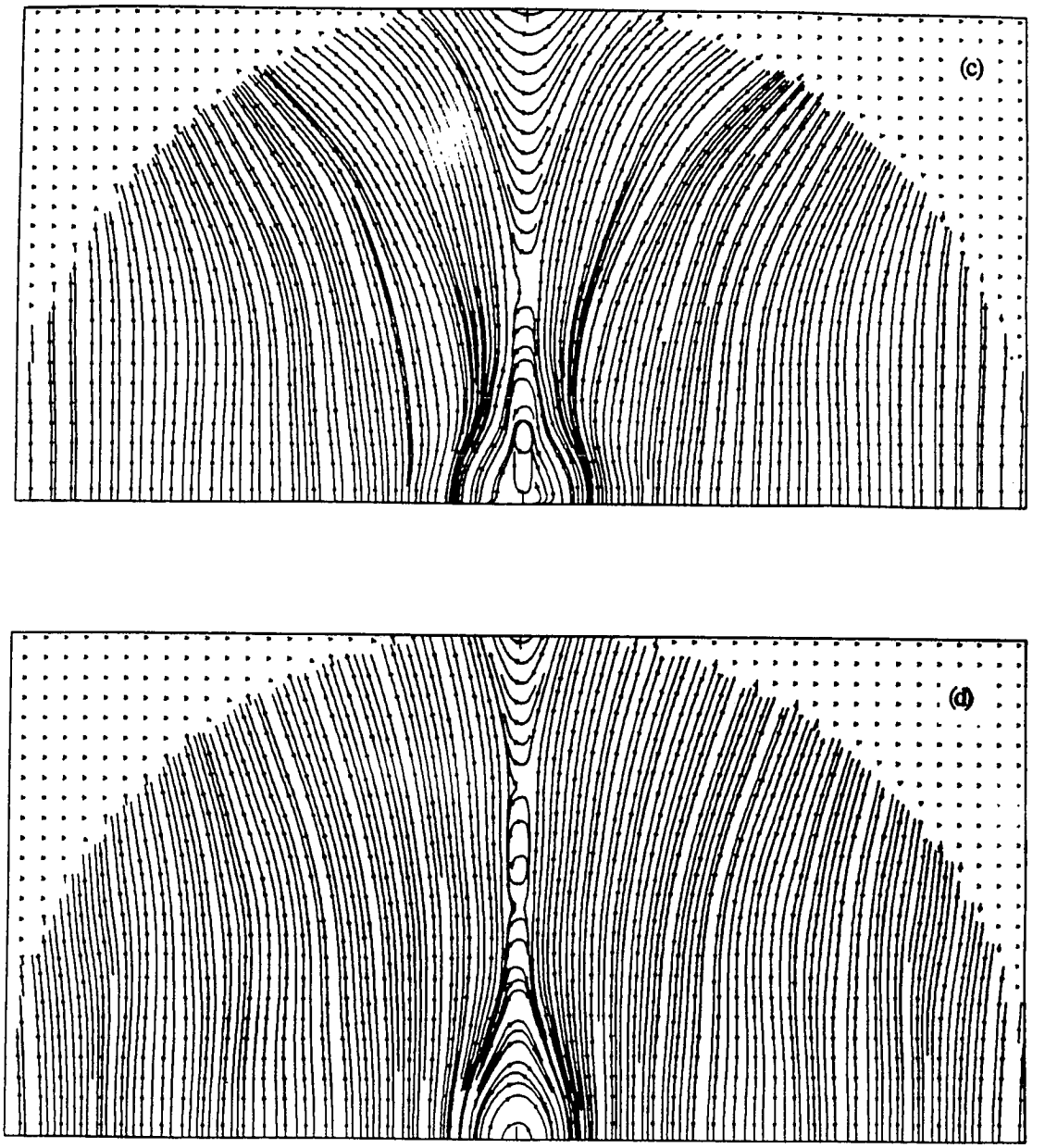

(c) Same as (a) at $t = 1.0\ min.$ (d) Same as (c) with larger initial perturbation.

5.6 Appendix

In this Appendix, we show why the linearized compressible MHD Eqs. (5.6)–(5.8) for the x-point initial magnetic field equilibrium (5.3) with conducting wall boundary conditions, initial uniform density and pressure can be approximated near the x-point by the incompressible 2-D MHD.

In Eq. (5.6) we have assumed $\nabla P = 0$, and from linearized Eq. (1.5) we have to the first order

$$P \sim \rho, \tag{5.25}$$

where P and ρ are the perturbed pressure and density respectively. Hence, both P and ρ are to the first order functions of time alone, and we get (with the equilibrium density $\rho_0 \equiv 1$)

$$\frac{\partial \rho(t)}{\partial t} + \nabla \cdot \mathbf{v}(x, y, z, t) = 0 \tag{5.26}$$

and therefore $\nabla \cdot \mathbf{v}$ is to the first order a function of time alone. Since the evolution is two dimensional for both the compressible and the incompressible case ($B_z = v_z = 0$) we can separate the velocity into compressible and incompressible parts

$$\mathbf{v} = \nabla \times (\phi \mathbf{e}_z) + \mathbf{r} f(t), \tag{5.27}$$

where the first term is the incompressible part, $f(t) \equiv \nabla \cdot \mathbf{v}$, and $\mathbf{r} = x\mathbf{e}_x + y\mathbf{e}_y$. Next, substituting $\mathbf{v}$ from Eq. (5.27) into Eq. (5.7) and taking the curl of the result yields an equation identical to the linearized form of the incompressible momentum Equation (5.5)

$$\frac{\partial \omega}{\partial t} = -y \frac{\partial J}{\partial x} - x \frac{\partial J}{\partial y}. \tag{5.28}$$

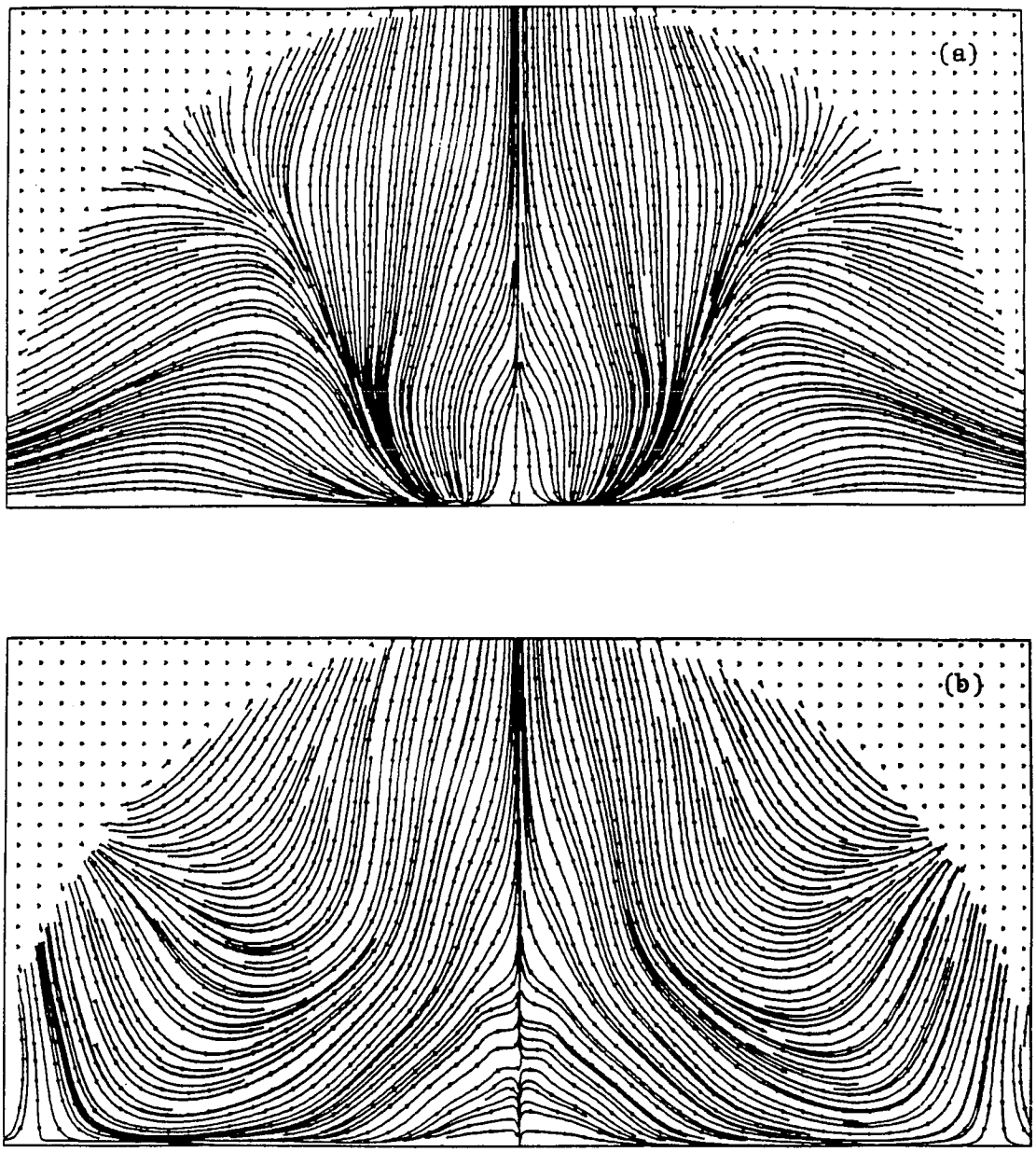

Figure 5.12: The velocity stream lines of the sheet current.
(a) At time $t = 0.5\ min.$ (b) At time $t = 0.7503\ min.$

Next, we substitute the velocity Eq. (5.27) into the linearized Ampere's Eq. (5.8) and get

$$\frac{\partial \psi}{\partial t} = S^{-1}\nabla^2\psi - \frac{\partial \phi}{\partial y}x + \frac{\partial \phi}{\partial x}y + (x^2 - y^2)f(t), \tag{5.29}$$

where the last term on the r.h.s accounts for the departure from the incompressible evolution. It is clear that this term vanishes on the separatrices of the x-point magnetic field configuration (given by $x = \pm y$) and at the x-point. It is also evident that as $r \to 0$ the incompressible term approaches zero at least as r^2.

Since the reconnection of the x-point in the linear stages occurs in the vicinity of $r = 0$, and as the initial perturbation decays exponentially, its relative importance becomes even more localized near the x-point, the evolution and the decay rates obtained from the linearized compressible MHD equations are expected to be in good agreement with the evolution and the decay rates obtained from the incompressible 2-D MHD equations. The agreement is found to hold numerically and is shown in Fig. 5.4.

BIBLIOGRAPHY

1. Akasofu, S.I., *Physics of Magnetospheric Substorms*, (Reidel, 1977).
2. Baum, P.J., and A. Bratenahl, J. Plasma Phys. **11**, 93 (1974).
3. Baum, P.J., and A. Bratenahl, Phys. Fluids **17**, 1232 (1974).
4. Baum, P.J., A. Bratenahl, and R.S. White, Phys. Fluids **16**, 226 (1973)
5. Baum, P.J., and J. Pollack, J. Appl. Phys. **44**, 163 (1973).
6. Braginskii, S.I., Rev. Plasma Phys. **1**, 205 (1965).
7. Bratenahl, A., and C.M Yeates, Phys. Fluids **13**, 2696 (1970).
8. Carreras, B., H.R. Hicks, and B.V. Waddell, Nucl. Fusion **19**, 583 (1979).
9. Chapman, S., and P.C. Kendall, Proc. Roy. Soc. **A271**, 435 (1963).
10. Chen, X.L., and P.J. Morrison, Phys. Fluids B **2**, 495 (1990).
11. Chen, X.L., and P.J. Morrison, Phys. Fluids B **2**, 2575 (1990).
12. Chen, X.L., and P.J. Morrison, Phys. Fluids B **4**, 845 (1992).
13. Coppi, B., R. Galvao, R. Pellat, M.N. Rosenbluth, and P.H. Rutherford, Sov. J. Plasma Phys. **2**, 533, (1976).
14. Craig, I.J., and A.N. McClymont, Ap. J. **371**, L41 (1991).
15. Giovanelli, R.G., Mon. Not. R. Astron. Soc. **107**, 338 (1947).
16. Dnestrovskii, Yu.N., D.P. Kostomorov, and A.M. Popov, Sov. J. Plasma Phys. **5**, 289 (1979).

17. Dobrowolny, M., P. Veltri, and A. Mangeney, J. Plasma Phys. **29**, 303 (1983).

18. Drake, J.F., and Y. C. Lee, Phys. Fluids **20**, 134 (1977).

19. Drake, J.F., *IAU Symposium 107*, ed. M. R. Kundu and G. D. Holman (Reidel, 1985).

20. Dungey, J.W., Phil. Mag., **44**, 725 (1953).

21. Dungey, J.W., *Cosmic Electrodynamics*, pp. 98-102 (Cambridge U.P., New York, 1958).

22. Einaudi, G., and F. Rubini, Phys. Fluids **29**, 2563 (1986).

23. Einaudi, G., and F. Rubini, Phys. Fluids B **1**, 2224 (1989).

24. Furth, H.P., J. Killeen, and M.N. Rosenbluth, Phys. Fluids **6**, 459 (1963).

25. Furth, H.P., P.H. Rutherford, and H. Selberg, Phys. Fluids **16**, 1054 (1973).

26. Gatilov, V.V., A.M. Sagalakov, and V.F. Ul'chenko, Sov. J. Plasma Phys. **15**, 31, (1989).

27. Giovanelli, R.G., Mon. Not. R. Astron. Soc. **107**, 338 (1947).

28. Hassam, A.B., Bull. Amer. Astron. Soc. **22**, 853 (1990).

29. Kerner, W., and H. Tasso, Plasma Phys. **24**, 97 (1982).

30. Killeen, J., *Physics of Hot Plasmas*, edited by B. J. Rye and J. C. Taylor (Oliver & Boyd, 1970).

31. Lapidus, A., J. Comp. Phys. **2**, 154 (1967).

32. Lee, Y.C., J.W. Van Dam, J.F. Drake, A.T. Lin, P.L. Pritchett, D.D'Ippolito, P.C. Liewer, and C.S. Liu, in *Plasma Physics and Controlled Nuclear Fusion Research*, Vol. I, p. 799 (International Atomic Energy Agency, Viena, 1979).

33. Mahajan, S.M., and R.D. Hazeltine, Nucl. Fusion **22**, 1191 (1982).

34. Oberhettinger, F., in *Handbook of Mathematical Functions*, edited by M. Abramowitz, and I.A. Stegun (Dover Publications, Inc., New York, 1972).

35. Ofman, L., submitted to Phys. Fluids B (1992).

36. Ofman, L., X.L. Chen, P.J. Morrison, and R.S. Steinolfson, Phys. Fluids B **3**, 1364 (1991).

37. Ofman, L., P.J. Morrison, and R.S. Steinolfson, Institute for Fusion Studies Report #530, The University of Texas at Austin, December 1991.

38. Paris, R.B., and W. N.-C. Sy, Phys. Fluids **26**, 2966 (1983).

39. Parker, E.N., Ap. J. **138**, 552 (1963).

40. Persson, M., Ph.D. thesis, Chalmers University of Technology, Göteborg, 1987.

41. Persson, M., and A. Bondeson, Phys. Fluids B **2**, 2315 (1990).

42. Persson, M., Nucl. Fusion **31**, 382 (1991).

43. Petschek, H.E., *AAS-NASA Symp. on Solar Flares*, NASA SP-50, p.425 (1964).

44. Porcelli, F., Phys. Fluids **30**, 1734 (1987).

45. Priest, E.R., *Solar Flare Magnetohydrodynamics*, Ch. 5 (Gordon and Breach, New York, 1981).

46. Priest, E.R., *Solar Magnetohydrodynamics*, (Reidel, Dordrecht, The Netherlands, 1985).

47. Pritchett, P.L., Y.C. Lee, and J.F. Drake, Phys. Fluids **23**, 1368 (1980).

48. Richtmyer, R.D., and K.W. Morton, *Difference Methods for Initial Value Problems*, 2nd ed. (Wiley-Interscience, New York, 1967).

49. Rutherford, P.H., Phys. Fluids **16**, 1903 (1973).

50. Schnack, D.D., Ph.D. thesis, University of California, Davis, 1977.

51. Schnack, D.D., and J. Killeen, in *Theoretical and Computational Plasma Physics*, p. 337, (International Atomic Energy Agency, Viena, 1978).

52. Schnack, D.D., and J. Killeen, Nucl. Fusion **19**, 877 (1979).

53. Spicer, D.S., Solar Physics **53**, 305 (1977).

54. Steinolfson, R.S., and G. Van Hoven, Phys. Fluids **26**, 117 (1983).

55. Steinolfson, R.S., and G. Van Hoven, Phys. Fluids **27**, 1207 (1984).

56. Steinolfson, R.S, and R.M. Winglee, J. Geophys. Res., submitted (1992).

57. Stix, T.H., Phys. Rev. Letters **3** 6, 521 (1976).

58. Strauss, H.R., J. Comp. Phys. **28**, 437 (1978).

59. Sturrock, P., *Solar Flares*, pp. 83-117 (Colorado Associated University Press, Boulder, CO, 1980).

60. Sweet, P.A., IAU Symp. **6**, 123 (1958).

61. Syrovatsky, S.I., Soviet Astron. **10**, 270 (1966).

62. Vekstein, G.E., and E.R. Priest, Ap. J., **384**, 333 (1992).

63. Wang, S., L. C. Lee, and C. Q. Wei, Phys. Fluids 31, 1544 (1988).

64. Wang, H., and H. Zirin, Bull. Am. Ast. Soc. **22**, 2 (1990).

VITA

Leon Ofman was born in Riga, Latvia, on May 20, 1962, the son of Maxim Ofman and Nomi Ofman (Gorfinkel). In June 1972 he immigrated with his family to Israel. After graduating from the Katsanelson high school, Kfar-Saba, Israel in the summer of 1980, he joined the Israeli Defense Forces. After completing three years of military service in October 1983, he entered the Tel-Aviv University, Tel-Aviv, Israel. On July 23, 1986 he received the Bachelor of Science degree in Physics, and entered the graduate program in the fall of 1986. On November 2, 1988 he received the Master of Science degree in Physics from Tel-Aviv University. During his studies at the Tel-Aviv University he worked as a research and teaching assistant at the Department of Physics and performed part of his research at the Space Environment Laboratory, Boulder, Colorado, and at the Paris Observatory in Meudon, France. From February to July of 1989 he was employed as a physicist at Orbot Instruments, Yavneh, Israel. In August 1989 he entered the graduate school of the University of Texas at Austin and has been employed as a research assistant at the Institute for Fusion Studies and at Southwest Research Institute, San Antonio, Texas, as well as a teaching assistant at the Department of Physics. On November 11, 1987 he married Rachel Ofman (Srago) and they do not have children (yet).

Permanent address: 12/5 Hatapuz St.
Kfar Saba
Israel 44108

This dissertation was typeset with LaTeX by the author.